Temperature/Emissivity Separation Algorithm Theoretical Basis Document, Version 2.4

A. R. Gillespie,[1] S. Rokugawa,[2] S. J. Hook,[3] T. Matsunaga,[4] and A. B. Kahle[3]

[1] Department of Geological Sciences, University of Washington, Seattle, Washington 98195, USA
[2] The University of Tokyo, Faculty of Engineering, 7-3-1 Hongo, Bunkyo-ku, Tokyo 113, JAPAN
[3] Jet Propulsion Laboratory 183-501, Pasadena, California 91109, USA
[4] Geological Survey of Japan, 1-1-3 Higashi, Tsukuba, Ibaraki 305, JAPAN

Prepared under NASA Contract NAS5-31372

22 March 1999

ABSTRACT

The ASTER scanner on NASA's Terra (EOS-AM1) satellite will collect five channels of TIR data with an NEΔT of $\leq$0.3K to estimate surface kinetic temperatures and emissivity spectra, especially over land, where emissivities are not known in advance. Temperature/emissivity separation (TES) is difficult because there are five measurements but six unknowns. Various approaches have been used to constrain the extra degree of freedom. ASTER's TES algorithm hybridizes two established algorithms, first estimating the temperature and band emissivities by the Normalized Emissivity Method, and then normalizing the emissivities by their average value. Next, an empirical relationship adapted from the Alpha Residual method is used to predict the minimum emissivity from the spectral contrast (min-max difference or MMD) of the normalized values, permitting recovery of the emissivity spectrum with improved accuracy. TES uses an iterative approach to remove reflected sky irradiance. Input to TES consists of land-leaving radiances (compensated for atmospheric absorption and path radiance) and downwelling sky irradiance. Based on numerical simulation, TES can recover temperatures within about ±1.5 K, and emissivities within about ±0.015. Limitations arise from the empirical relationship between emissivity values and spectral contrast, compensation for reflected sky irradiance, and ASTER's precision, calibration, and atmospheric correction.

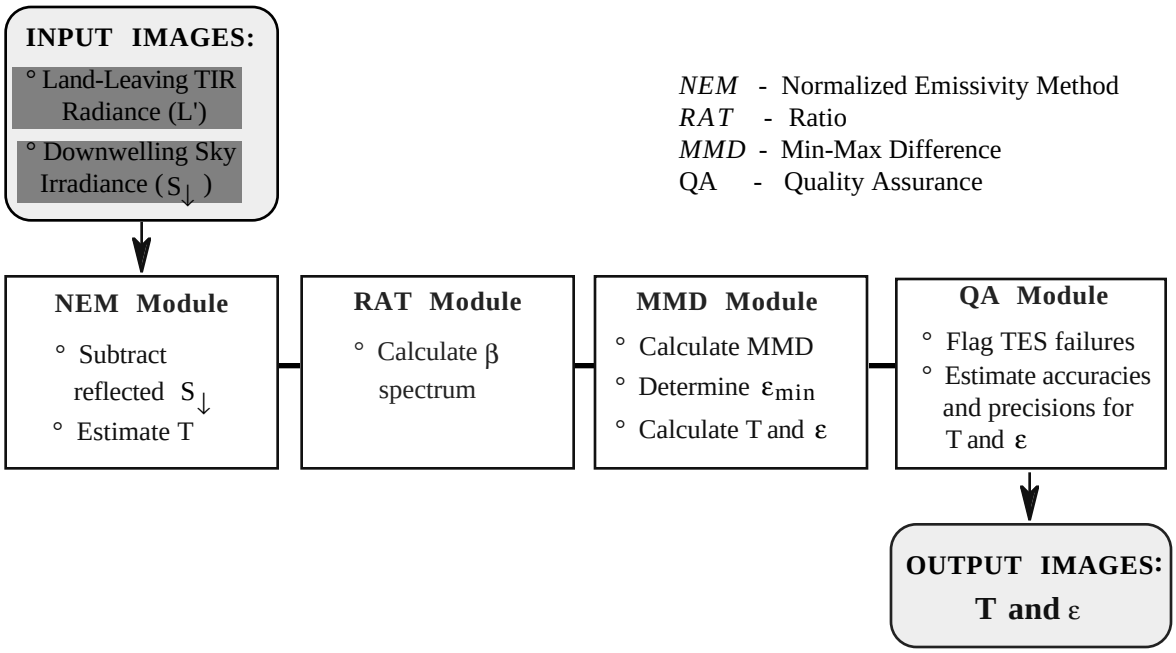

Figure 1. Basic design of the TES algorithm. The NEM module estimates normalized emissivities used to estimate reflected sky irradiance, which is removed iteratively, and then estimates the surface temperature T. T is used in the RATIO module to calculate normalized emissivities, or β values, which measure spectral shape. The MMD module calculates the Min-Max β difference, from which the minimum emissivity ε_{min} is found by empirical regression. The β spectrum is scaled by ε_{min} to give the TES emissivities, from which the surface temperature is calculated. Accuracies and precisions are calculated from data characteristics and measures of TES performance. A more detailed flow diagram is given in Figure 4.

TABLE OF CONTENTS

1. INTRODUCTION

The Advanced Spaceborne Thermal Emission and Reflection Radiometer (ASTER) includes a five-channel multispectral thermal-infrared (TIR) scanner designed for recovery of land-surface "kinetic" temperatures and emissivities, not just temperatures over homogeneous surfaces of known emissivity such as water. Land surface temperatures (T) are important in global-change studies, in estimating radiation budgets and heat-balance studies, and as control for climate models. Emissivities (ε) are strongly indicative, even diagnostic, of composition, especially for the silicate minerals that make up much of the land surface. Surface emissivities are thus important for studies of soil development and erosion and for estimating amounts and changes in sparse vegetative cover for which the substrate is visible. Surface temperatures are independent of wavelength and can be recovered from a small number of bands. Because emissivity spectra of geologic materials can be quite complex, emissivity studies require as many spectral bands in the 8-14 μm TIR window as possible.

ASTER will be carried on the first platform of NASA's Earth Observing System, Terra (EOS-AM1), scheduled for launch in July 1999, and will obtain a global emissivity map of the land surface. ASTER will also recover surface temperatures and emissivities for requested localities for the entire six-year lifetime of Terra. With a TIR spatial resolution of 90 m and a VNIR resolution of 15 m, ASTER acts as the "zoom lens" for other EOS imaging experiments. High-resolution ASTER T and ε data can be more readily verified by field experiments and, at the same time, be used to understand the averaged responses of the lower-resolution scanners.

ASTER T and ε values will be recovered using a new Temperature/Emissivity Separation algorithm, TES. The key goals of TES are (1) to estimate accurate and precise surface temperatures especially over vegetation, water and snow, and (2) to recover accurate and precise emissivities for mineral substrates. TES will produce "seamless" images -- in other words, there should be no artifactual discontinuities, such as can be introduced by classification. TES embodies the simplest

approach feasible consistent with the above goals. T (1 band) and ε (5 bands) will be available as standard products from EOS. TES is adaptable to data sources other than ASTER.

Calculating T and ε from radiance measurements is an underdetermined problem, even if the scene is isothermal and consists of a single material of uniform texture and topographic slope and aspect. For ASTER there are five measurements but six unknowns. Consequently, one degree of freedom must be constrained independent of ASTER. There is a degree of arbitrariness in the solution, resulting in a plethora of approaches and algorithms.

The ASTER Temperature/Emissivity Working Group (TEWG) has examined the performance of existing algorithms, with the goal of selecting one to create ASTER temperature and emissivity standard products. Even the best of these had correctable deficiencies, and this observation led us to develop a new, hybrid algorithm (TES: Fig. 1) that combines the desirable features of previous algorithms and adds some new features.

This document gives the theoretical basis for the development of the TES algorithm (see also Gillespie *et al.*, 1998). First, it gives background information and summarizes the behavior of thermal infrared emittance from the terrestrial surface (§2). Next, assumptions critical to the TES algorithm are identified, and the algorithm and its performance (§3) are documented. Finally, a validation plan is presented for the T and ε Standard Products (§4).

Five appendixes are attached to this ATBD. Appendix A summarizes peer reviews (version 1, Hook *et al.*, 1994; version 2.3, Gillespie *et al.*, 1996). Algorithms examined in writing TES are summarized in Appendix B. A discussion of spectral mixing and target heterogeneity is in Appendix C. The effects of multiple scattering among scene elements are discussed in Appendix D. The formal Validation Plan, summarized in §4, is presented in Appendix E and has also been incorporated into a general plan for all of the ASTER Standard Products.

Table 1. Spectral and spatial characteristics of ASTER. Asterisk indicates the stereo band. Stereo Base/Height ratio is 0.6. Estimated radiometric accuracy at 240K is 3 K.

Advanced Spaceborne Thermal Emission Reflectance Radiometer (ASTER).					
Wavelength Region	Band Number	Spectral Range, μm	Radiometric Accuracy	Radiometric Precision	Spatial Resolution
V					
N	1	0.52-0.60	± 4%	≤0.5%	15m
I	2	0.63-0.69	± 4%	≤0.5%	15m
R	3*	0.76-0.86	± 4%	≤0.5%	15m
	4	1.60-1.70	± 4%	≤0.5%	30m
S	5	2.145-2.185	± 4%	≤1.3%	30m
W	6	2.185-2.225	± 4%	≤1.3%	30m
I	7	2.235-2.285	± 4%	≤1.3%	30m
R	8	2.295-2.365	± 4%	≤1.0%	30m
	9	2.360-2.430	± 4%	≤1.3%	30m
			(at 300K)	(at 300K)	
	10	8.125-8.475	1 K	≤0.3 K	90m
T	11	8.475-8.825	1 K	≤0.3 K	90m
I	12	8.925-9.275	1 K	≤0.3 K	90m
R	13	10.25-10.95	1 K	≤0.3 K	90m
	14	10.95-11.65	1 K	≤0.3 K	90m

1.1 The ASTER Imaging System

ASTER is a multispectral scanner that produces images of high spatial resolution. It is currently scheduled to fly in Earth orbit in July, 1999, on Terra, the first platform of NASA's Earth Observing System. The instrument will have three bands in the visible and near-infrared (VNIR) spectral range (0.5-0.9 μm) with 15-m spatial resolution, six bands in the shortwave-infrared (SWIR) spectral range (1.6-2.4 μm) with 30-m spatial resolution, and five bands in the thermal-infrared (TIR) spectral range (8-12 μm), with 90-m resolution (Kahle *et al.*, 1991; Yamaguchi *et al.*, 1993). These 14 bands are collected in three down-looking telescopes that may be slewed ±8.5° (SWIR, TIR) or ±24° (VNIR) in the cross-track direction. Combined with the FOV of ±2.5°, the maximum TIR view angle is thus 11°. An additional backward-viewing telescope with a single band duplicating VNIR band 3 will provide the capability for same-orbit stereogrammetric data. ASTER's estimated TIR radiometric accuracy at 300K is 1K; at 240K it is 3K. Radiometric precision (NEΔT) at 300K is ≤0.3 K. Characteristics of the ASTER scanner are summarized in Table 1. Anticipated performance is documented by Fujisada and Ono (1993).

The ASTER instrument is being provided by the Japanese Government under the Ministry of International Trade and Industry (MITI). The ASTER project is implemented through the Earth Remote Sensing Data Analysis Center (ERSDAC) and the Japan Resources Observation System Organization (JAROS), nonprofit organizations under MITI. JAROS is responsible for the design and development of the ASTER instrument, which was built by the Nippon Electric Company (NEC), the Mitsubishi Electric Corporation (MELCO), Fujitsu, and Hitachi. The ASTER Science Team is an international team of Japanese, American, French, and Australian scientists. The team participates in the definition of the scientific requirements for ASTER, in the development of algorithms for data reduction and analysis, and in calibration, validation and mission planning.

1.2 Product Names and Numbers

The TES algorithm will produce two Standard Products, surface kinetic temperature and surface emissivity. Each product has associated with it a two-plane Quality Assurance (QA) image and image header record describing ASTER data and TES performance characteristics.

Surface Kinetic Temperature AST08 - A single image plane consisting of short-integer (16-bit) pixels specifies the temperature in quanta of 0.1 K (NEΔT ≤ 0.3 K). Output is T multiplied by 10. (Parameter #3803, Level 2).

Surface Emissivity AST05 - Five image planes consisting of 16-bit pixels specify the emissivity in quanta of 0.001. Output is multiplied by 1000. The possible emissivity range of 0-1 is thus encoded as 0 - 1000. With its guaranteed precision of ±0.3 K, ASTER is capable of measuring ε within about ±0.004 (at λ=10 μm and 300K). Current engineering projections of NEΔT=0.2 K correspond to ±0.003 emissivity. (Parameter #2124, Level 2).

1.3 Algorithm Status

The TES algorithm was originally developed and tested on a desk-top computer at the University of Washington (UW). This version processed data vectors but not images. The application code for images is a *C*-language program implemented as EOS Beta-level software at JPL and also on DEC Alpha computers at UW. The Beta software corresponded to ATBD Version 2.0. Delivery Version 1 corresponded to ATBD Version 2.3. Delivery Version 2 includes minor updates reflected in ATBD Version 2.4. The development and application versions have been tested on the same data and yield the same results, and the Japanese and American versions likewise yield the same results. TES processes an ASTER image (~700x700 pixels) in about 5 minutes on a DEC Alpha-3000/900 computer running at 275 Mhz under OSF-1.

This ATBD is Version 2.4 and includes responses to ATBD review suggestions and peer criticism (Appendix A). Otherwise, it is substantially the same as Version 2.3 (August, 1996) and no changes have been made to the code. Version 1 (Hook *et al.*, 1994) was the version that was previously peer-reviewed. It documented the two algorithms favored at the time by the TEWG: the Normalized Emissivity Method and the Alpha-Derived Emissivity Method. Beginning with Version 2.0 (Gillespie *et al.*, 1995), these algorithms were incorporated into a single new program, TES, which is now the only supported algorithm. The chief advantage of TES is its greater accuracy and precision. Versions 2.1 and 2.2 updated the TES documentation and describe minor changes in the algorithm: Equation 6 in Version 2.0 disagreed with the Beta version of the code and was corrected in Version 2.1, for example. Beginning with Version 2.1 the cloud-detection algorithm (for QA) was invoked before TES (see Cothern *et al.*, 1999). The discussion of QA was new to Version 2.3. In Version 2.4, a more complete listing of tests and test parameters used within TES has been given. Version 2.4 has been published in abbreviated form in the peer-reviewed literature (Gillespie *et al.*, 1998), and reviewers' criticisms have been incorporated in Version 2.4 of the ATBD. Future changes are expected to be minor, since TES appears to perform satisfactorily. An update to Version

2.4 is anticipated shortly: this update will include minor changes in the regression coefficients resulting when the regression line was based on the 980-sample ASTER TIR spectral library instead of the smaller library available in 1996.

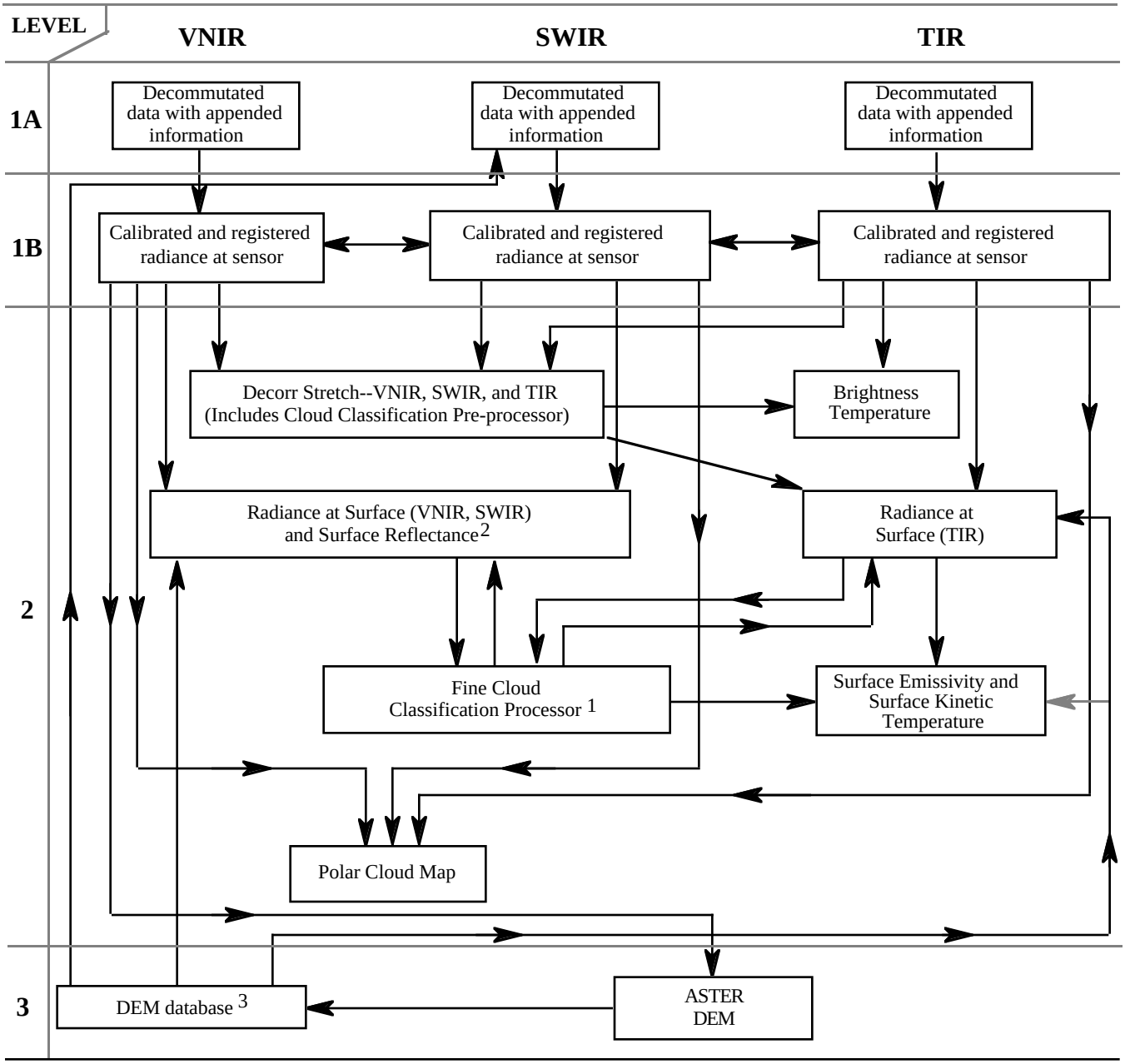

1. Produces a cloud mask that is incorporated into other products
2. Computed simultaneously with Radiance at Surface
3. Refers to a database of DEM data regardless of the source

Figure 2. Product Interdependencies.

1.4 ASTER Product Interdependencies

The ASTER TES algorithm operates in a network of other algorithms processing ASTER data. Figure 2 shows the main interdependencies of the data and processes within ASTER. A more detailed view of the processing flow specific to TES is

shown in Figure 3 (§3). Interdependencies with MODIS, MISR and other EOS products exists also, for example for atmospherically corrected ASTER data to produce the "Radiance at Surface" standard products. Those affecting TES directly are shown in Figure 3.

2. BACKGROUND

ASTER products AST08 and AST05 are intended to provide standard and reliable estimates of land surface temperature and emissivities that have known characteristics of accuracy and precision. It is desirable to produce "seamless" images -- in other words, there should be no sudden discontinuities in the Standard Products that do not reflect similar discontinuities on the ground. "Seams" can be introduced by classification. It is also a goal to maximize precision as well as accuracy, using a single algorithm embodying the simplest approach feasible.

2.1 Scientific Objectives and Justification

ASTER is the only high-spatial-resolution surface imaging system on Terra. As a result, ASTER addresses a variety of unique science objectives. The main contributions of ASTER to the EOS global-change studies will be in providing land-surface kinetic temperatures, surface emitted and reflected radiances, cloud properties, and digital elevation models (DEMs) at spatial scales that will permit detailed studies. The TES algorithm is critical to two of those contributions.

ASTER's five channels of thermal-infrared data permit the separation of measured radiances into a single surface kinetic temperature and an emissivity pseudo-spectrum, without having to make such broad assumptions about the surface emissivity as required when using one- or two-channel broad-band thermal scanners. Broad-band scanners are of greatest use over oceans, for which emissivities are well known. ASTER's capability is of greatest use over the land surface, for which emissivities are not known in advance.

The ASTER land-surface temperature product will have applications in studies of surface energy and water balance as required by climate, weather, and biogeochemical models. It can be used to aid in the quantification of evaporation and evapotranspiration, and the interactions between vegetation, soils, and the hydrologic cycle. Temperature data will also be used in the monitoring and analysis of volcanic processes. The ASTER emissivity product also contains information on the composition of the surface and is therefore useful for mapping studies. The emissivity information, alone in the remote-sensing arsenal, permits unique estimates of silicate minerals, the fundamental constituents of rocks and soils.

Terra will carry two other surface-imaging instruments in addition to ASTER. They are the Multi-angle Imaging Spectro-Radiometer (MISR) and the Moderate-Resolution Imaging Spectrometer (MODIS). Temperature and emissivity data from ASTER will be used to create data sets on a scale that permits ready validation by field experiments and, at the same time, can be used to understand the averaged response of the lower-resolution systems.

2.2 Previous Approaches to Temperature/Emissivity Separation

TIR radiation (8-14 μm) is emitted from a surface in proportion to its kinetic temperature and emissivity. The basic problem in estimating temperature and emissivity from remotely sensed data is that the data are non-deterministic: there are more unknowns than measurements (because there is an emissivity value for each image band, plus the kinetic temperature and atmospheric parameters). Historically, the chief reason for TIR measurements has been to estimate surface kinetic temperatures. This task is made easier if the emissivities are known *a priori* because the remote-sensing problem can then be made deterministic. Suitable targets thus include the oceans, for which emissivities have been measured independently and are essentially the same everywhere (e.g., Masuda *et al.* 1988).

Inversion of the TIR equations for T and ε have been attempted using deterministic and non-deterministic approaches. The former are restricted to areas for which one or more of the unknowns is known. Historically the chief reason for TIR measurements has been to estimate temperatures. This task is deterministic for important scenes for which ε is not in question: the ocean, snowfields and glaciers, and closed-canopy forests. However, most deterministic solutions require that the atmospheric parameters in equation 1 be measured directly and the measured radiance corrected for them, and this is not always feasible. Most ocean-temperature studies have utilized data from the Advanced Very High Resolution Radiometer (AVHRR), which has two channels, at 10.3-11.3 μm and 11.5-12.5 μm, thereby "splitting" the TIR spectral window. Joint analysis of the two "split-window" channels can compensate for atmospheric effects while solving for T (e.g., Barton, 1985; McMillan and Crosby, 1984; Prabhakara *et al.*, 1974). Split-window algorithms rely on empirical regression relating surface radiance measurements to water temperatures. A version of the split-window algorithm has been developed for EOS/MODIS images (Brown, 1994).

Several authors have examined extending the "split-window" technique to land surfaces (e.g., Price, 1984; Becker, 1987; Vidal, 1991). They all conclude, however, that large errors arise there due to unknown emissivity differences. Over land, the unknown emissivities are a greater source of inaccuracy than atmospheric effects. Inaccuracy of only 0.01 in ε causes errors in T sometimes exceeding those due to atmospheric correction (Wan and Dozier, 1989). In general, land emissivities can not be estimated this closely, and must be measured if accurate kinetic temperatures are to be recovered. As

a result, the usefulness of split-window methods for land is limited and the non-deterministic nature of TIR remote sensing must be addressed head-on. Many geologic studies, however, have utilized enhancements such as decorrelation stretching that do not recover T and ε (Kahle et al., 1980; Abrams et al., 1991). A spectral-unmixing approach has been used to separate a non-linear measure of T from ε, but the separation is imperfect (Gillespie, 1992).

In all, we examined ten inversion methods for the general land-surface problem in creating TES (Appendix B). These algorithms: determine spectral shape but not T; require multiple observations under different conditions; assume a value for one of the unknowns; assume a spectral shape; or assume a relationship between spectral contrast and ε. All require independent atmospheric correction. The temperature-independent spectral indices (TISI) of Becker and Li (1990), thermal log residuals and alpha residuals (Hook *et al.*, 1992); and spectral emissivity ratios (Watson, 1992a; Watson *et al.*, 1990) recover spectral shape. The day-night two-channel method (Watson, 1992b) solves the problem of indeterminacy in principle. In practice, however, this approach magnifies measurement "noise" greatly and requires "pixel-perfect" registration between the two images. Other techniques have been based on an assumed value for a "model" emissivity at one wavelength (Lyon, 1965), or an assumed maximum emissivity (ε_{max}) value at an unspecified wavelength (normalized emissivity method, or NEM) (Gillespie, 1985; Realmuto, 1990). These approaches are unsatisfactory for ASTER because inaccuracies tend to be high (±3 K) and because tilts are introduced into the ε spectra. One method required only that the emissivity be the same at two wavelengths (Barducci and Pippi, 1996). However, this assumption is commonly violated for ASTER, with only five channels. Finally, the "alpha-derived emissivity" (ADE) method utilized an empirical relationship between the standard deviation and mean emissivity to restore amplitude to the alpha-residual spectrum, thereby recovering T also (Hook *et al.*, 1992; Kealy and Gabell, 1990; Kealy and Hook, 1993). The ADE method, however, relies on Wien's approximation to invert equation 1, thereby introducing slope errors into the ε spectrum. The Mean-MMD method avoids Wien's approximation and uses a modified ADE empirical relationship based on the minimum-maximum emissivity difference (MMD) (Matsunaga, 1994).

The MODIS team has considered an approach in which emissivities are specified by classifying VNIR/SWIR data (Wan, 1994). Although important scene types such as vegetation are readily identified in the VNIR and have well known ε spectra, classification is ineffective for many geological materials. It also creates sharp boundaries in images of gradual transitions.

2.3 Conceptual Framework for TIR Remote Sensing

Temperature is not an intrinsic property of the surface; it varies with the irradiance history and meteorological conditions. Emissivity is an intrinsic property of the surface and is independent of irradiance. The radiance from a perfect emitter (i.e., a blackbody for which ε = 1.00) is exponentially related to temperature, as described by Planck's Law:

$$B_\lambda = \frac{c_1}{\pi\lambda^5}\left(\frac{1}{\exp(c_2/(\lambda T)-1}\right) \qquad (1)$$

B = blackbody radiance (W m^{-2} sr^{-1} μm^{-1}) — λ = wavelength (μm)
c_1 = $2\pi h c^2$ (3.74×10^{-16} W m^2; 1st radiation constant) — T = temperature (K)
h = 6.63×10^{-34} W s^2 (Planck's constant) — c = 2.99×10^{8} m s^{-1} (speed of light)
c_2 = h c/k (1.44×10^{4} μm K; 2nd radiation constant) — k = 1.38×10^{-23} W s K^{-1} (Boltzmann's constant)

The radiance R from a real surface, however, is less by the factor ε: $R_\lambda = \varepsilon_\lambda B_\lambda$. ASTER integrates radiance emitted from a number of surface elements. This radiance is attenuated during passage through the atmosphere, which also emits TIR radiation. Some of this radiance is emitted directly into the scanner ("path radiance"); some strikes the ground and is then reflected into the scanner. For most terrestrial surfaces the reflectivity ρ and ε are complements (Kirchhoff's Law): $\rho_\lambda = 1 - \varepsilon_\lambda$. A simplified expression for the measured radiance L is:

$$L_{x,y,\lambda} = \tau_{x,y,\lambda}\left(\varepsilon_{x,y,\lambda}B_\lambda\left(T_{x,y}\right)+\rho_{x,y,\lambda}\left(S\downarrow_{x,y,\lambda} + \sum_{m=-\infty}^{\infty}\sum_{n=-\infty}^{\infty} R^*_{x+m,y+n,\lambda}\right)\right)+S\uparrow_{x,y,\lambda}. \qquad (2)$$

x, y = position in scene — τ = atmospheric transmissivity
$S\downarrow$ = downwelling atmospheric irradiance — $S\uparrow$ = upwelling atmospheric path radiance
R* = radiance emitted from adjacent scene elements

Equation 2 describes only the radiance at a single wavelength, and only radiance from homogeneous isothermal surfaces. In practice, the radiance is measured over a band of wavelengths; however, errors due to this integration are smaller than those due to ASTER measurement uncertainties. For most terrestrial surfaces $\sim 0.7 \le \varepsilon \le 1.0$ (Prabhakara and Dalu, 1976),

although surfaces with $\varepsilon < 0.85$ are restricted to deserts. Radiance emitted at 10 μm from a surface at 300 K is on the order of 10 W m^{-2} sr^{-1} μm^{-1}. For a sea-level summer scene, typical values of the atmospheric variables (midlatitude, summer, 23-km visibility and 3.36 cm column water) estimated by the MODTRAN 3.5 atmospheric radiative transfer model are $\tau \approx 60\%$, $S\uparrow \approx 2.7$ W m^{-2} sr^{-1} μm^{-1} and $S\downarrow \approx 7.8$ W m^{-2} μm^{-1} (the reflected downwelling radiance for ε=0.9 will be ~0.25 W m^{-2} sr^{-1} μm^{-1}). One effect of $S\downarrow$ is to reduce the spectral contrast of the ground-emitted radiance, because of Kirchhoff's Law. It is necessary to compensate for atmospheric effects, including $S\downarrow$, if T and ε_λ are to be recovered accurately. Incident radiance from adjacent scene elements (pixels) varies with terrain roughness (Li *et al.*, 1998) but is typically less than $S\downarrow$ and is usually ignored. Therefore, the remote-sensing problem reduces to $L \approx \tau \varepsilon B(T) + \tau \rho S\downarrow + S\uparrow$. Equation 2 ignores effects due to heterogeneity, view angle, and the atmospheric point-spread function, as does TES.

Scene heterogeneity... At the 90-m scale of ASTER TIR pixels, many terrestrial surfaces consist of multiple components having different emissivity spectra and temperatures. Each component adds to the number of unknowns, while the number of measurements is unchanged. ASTER TIR measurements for such complex surfaces are not sufficient to estimate all the unknowns; instead, it is necessary to determine only an effective T and ε spectrum for each pixel. This simplification is standard in TIR remote sensing and is not specific to TES. Further discussion is found in Appendixes C and D.

View-Angle Effects... ASTER views the surface at a range of angles. Although the maximum viewing angle is limited to ±11° from nadir, in rugged terrain with steep slopes the local emergent angle, as calculated from a DEM, may be as high as 45°. It is thought that view-angle effects in TIR are less than in VNIR or SWIR. Field measurements have indicated that view-angle effects on emissivity spectra are greatest for the simplest scenes: e.g., for single leaves or smooth cobble faces. Complexly structured scenes such as forests or even alluvium appear to emit TIR energy isotropically, in accordance with Lambert's Law. In addition, the orientation of an emitting surface in rough and vegetated scenes is independent of topographic slope (Gu and Gillespie, 1998). Therefore, the local emergent angle calculated from a DEM may give a misleading over-estimate of the significance of non-Lambertian emittance for some rough surfaces.

In ASTER data, directional discrepancies between brightness and kinetic temperature may be greatest for snow or ice (Dozier and Warren, 1982). Even for ice or closely packed snow, however, emissivity differences are ≤0.005 for viewing angles of 45° or less (Wald, 1994). Wald and Salisbury (1995) measured differences in quartzite powders of 0.015, although values for a quartzite slab were as large as 0.1 at 8.3 μm, in the reststrahlen band. Thus, only for extreme viewing angles and surface types will directional effects exceed the target performance levels for TES. Nevertheless, brightness temperatures measured up-sun or down-sun may differ more than this because of shadowing. Correction for this phenomenon requires detailed knowledge of surface roughness and is experimental, better suited for special than standard products.

Other directional effects such as the increasing atmospheric absorption at high view angles are accounted for during atmospheric correction, as are direct effects of elevation. Correcting for viewing geometry itself is a more difficult issue, and requires that the photometric properties of the imaged surfaces be known. However, BRDFs differ with scene composition: in the VNIR, at least, forest stands behave differently than gravel surfaces, and even among gravel surfaces there may be significant (>10%) reflectance differences due just to clast size and shape distributions. Our experiments with TIR radiosity models (App. D) suggest a similar complexity for emitted radiation also. Identification of the correct photometric parameters would require some sort of scene classification, or ancillary data such as SAR backscatter coefficients, not available from Terra. Furthermore, TIR measurements are complicated by the fact that ground-emitted radiance depends on the thermal history and thermal inertia of the scene element, as well as exchange of energy with nearby scene-facing terrain elements. Our studies into adjacency effects have convinced us that corrections for terrain, viewing geometry, and adjacency effects are the subject of research and that it is premature to incorporate them in ASTER standard products.

Atmospheric Point-Spread Function... Forward scattering of the ground-emitted radiance by the atmosphere mixes radiance among neighboring scene elements. The effect is most severe for a cool scene element among neighboring warm ones. Provided the point-spread function is known, the data can be unmixed by deconvolution. TES does not undertake this task.

3. TES ALGORITHM

The Temperature/Emissivity Separation (TES) algorithm combines attractive features of two precursors and some new features (Fig. 1). It is most closely related to the Mean-MMD (MMD) method (Matsunaga, 1994), itself based on the Alpha-Derived Emissivity (ADE) technique (Kealy and Gabell, 1990; Hook *et al.*, 1992; Kealy and Hook, 1993). . Essentially, the TES algorithm uses the Normalized Emissivity Method (NEM) (Gillespie, 1985) to estimate T, from which emissivity ratios are calculated (RATIO algorithm). These "β" values are the NEM emissivities normalized by their average value. Watson *et al.* (1990) and Watson (1992b) showed than emissivity band ratios were insensitive to errors in temperature estimation, and this is true of the normalized β spectra also. The β spectrum preserves the shape, but not the amplitude, of the actual emissivities. To recover the amplitude, and hence a refined estimate of the temperature, the MMD is calculated and

used to predict the minimum emissivity (ε_{min}). TES operates on ASTER "land-leaving TIR radiance" data that have already been corrected for atmospheric τ and $S\uparrow$ (Palluconi *et al.*, 1994). The same ASTER standard product reports $S\downarrow$, which cannot be removed without knowledge of ε. TES removes reflected $S\downarrow$ iteratively, before estimating the NEM T (Schmugge *et al.*, 1995). TES also differs from precursors in: (1) refining the value of ε_{max} used in NEM, pixel by pixel; (2) correcting inaccuracies in ε_{min} for graybodies (e.g., vegetation) caused by errors in MMD due to NEΔT; and (3) compensating for reflected down-welling sky irradiance. Finally, TES estimates and reports pixel-by-pixel accuracies and precisions for T and ε, in a QA data plane that is part of the ASTER standard product. In Figure 1 and subsequent discussion the TES code is subdivided into modules named for the algorithms they derive from.

The significant advance of the TES algorithm is to produce unbiased and precise estimates of emissivities and, therefore, improved estimates of surface temperatures for the land surface. The differences between the TES and MMD algorithms are:

1) TES regresses the minimum emissivity (ε_{min}) to the maximum-minimum difference (MMD) of the ratioed emissivities calculated from ASTER radiances to improve the accuracy of the recovered emissivities and the shape of the spectrum.
2) TES uses a power-law, rather than linear, regression, to improve performance for the wide range of emissivities encountered on land surfaces.
3) TES compensates for systematic errors in the ASTER emissivities for near-graybodies due to measurement imprecision and inaccurate estimation of the maximum emissivity.
4) TES corrects for downwelling sky irradiance.

For most scenes the TES algorithm can recover temperatures with an accuracy and precision of 1.0-1.5 K, assuming accurate radiometric measurements. Emissivities can be recovered with an accuracy and precision of 0.010-0.015. TES's performance over land and sea are comparable. ASTER TES temperature recovery is not as accurate as that of the MODIS split-window algorithm for sea surfaces because: 1) ASTER resolution is better by an order of magnitude and its SNR is accordingly lower; and (2) the ASTER TIR channels are all at wavelengths in the 8-12µm window in which the atmosphere is similarly absorptive (typically, $\tau \approx 0.6$). In any case, ASTER's data acquisition plan is focused on the land surface. Major limitations on algorithm performance arise from two main sources: (1) the reliability of the empirical relationship between emissivity values and spectral contrast; and (2) compensation for atmospheric factors. Measurement accuracy and precision contribute to TES errors, but to a lesser degree.

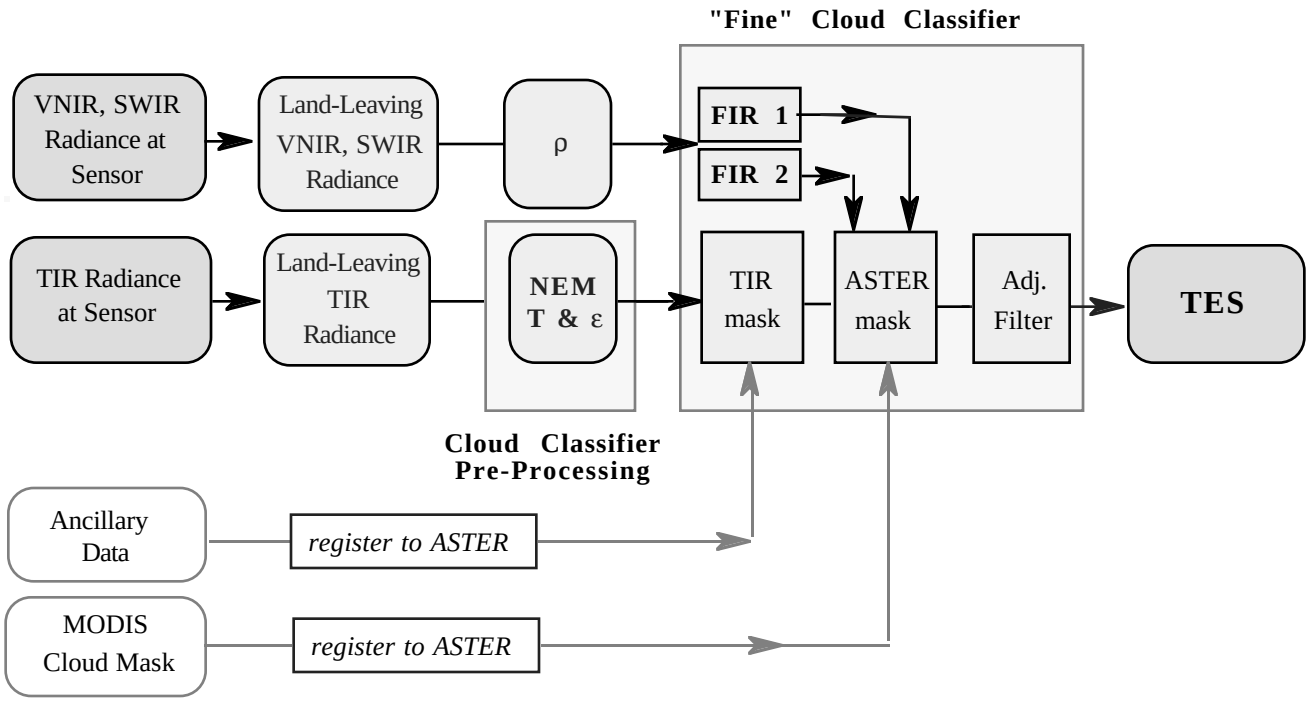

Figure 3. ASTER Processing flow diagram showing the generation of the QA cloud mask for Land-Leaving Radiance, VNIR/SWIR reflectance (ρ), and TES T and ε Standard Products. The mask is created before TES to minimize processing complexity, since TES may not always be invoked but the mask is nevertheless required for the lower-order products; this necessitates estimating T and ε, using the NEM algorithm. "FIR" refers to the finite-element filter used in the classification (Smith *et al.*, 1994). "Adj. Filter" is a spatial filter that defines regions subject to cloud adjacency effects.

Data processing stream... TES is executed in the ASTER processing chain after calculating AST09 (Land-Leaving TIR Radiance) and creation of the ASTER cloud mask, as summarized in Figure 3. No higher-level Standard Products depending on TES are generated. The main data stream for TES itself begins with the land-leaving radiance TIR radiance. The intermediate steps shown in Figure 3 all are needed for the cloud mask, which is part of the ASTER Quality Assurance (QA) report for TES and other Standard Products. The cloud mask does not create a classified map of cloud types and characteristics; it identifies pixels for which the surface is obscured, and for which atmospheric corrections used in calculating the land-leaving radiance product are likely to be in error. The algorithm that does this is identified as the "Fine Cloud Classifier" in Figure 3, to distinguish it from the predictive cloud maps that will be used in editing ASTER acquisition and processing schedules.

The "Fine Cloud Classifier" relies on the ASTER VNIR/SWIR reflectance (ρ) data, the MODIS Cloud Mask, and ancillary information such as geographic location and the date or season of image acquisition. ASTER TIR data, processed by the NEM algorithm to estimate T and ε, are used to test candidate clouds identified from the other data sources. The MODIS Cloud Mask and the Ancillary data streams are shown dashed in Figure 3 because their use has been only tentatively explored. The classification of the ASTER ρ data is based on separate finite impulse response filters (FIRs) for optically thick and thin clouds. These FIRs maximize contrast between foreground (cloud) and background (land surfaces) (Smith *et al.*, 1994). Thresholding produces a preliminary cloud mask which, combined with data from the MODIS Cloud Mask, is passed to TES to become part of the QA record attached to each output image. An algorithm similar to a low-pass spatial filter ("Adj. filter" in Fig. 3) is applied to the mask to identify "perimeter" pixels on the edge of or near to clouds, for which $S\downarrow$ is likely to be much higher than estimated by the atmospheric models used in calculating the land-leaving radiance. Night-time cloud identification must be on the basis of TIR and ancilary data alone. The production of the ASTER cloud mask is documented in a separate ATBD (Cothern *et al.*, 1999).

Sky irradiance... The TES algorithm compensates for reflected sky irradiance ($S\downarrow$). This term is relatively unimportant unless the reflectivity is high (emissivity is low). For example, $S\downarrow$ contributes little error in recovery of sea-surface temperatures, because the reflectivity for water is only ~1.5%. For rocks and soils, with lower emissivities and higher reflectivities, $S\downarrow$ is more important.

The TES algorithm uses an iterative approach to remove reflected $S\downarrow$ and refine estimated emissivities (e.g., Schmugge *et al.*, 1995) before proceeding with the RATIO and MMD modules. Compensating for reflected down-welling sky irradiance is done in two stages of generations of processing. The first stage consists simply of refining the NEM estimates of emissivity in a loop, using the emissivity value as an estimate of scene reflectivity. These reflectivities are less accurate than the rescaled TES emissivities; therefore, once the first-generation TES emissivities are found the sky-irradiance compensation is repeated, now using the using first-generation TES T and ε to refine the correction for $S\downarrow$, leading to a more accurate second-generation TES T and ε. This approach is effective provided emissivities are large or sky temperatures are much lower than land temperatures, but it is inaccurate for cold ground under a warm sky.

Performance... For most scenes the TES algorithm can recover temperatures with an accuracy and precision of <1.5 K, assuming accurate radiometric measurements. Emissivities can be recovered with an accuracy and precision of <0.015. TES's performance over land and sea are comparable. TES temperature recovery is not as accurate as that of the MODIS split-window algorithm for sea surfaces because: (1) ASTER resolution is better by a factor of 11, and the SNR is accordingly lower; and (2) none of the ASTER TIR channels is at wavelength at which the atmosphere is absorptive. In any case, ASTER's data acquisition plan is focused on the land surface. Major limitations on algorithm performance arise from two main sources: (1) the reliability of the empirical relationship between emissivity values and spectral contrast; and (2) compensation for atmospheric factors. Measurement accuracy and precision contribute to TES errors, but to a lesser degree.

Organization of presentation... Details of the algorithm follow an overview of TES from a strategic viewpoint (§3.1). In §3.2 there is a discussion from a processing viewpoint, breaking the algorithm into its component sections or modules. In §3.3 critical assumptions are discussed and justified, as are the internal tests of performance. In §3.4 the factors limiting the accuracy and precision of the algorithm are identified. Radiance data simulated from laboratory emissivity spectra and also acquired by an airborne scanner are used to test TES. Final sections §3.5 and §3.6 outline diagnostics and exception handling, including the design of the QA data planes.

3.1 TES Overview

The TES algorithm starts with TIR data that have been corrected for atmospheric transmissivity and path radiance (ASTER standard product AST09, "Land-Leaving TIR Radiance" or L': Palluconi *et al.*, 1994). AST09 also reports sky irradiance, $S\downarrow$. The first step in TES is to estimate the emissivities from L', using the Normalized Emissivity Method (NEM). These are used, along with Kirchhoff's Law, to estimate the amount of L' that is due to reflected $S\downarrow$, and that amount is subtracted from

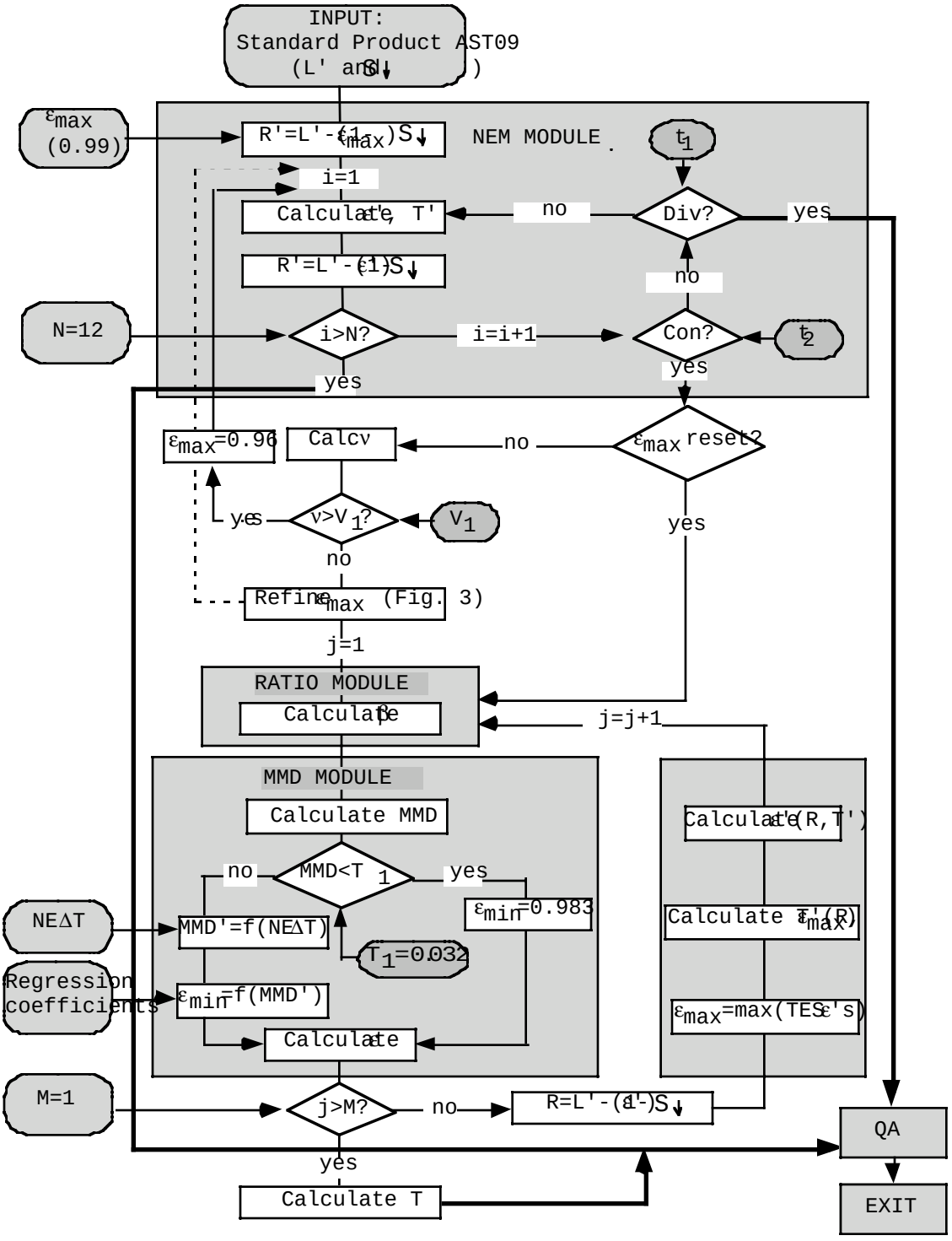

Figure 4. Detailed flow diagram of TES, schematic in places. Divergence (Div) and convergence (Con) tests determine if iterative correction for $S\downarrow$ will work. Div is $\Delta^2 R/\Delta i^2 < t_1$; Con is $R'_{i+1}-R'_i < t_2$ and terminates iteration when R is stable. The assumed value for ε_{max} in the NEM module is refined if the spectral variance is small (see Fig. 5). ε_{min} found in the MMD module is compensated for measurement error. TES ε values are used to refine R. QA consists of TES performance and product characteristics and encoding them in reserved data planes (Fig. 7). *The reference to Fig. 3 is a typographic error; it should read Figure 5.*

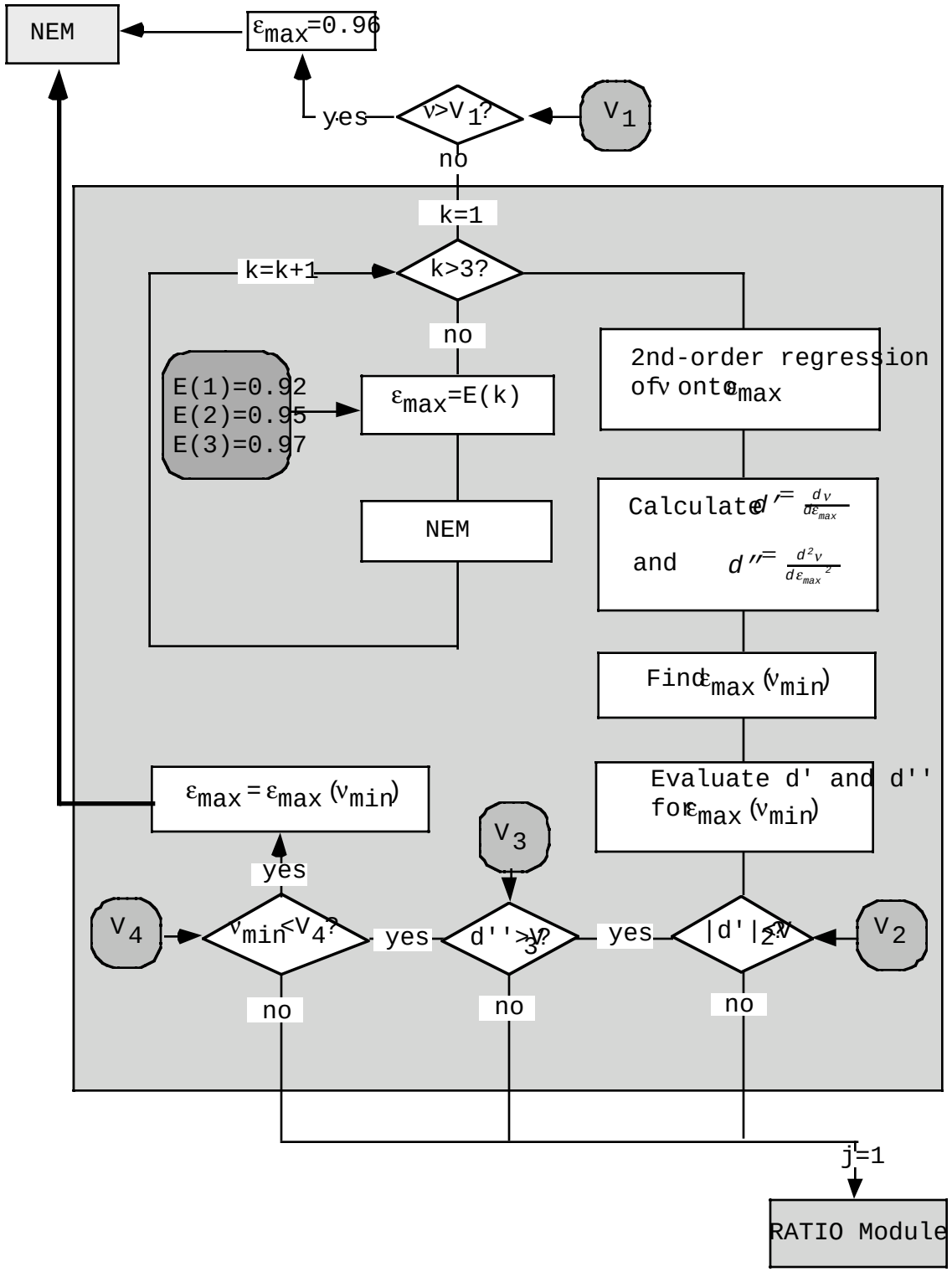

Figure 5. The NEM module in TES, with detailed treatment of the estimation of ε_{max} for near-graybodies. Parameter $\varepsilon_{max}(\nu_{min})$ is the value of ε_{max} that minimizes spectral variance ν. The first test ($\nu<V_1$?) excludes spectra with high variance from refinement. The second test ($|d'| < V_2$?) excludes sloping or structured spectra, and the third test ($d'' > V_3$?) excludes convex and flat spectra. Like the first test, ($\nu_{min} < V_4$?) excludes all but graybody spectra. Tests on the regression are applied in the window $0.9 \le \varepsilon_{max} \le 1.0$. TES will not be accurate for non-natural graybodies such as metals having $\varepsilon_{max} < 0.9$. Test parameters and their values are summarized in Table 3.

L' iteratively to estimate the emitted radiance, R, from which a temperature T is calculated, again by the NEM module. From T and R the RATIO module calculates an unbiased estimate of spectral shape. The key issue now is to estimate the amplitude of the emissivity (ε) spectrum, using the MMD regression and the normalized emissivities. After the actual emissivities are calculated, it remains to recalculate the surface temperature from these values and R. Throughout, corrective algorithms are applied to refine assumed values, based on the measured data and measures of TES' performance. Figure 4 presents a flow chart of the main processing steps in the TES algorithm.

3.2 Processing

Below, the steps of the TES algorithm are presented in sufficient detail to permit regeneration of the processing code. The input image data sets consist of "Land-Leaving TIR Radiance," L', and sky irradiance, $S\downarrow$. Several parameters and thresholds may be adjusted from their default values as the need arises. These parameters are identified below. The output data sets consist of five emissivity images, corresponding to ASTER channels 10-14, and a single temperature image.

3.2.1 Estimating the surface temperature and subtracting reflected sky irradiance (NEM module)

The surface temperature is first estimated using the normalized emissivity approach (Fig. 5; App. B). Essentially, the value of the maximum emissivity for bands 10-14, ε_{max}, is assumed in order to calculate a temperature and the other emissivities from L'. These emissivities permit iterative correction for reflected down-welling sky irradiance, $S\downarrow$. An empirically based process, described below, is used to refine ε_{max} for nearly flat emissivity spectra, as determined by a low variance for the NEM spectra. To begin, ε_{max} is assumed to be 0.99, at the high end of the range for graybody materials such as vegetation.

Upon entry to the NEM module, radiance R_b in each band b is estimated by $R'_b = L'_b - (1 - \varepsilon_{max})\ S\downarrow_b$. Subtracting $(1-\varepsilon_{max})\ S\downarrow$ accounts for part of the reflected sky irradiance. In our discussions, we use R', T' and ε' to refer to interim values of R, T and ε, before iterative correction for $S\downarrow$ is complete. The NEM temperature is taken to be the maximum temperature calculated from R'_b for image channels b=10-14:

$$T' = \max(T_b); \quad T_b = \frac{c_2}{\lambda_b}\left(\ln\left(\frac{c_1\varepsilon_{max}}{\pi R'_b \lambda_b^5} + 1\right)\right)^{-1}; \quad \varepsilon'_b = \frac{R'_b}{B_b(T_b)} \tag{3}$$

where c_1 and c_2 are the constants from Planck's Law (Eq. 1). Once T' is known, NEM emissivities ε'_b are calculated and used iteratively to re-estimate $R'_b = L'_b - (1- \varepsilon'_b)\ S\downarrow_b$. This process is repeated until the change in R'_b between steps is less than threshold value t_2, or until the number of iterations exceeds N, which is currently set to 12 (Fig. 4, 5). The current default value for t_2, 0.05 W m^{-2} sr^{-1} μm^{-1} per iteration, is determined by the maximum predicted value of NEΔR. If the slope of R'*vs.* iteration increases between iterations (exceeds t_1 = 0.05 W m^{-2} sr^{-1} μm^{-1} per iteration^2) correction for $S\downarrow$ is not possible. Execution of TES is aborted, and the NEM T and ε are reported along with a warning flag in the QA plane. Correction for $S\downarrow$ is typically <1 K unless the sky is warmer than the ground or humidity is high. Because error introduced during correction depends on ε, it is possible to recover accurate temperatures from the high-ε image channel even if the rest of the spectrum is inaccurate.

Therefore, if any values of ε'_b fall outside a permitted range ($0.5 < \varepsilon'_b < 1.0$) as the iterations progress, calculations for the affected pixel are halted and an error condition is noted as described above. This test is not indicated in Figures 4 and 5. The accuracy of the temperature product under these conditions needs further evaluation. The default range for emissivities also needs further testing.

The value for ε_{max} was chosen to be representative of common graybody spectra such as vegetation, water or snow. However, actual values of ε_{max} will vary from pixel to pixel, even if the scene does consist of these materials. It may be possible to improve on the estimate of ε_{max} by analysis of the measured data for each pixel: the best value for ε_{max} minimizes the variance ν of the NEM emissivities. Plotting ν against possible values of ε_{max} yields an upwards-opening parabola. A new value of ε_{max} may be found by calculating $\nu\left(\frac{1}{5}\sum\varepsilon_b\right)^{-2}$ for ε_{max} = 0.92, 0.95, and 0.97 in addition to 0.99, and fitting a parabola to the data. If this curve has a minimum for $0.9 \le \varepsilon_{max} \le 1.0$, it indicates the best estimate of ε_{max}. In this case, the NEM module is executed again to find a new NEM T. This approach gives useful results only if there is little detail in the actual emissivity spectrum. Therefore, it is only invoked if ν calculated for ε_{max} = 0.99 is less than an empirically determined threshold value, $V_1 = 1.7\text{x}10^{-4}$ (Fig. 5).

The refinement for ε_{max} depends on being able to define a minimum variance. If the parabola is too flat and sloped, a reliable minimum cannot be defined, even if there is a mathematical solution. Therefore, additional tests required. In the second test, if the absolute value of the average slope of the ν *vs.* ε_{max} curve is greater than $V_2 = 1.0 \times 10^{-3}$, the refinement attempt is aborted. In the third test, if the second derivative is less than $V_3 = 1.0 \times 10^{-3}$ the parabola is considered to be too flat for a reliable solution. Finally, even if ν_{min} can be determined, its value may be so low that the emissivity spectrum is essentially a graybody. The final test, $\nu_{min} < V_4$? ($V_4 = 1.0 \times 10^{-4}$), detects exceptionally flat spectra. In all these cases, if the test is failed $\varepsilon_{max} = 0.983$ is assumed.

One consequence of the threshold test (for V_1) is that ε_{max} may be refined for vegetation, but not for most rocks. In case $\nu \geq V_1$ the pixel is assumed to be rock or soil, and the value of ε_{max} is reset to 0.96, the midrange value ($0.94 \leq \varepsilon_{max} < 0.99$) for rocks and soils in the ASTER spectral library. NEM temperatures passed to the RATIO module should be accurate within ±3 K at 340 K, and within ±2 K at 273 K, provided atmospheric correction is successful. A second consequence is that the refinement of ε_{max} is most effective in the absence of measurement error. Numerical simulations suggest that refinement will be effective, at least sometimes, for ASTER data.

Further experimentation with ASTER images simulated from airborne scanner data is required in order to determine threshold values and the overall value of refining ε_{max} in terms of improved TES performance. In any case, the threshold values will be sensitive to NEΔT and must be refined as improved estimates become available.

3.2.2 Ratio algorithm (RATIO module)

The relative emissivities, β_b, are found by ratioing emissivities, calculated from the NEM T and the atmospherically corrected radiances, to the average emissivity:

$$\beta_b = \varepsilon_b \, 5 \, (\Sigma \varepsilon_b)^{-1}; \quad b = 10, 14. \tag{4}$$

Because emissivities themselves are generally restricted to $0.7 < \varepsilon_b < 1.0$, $0.75 < \beta_b < 1.32$. The errors in β due to inaccuracy in the NEM estimate of T are systematic but less than the random errors due to NEΔT, for $240 < T < 340$ K. Warping of the β spectrum is below the threshold of detectability for ASTER data.

3.2.3 Estimating TES emissivities and temperature (MMD module)

The β spectrum must next be scaled to actual emissivity values, and the surface temperature must be recalculated from these new emissivities and from the atmospherically corrected radiances. These TES T and ε values are the reported ASTER Standard Products. An empirical relationship predicting ε_{min} from MMD is used to convert β_b to ε_b. We established this regression using laboratory reflectance and field emissivity spectra (Hook and Kahle, 1995), as documented in §3.3.

The first step in the TES algorithm is to find the spectral contrast:

$$\mathrm{MMD} = \max(\beta_b) - \min(\beta_b); \qquad b = 10 \; - \; 14 \tag{5}$$

from which the minimum emissivity is predicted and used to calculate the TES emissivities:

$$\varepsilon_{min} = 0.994 - 0.687 * \mathrm{MMD}^{0.737}; \qquad \varepsilon_b = \beta_b \left(\frac{\varepsilon_{min}}{\min(\beta_b)} \right); \qquad b = 10 \; - \; 14; \tag{6}$$

Provided the actual emissivity contrast in a scene element is much greater than the apparent contrast due only to measurement error, MMD is an unbiased estimate. For graybodies, however, MMD is dominated by measurement error and is no longer unbiased. That is, as the true spectral contrast is reduced to zero, MMD is also reduced, but to a positive limit whose value depends on the NEΔT. It is possible to correct the apparent MMD *pro forma*, as specified by Monte Carlo simulations:

$$\mathrm{MMD'} = [\mathrm{MMD}^2 - c \, \mathrm{NE}\Delta\varepsilon^2]^{-1}; \quad c = 1.52 \tag{7}$$

where MMD' is the corrected contrast, NE$\Delta\varepsilon$=0.0032 is calculated from NEΔT=0.3°K at 300K, and the coefficient c was determined empirically. Equation 6 improves the accuracy of TES for graybodies, but at the expense of precision. We have found that if MMD<T_1 (currently set to 0.032), the loss of precision becomes unacceptable. Therefore, when this is the case, MMD' is not calculated and ε_{min} is not found from equation 6 but instead is set to 0.983, a value appropriate for graybodies such as vegetation, and processing continues. The optimum *pro forma* correction has not yet been determined, and deserves further study before launch and during the Initial Check-Out (ICO) period after launch.

The NEM T for rocks and soils is likely to be in error by up to 3 K because the assumed value of ε_{max} may be inaccurate. This error can be reduced by recalculating T from the measured, atmospherically corrected radiances R and the TES emissivity spectrum:

$$T = \frac{c_2}{\lambda_{b^*}}\left(\ln\left(\frac{c_1\varepsilon_{b^*}}{\pi R_{b^*}\lambda_{b^*}^5 R}+1\right)\right)^{-1}. \quad (8)$$

where b* is the ASTER band for which emissivity ε_b is maximum (and correction for $S\downarrow$ is minimum).

3.2.4 Final correction for sky irradiance and bias in β

The TES ε and T values are more accurate than the NEM values. Recalculation of the TES ε and T values improves their accuracy further. To do this, first the TES ε values are used instead of the NEM values to make a final single (non-iterative) correction to L' for reflected $S\downarrow$, and then the new estimates of R are used with the TES T instead of the NEM T to recalculate the β spectrum (Eq. 4). Then improved TES ε and T are calculated as before. Experience shows that there is little gain if this process is repeated more than once (M=1, Fig. 4). For a variety of simulated and real radiance measurements the "refined" TES emissivities changed by as much as 0.01; therefore, this final correction is worth doing.

3.3 Regression of ε_{min} onto MMD

The relationship between emissivity and spectral contrast is a key feature of the TES algorithm. It was initially established by analysis of 86 laboratory reflectance spectra supplied by J.W. Salisbury (pers. comm., 1994), equivalent to emissivity by Kirchhoff's Law. The data were converted to ASTER pseudo-spectra and ε_{min} was found for each sample. Radiances were estimated, scaling emissivities by blackbody radiances calculated for T=300 K, and β spectra and MMD values were calculated. The ε_{min} data were then regressed to the MMD values. They are related by a simple power law (Fig. 6). The regression parameters are insensitive to the assumed temperature. Although the regression parameters are defined empirically, the relationship itself is reasonable and physically predictable if deviation from blackbody behavior is due to molecular resonance localized in narrow reststrahlen features.

The critical assumption that this regression applies to the entire gamut of surface materials remains to be proven. We have tested this assumption and, so far, it appears to be valid. A different set of 31 of Salisbury's reflectance spectra (Salisbury *et al.*, 1988, 1992) yielded nearly identical regression coefficients (H. Tonooka, Ibaraki Univ., pers. comm., 1996), as did field emissivity spectra of Australian rocks (n=91) collected using the Jet Propulsion Laboratory's μFTIR spectrometer (Hook and Kahle, 1995). Hundreds of airborne MIRACO_2LAS CO_2 laser reflectance spectra, with a narrower window than the five ASTER TIR bands, yielded a regression having similar overall characteristics (T. Cudahy, CSIRO, pers. comm., 1996). A cautionary note is warranted here: some tests of this algorithm have been conducted using libraries that contained TIR spectra that erroneously had been offset. Not surprisingly, the resulting regression curves were likewise erroneous.

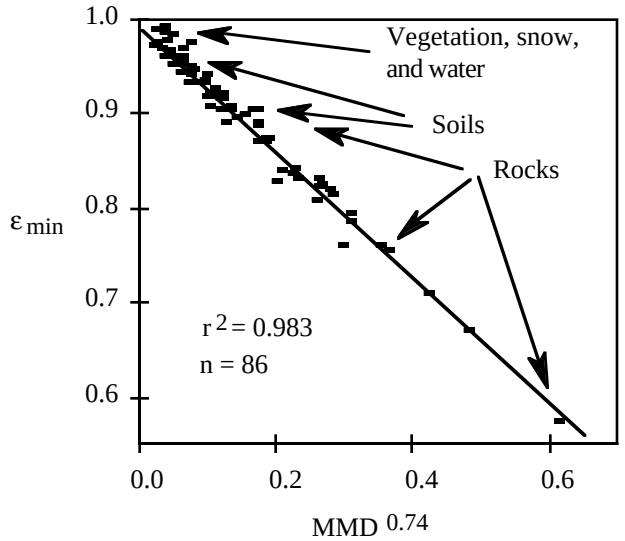

Figure 6. The empirical relationship between ε_{min} and MMD, based on 86 laboratory reflectance spectra of rocks, soils, vegetation, snow and water, provided by J. W. Salisbury in 1995. 95% of the samples fall within ±0.02 emissivity units of the regression line, corresponding to an error in T of about ±1.5 K at 300 K. The ε_{min}-MMD relationship follows a simple power law:

$$\varepsilon_{min}=0.994-0.687*MMD^{0.737}.$$

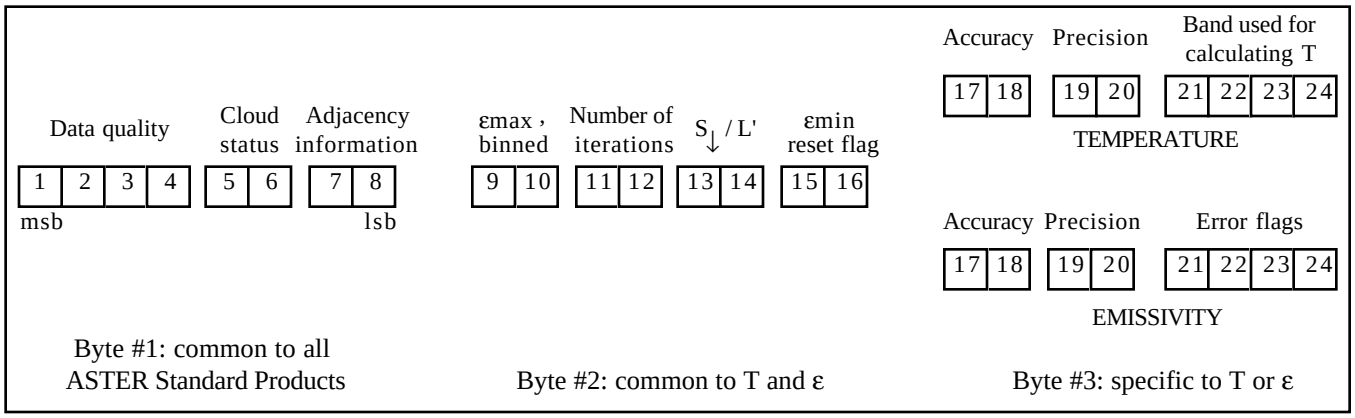

Figure 7. The general structure of the first QA data plane

The regression for the TES algorithm uses ε_{min} rather than mean emissivity as in the Mean-MMD algorithm**,** because ε_{min} was found to improve the correlation. The MMD was used because, for most spectra, it was just as good and faster to calculate than other measures of spectral complexity, such as variance. Use of the variance, however, reduces sensitivity to measurement error for the important class of near-blackbody scene components, and this choice deserves review.

The scatter of the individual samples about the regression line (Fig. 6) results in an irreducible imprecision of ~1.5 K in the TES algorithm. Coincidentally, this is about the magnitude of the scatter of data on the ε_{min} - MMD plane due to ASTER measurement error, evaluated by Monte Carlo techniques. It is also comparable to the predicted inaccuracy of the ASTER TIR data of 1 K.

3.4 Quality Assessment and Diagnostics

There are two types of quality controls for the TES algorithm: internal, automatic tests and external validation of results, detailed in §3.5 and §4, respectively. The internal tests will be conducted for every pixel, but the external validity tests will be conducted primarily just after launch, and less frequently thereafter. The validity checks will be used to assess general performance characteristics, and will also be used together with the pixel-by-pixel performance estimates to establish accuracy and precision ranges for the T and ε Standard Products. This latter information will be reported along with algorithm processing status indicators in the QA record associated with each image processed by TES.

The QA report consists of a header record and three 8-bit data planes. The QA Header, described in Geller(1996), is common to all products and consists of Level 1B processing information and QA Log information. The first 8-bit QA data plane contains shared information that is common to all data products, on a telescope-by-telescope basis (in this case, TIR). The second plane contains data relevant to the operation of TES. The third data plane contains information specific to the Standard Product, in this case T or ε. The data-plane approach was chosen because it allows for easier graphical display of housekeeping data and performance summaries, making it easier for a user to see which parts of the scene were most affected. The structure and content of the QA Header Data Planes are described below (Fig. 7, Table 2).

The first QA data plane contains three fields (Figure 7, Table 2):

1) The data-quality field. Only three QA categories ("Bad," "Suspect," "Bad") have so far been assigned specific bit patterns. The remaining bit patterns will be used to specify categories of "bad" and "suspect" pixels, based on information from developers.
2) The cloud mask field. Pixels for which the surface is obscured by optically thick clouds, obscured by optically thin clouds, haze or cirrus, or not obscured at all will be flagged. Additionally, "clear" pixels in the neighborhood of clouds will be flagged as "suspect" pixels in field 1.
3) The cloud-adjacency field. Pixels flagged as adjacent to clouds in field 2 are categorized by distance ("very near," near, "far," or "very far") from the nearest "cloud" pixel. Quantitative values for these categories will be assigned during ICO.

In Table 2, listed subdivisions of the data quality categories do not yet have bit patterns assigned, and some categories remain to be defined. Categories annotated as "All Algorithms" will apply to all higher-level data products (with the possible exception of DEMs). Bit fields applicable to a specific algorithm (e.g., TES only; DEM only) will be used for that algorithm only. As of this writing, the quantitative threshold distances for the adjacency categories are under discussion by a splinter working group of the ASTER TEWG. Also, the bit assignments for the emissivity portion of the TES product are still being discussed, and the exact way in which the accuracy and precision ranges are to be quantified from the reported indicators (primarily $S\downarrow/L'$ and proximity to cloud) and other TES parameters (e.g., MMD) has not been finalized.

Table 2a. QA data planes 1 (common to all ASTER products) and 2 (specific to both TES T and ε).

Data Plane	Field	Category	Binary Code	Description
1	Data quality	"Bad"	1111	Bad Pixel: Labeled as Bad in the Level-1 data.
				General code, algorithm or LUT failure (all algorithms)
				Algorithm or LUT returned "bad input value" flag (all algorithms)
				Algorithm convergence failure (TES only). NEM T and ε are reported.
				Algorithm divergence (TES only). NEM T and ε are reported.
				Too few good bands (TES only). No values for T and ε are reported.
		"Suspect"	0111	All bands of the input pixel are "suspect"
				Output data value is Out-of-Range (All algorithms)
				Algorithm or LUT returned "suspect input value" flag (All algorithms)
				Edited DEM pixel (DEM only)
				Some TES output bands out-of-range (TES only)
				Perimeter effect from thick cloud
				Perimeter effect from thin cloud
		"Good"	0000	Good Pixel: This pixel has no known defects
	Cloud mask	Thick cloud	10	Optically thick cloud detected
		Thin cloud	01	Optically thin cloud/haze detected
		Clear	00	No clouds detected
	Adjacency code	Very near	11	Uncorrected cloud irradiance may exceed ~30% of "typical" L'
		Near	10	Uncorrected cloud irradiance may be ~20-30% of "typical" L'
		Far	01	Uncorrected cloud irradiance may be ~10-20% of "typical" L'
		Very far	00	Uncorrected cloud irradiance probably less than ~10% of "typical" L'
2	ε_{max}	>0.98	11	vegetation, snow, water, some soils
		0.96-0.98	10	default value of ε_{max}
		0.94-0.96	01	most silicate rocks
		<0.94	00	possible error condition
	Number of iterations	≥7	11	slow to converge
		6	10	nominal performance
		5	01	nominal performance
		4	00	fast to converge
	S↓/L'	≥0.3	11	warm, humid air or cold land; correction may be inaccurate
		0.2-0.3	10	nominal value
		0.1-0.2	01	nominal value
		≤0.1	00	high altitude scene; correction probably accurate
	ε_{min} reset flag	Reset	10	ε_{min} was reduced in proportion to measurement noise
		Not reset	00	ε_{min} did not need to be corrected

3.5 Exception Handling

No attempt will be made to recover temperature or emissivities for pixels classified as "bad" in the input TIR data. This category includes transmission errors and dropped lines. Pixels identified within the TES algorithm as cloud or classified as being adjacent to clouds will be analyzed, but will be flagged as "suspect" as discussed above. Pixels identified as having cirrus cover in the MODIS products will likewise be flagged, should those products be available and adequately coregistered to the ASTER images. All other data will be processed by TES, but processed pixels failing the atmospheric-correction tests will be flagged. Specifically, should the correction for reflected $S\downarrow$ diverge or fail to converge, processing for the affected pixel will halt and the NEM T and ε values will be reported as the Standard Product instead of the TES values. For other pixels designated as "bad" output will consist of a single pre-determined default value. Any pixels with apparent $\varepsilon>1$ will be reset to 1 and the T re-calculated; any pixels with $\varepsilon<0$ will be re-set to 0.

Table 2b. QA data plane 3 for TES Standard Products T (3-T; top) and ε (3-ε; bottom).

Data Plane	Field	Category	Binary Code	Description
3-T	T Accuracy	> 2.0 K	11	poor performance
		1.5 - 2.0 K	10	marginal performance
		1.0 - 1.5 K	01	nominal performance
		< 1.0 K	00	excellent performance
	T Precision	> 2.0 K	11	poor performance
		1.5 - 2.0 K	10	marginal performance
		1.0 - 1.5 K	01	nominal performance
		< 1.0 K	00	excellent performance
	Band	Band used for calculating T	1000	ASTER band 14
			0100	ASTER band 13
			0010	ASTER band 12
			0001	ASTER band 11
			0000	ASTER band 10 (not normally used)
3-ε	ε Accuracy	> 0.020	11	poor performance
		0.015 - 0.020	10	marginal performance
		0.010 - 0.015	01	nominal performance
		< 0.010	00	excellent performance
	ε Precision	> 0.020	11	poor performance
		0.015 - 0.020	10	marginal performance
		0.010 - 0.015	01	nominal performance
		< 0.010	00	excellent performance
	Error flags		1000	ε is bad due to out-of-range or other causes
			0100	L' or S↓ were bad in input product
			0010	L' or S↓ were suspect in input product
			0001	Not all bands had valid data
			0000	No error conditions

3.6 Data Dependencies

Input data for the TES algorithm are given in Table 3. The primary inputs are the calibrated and atmospherically corrected "radiance at ground" TIR images and the sky irradiance images. The coregistered and calibrated ASTER VNIR and SWIR data are optional inputs used to recognize and flag cloudy areas. These and default parameters discussed in §3 above are required at launch. The parameters may be updated as experience is accumulated, but changes to critical ones (such as the coefficients for the ε_{min}-MMD regression) will be changed as infrequently as possible, and as close to the time of launch as possible, to ensure data conformity.

Products such as the MODIS cloud mask may not be ready until after ICO. Their use will be explored as they become available, and a decision to use or not to use them will be made as soon as possible.

3.7 Performance

We have tested the TES algorithm by numerical simulation and on three existing calibrated and atmospherically corrected TIMS multispectral TIR images (Palluconi and Meeks, 1985). In the first approach, radiances are estimated using Planck's Law and measured emissivity spectra. These results probably give the most insight into the workings of the TES algorithm itself. The ASTER simulator images, on the other hand, provide a more realistic test, but are less well understood because of the difficulty of collecting adequate spectral data in the field until recently.

Table 3. Input data for the TES algorithm

INPUT IMAGES

Product ID	Parameter/Level	Product description
ASTO9 -TIR	3817/2	ASTER radiance leaving ground
ASTO9	3817/2	Sky Irradiance
-NA-	--NA--	ASTER cloud mask
MOD35	3660/?	MODIS cloud mask

INPUT PARAMETERS

Name	Parameter description	Current Value
ε_{max}	maximum emissivity for NEM subroutine	0.990 (1st pass, 0.960 (2nd pass)
ε_{max}	default value if MMD< T1	0.983
-	gain - (ε_{min} *vs.* MMD regression)	-0.647
-	offset - (ε_{min} *vs.* MMD regression)	0.994
-	power coefficient - (ε_{min} *vs.* MMD regression)	0.737
N	maximum iterations in sky irradiance module	12
M	number of passes through TES	2
NEΔT	ASTER NEΔT	0.3K

TEST VALUES

Name	Parameter description	Current Value
L1	upper emissivity limits	0.5
L2	lower emissivity limits	1.0
V_1	Maximum variance to initiate refinement of ε_{max}	1.7×10^{-4}
V_2	Tolerance for "zero" slope of ε_{max} *vs.* ν curve	1.0×10^{-3}
V_3	Max. value for 2nd derivative of ε_{max} *vs.* ν curve.	1.0×10^{-3}
V_4	Maximum value for min. ν (ν_{min}).	1.0×10^{-4}
t_1	divergence test: max. 2nd derivative	0.05 W m^{-2} sr^{-1} μm^{-1} per iteration^{-2}.
t_2	convergence and stability test: max. 1st derivative.	0.05 W m^{-2} sr^{-1} μm^{-1} per iteration.
T_1	minimum MMD for which regression is used	0.032
c	empirical coefficient used to adjust MMD for noise	1.52

3.7.1 Numerical Simulation Results

Overall, the TES algorithm operating on error-free input radiances can recover temperatures for a wide range of surfaces within 1 K and emissivities within 0.01. For numerically simulated radiance emitted from surfaces at 300 K, based on the field emissivity spectra in our library, 95% of the recovered temperatures were within 1.5 K and 1 standard deviation = 0.3 K, for example (Fig. 8). The performance is not related to scene composition in general, but to the scatter about the ε_{min}-MMD regression line, scatter which is largely independent of MMD (Fig. 6). Monte Carlo simulation shows that the scatter of recovered temperatures due to measurement error is about the same as that due to the inherent scatter about the regression line. Recovered emissivities show little bias, but err systematically by an amount proportional to the error in temperature: if TES overestimates T by 1 K at 300 K, it will tend to underestimate ε by ~0.017.

TES results are sensitive both to T (Fig. 9) and to ε_{max} (Fig. 10), although less so than NEM results. Over the range 240 - 340 K the variability of TES T's (~0.5 K) is less than the projected inaccuracy of the ASTER measurements (1 K, Table 1). Within ASTER scenes the temperature range will typically be much smaller (e.g., 270 - 310 K) and the systematic error with T can be neglected.

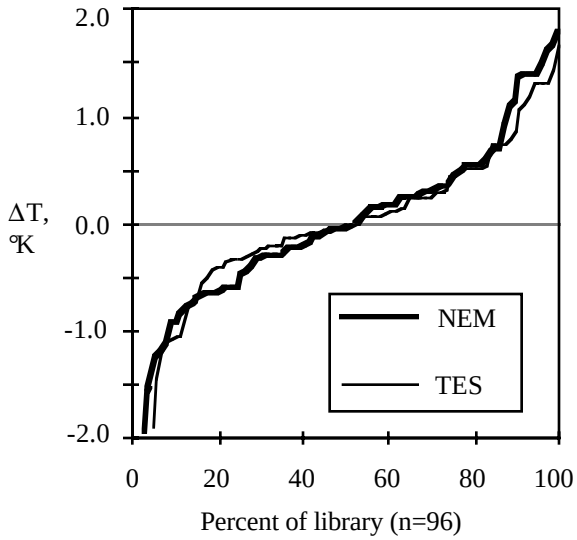

Figure 8. Temperature errors (ΔT) for the NEM and TES approaches (ε_{max}=0.97).

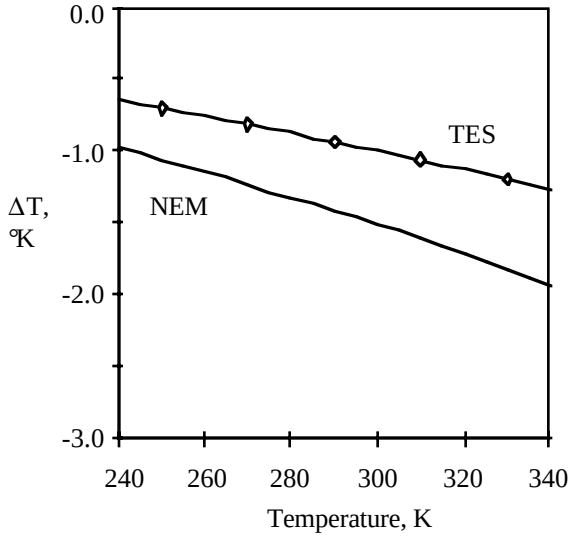

Figure 9. Accuracy of TES and NEM T is sensitive to temperature. Calculated for one sample of vegetation (ε_{max}=0.97).

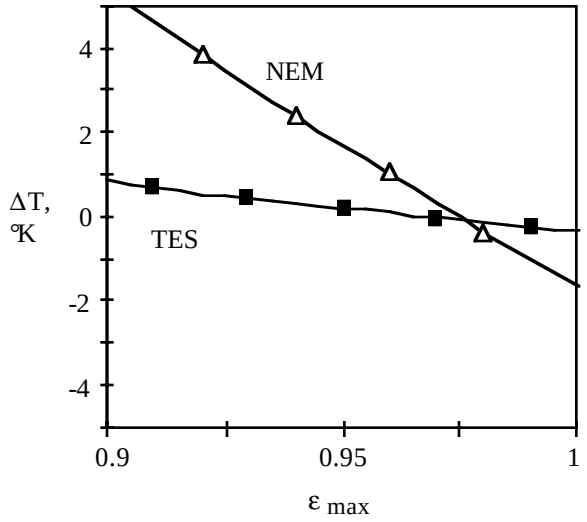

Figure 10. Apparent temperatures recovered by TES (filled squares) are less sensitive to ε_{max} than NEM temperatures (open triangles). ΔT: temperature error. Correct ε (ASTER bands 10-14): 0.964, 0.964, 0.957, 0.975, 0.971 (T=300K).

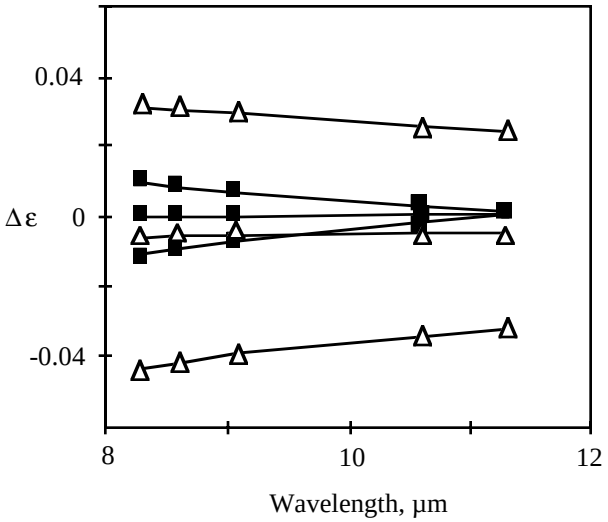

Figure 11. Apparent TES emissivities (filled squares) are less sensitive to ε_{max} than are NEM emissivities (open triangles). Δε: emissivity error. Squares and triangles are at the central wavelengths for ASTER bands 10 - 14. Values of ε_{max}: 0.94 (bottom), 0.97 (middle) and 1.00 (top). Correct ε (Quartzite; ASTER bands 10-14): 0.937, 0.907, 0.840, 0.938, 0.949 (T=300K).

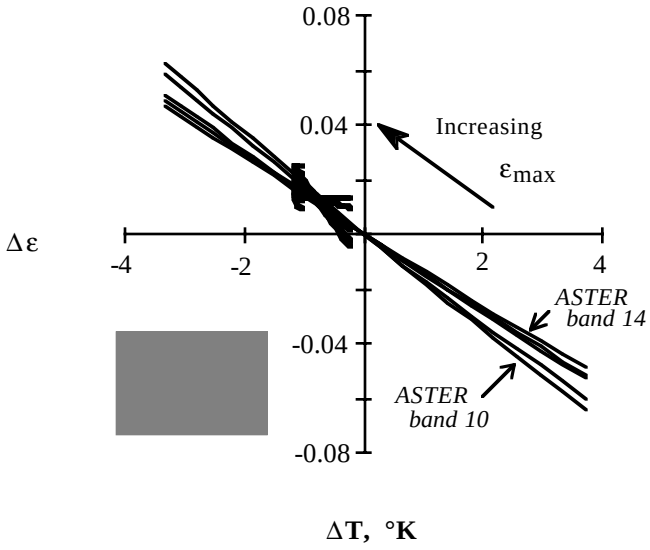

Figure 12. TES results are less sensitive than NEM results to ε_{max} (in the range $0.9 \leq \varepsilon_{max} \leq 1.0$). Emissivities for ASTER bands 10-14 are 0.937, 0.907, 0.840, 0.938, and 0.949.

A major source of error in the NEM algorithm is the assumed value of ε_{max} (Fig. 10). If ε_{max} is varied over its range measured for our spectral library (0.94 - 1.00), recovered NEM temperatures will vary by ~4 K. TES greatly reduces the dependency on ε_{max}, to about 0.5 K for the example just given. This value is less than uncertainty from other sources, and does not contribute significantly to the total error.

As the assumed value of ε_{max} is changed, the NEM ε spectrum both tilts and changes its average amplitude by ~0.06 (Fig. 11). In contrast, TES emissivities change amplitude but little. However, the tilt or bias remains. Figure 12 demonstrates the dramatically decreased sensitivity to the assumed value of ε_{max} for TES compared to NEM, for a simulated quartzite sample at 300 K. The results described above pertain to the simplest TES algorithm, in which none of the iterative corrections have been employed. Therefore, the performance limits are conservative and may be improved upon.

The first refinement allows the TES algorithm to select ε_{max} in the NEM module to minimize the variance of the NEM emissivities. For graybodies, this re-estimation of ε_{max} reduces its sensitivity to measurement error by a factor of four (Fig. 13).

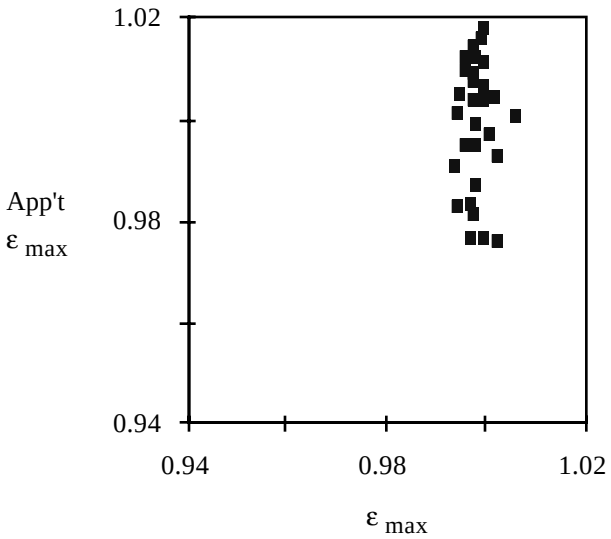

Figure 13. Apparent values of ε_{max} (y axis) calculated from simulated ASTER graybody radiance values (ε=0.9945; 300 K) with Monte Carlo measurement errors (N=30), plotted against ε_{max} refined by minimizing the NEM spectral variance (x axis).

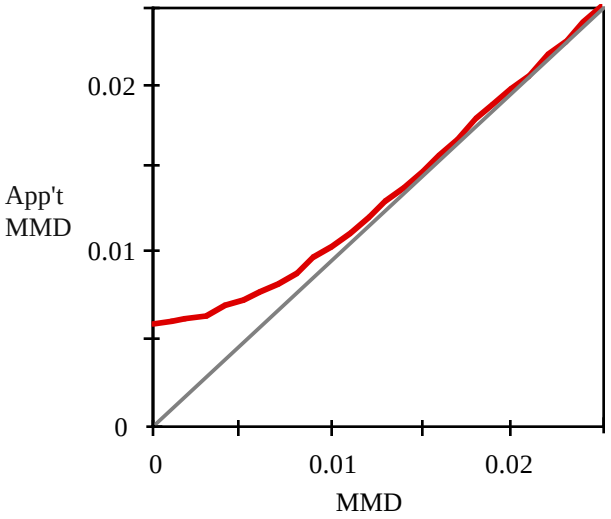

Figure 14. Random measurement errors increase the apparent MMD for graybodies (heavy line; NEΔT=0.2 K). Dashed line shows correct values.

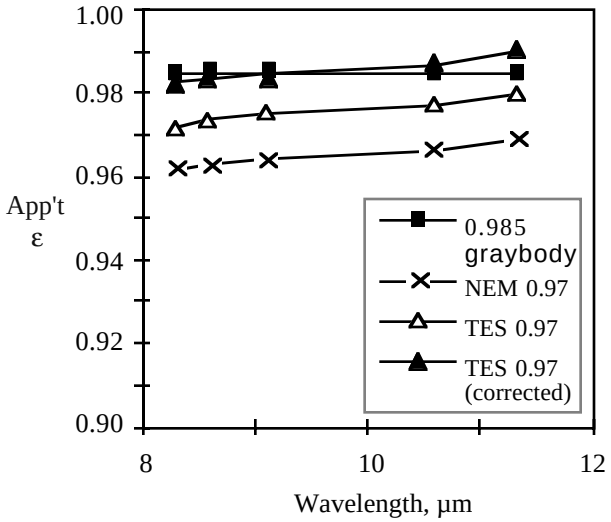

Figure 15. TES emissivities are improved by correcting the MMD, shown above for an ideal graybody of 0.985 emissivity. Assumed ε_{max} = 0.97 (300 K).

TES is not as sensitive as NEM to NEΔT. (Matsunaga (1994) argued that his Mean-MMD algorithm was more sensitive to NEΔT than the NEM algorithm, but he was referring to temperature instead of emissivity). Propagated through the TES algorithm, the effect of improving ε_{max} is at the measurement precision level for both T and ε (Fig. 12). However, the reduction to the apparent tilt of TES emissivity spectra is significant and drops it below the random noise level, such that it cannot be detected.

TES refines the apparent MMD for graybodies by a *pro forma* reduction to compensate for measurement noise (Fig. 14), which can cause a systematic overestimation of temperature by as much as 1.6 K. To correct the apparent MMD, values are first estimated for different near-graybody spectra to which random noise has been added. A third-order curve relating apparent and actual (noiseless) MMD values, found by regression, may then be used to estimate the correct MMD. Correction of the apparent MMD improves the accuracy of the recovered temperatures (decreasing them) and the TES emissivities too (inducing them) (Fig. 15). The chief improvement is in the amplitude, not the shape of the spectrum. The amount of improvement indicated in the sample of Figure 15, due only to the *pro forma* correction to MMD, is about 0.012.

The relationship between uncorrected TES and NEM emissivities will vary from sample to sample, depending on the distance of the sample (ε_{min}, MMD) from the TES regression line. It will also vary with measurement error.

Finally, TES's performance can be improved by using the TES temperature to recalculate the ratioed emissivities (β_i) and then the TES emissivities (ε_i) and T. The improvement is a function of the accuracy of ε_{max} -- if it is already correct, no further improvement is possible. However, for some samples the average emissivity can be improved by 0.01 or more, and artifactual tilt can be essentially eliminated. Figure 16 shows the effect of the successive refinements on the TES emissivity spectrum for one graybody (ε=0.9945) that plots close to the ε_{min}-MMD regression line. For this sample, the original ε_{max} is a bad estimate, and the recalculated NEM spectrum provides the best average fit of all, although the standard deviations for the recalculated NEM spectra (±0.013) are twice those of the TES spectra (±0.006). For other samples, the NEM spectra will be highly variable, but the TES spectra will be similar. Overall improvement to the TES spectra is about 0.01 emissivity units -- worth the added computation in light of the desired levels of accuracy.

Compensating for sky irradiance... Correction must be made for atmospheric attenuation, for additive path radiance, and for downward sky irradiance reflected from the scene. Correction for the first two is made in standard product AST04, "radiance at ground," possibly to the percent level, although quantitative estimates depend on factors for which are as yet uncertain. Sky irradiance may be determined to within 10%, according to current estimates, but this uncertainty too may be revised as launch nears. Below, LOWTRAN7 atmospheric models were used in numerical simulations to assess sensitivity to error in the atmospheric corrections.

TES emissivities and temperatures are modestly insensitive to 1% errors in atmospheric attenuation, which translate to uncertainties of ~0.004 in ε, but ~0.8 K in T. In comparison, respective precisions of ~0.006 and 0.3 K correspond to the NEΔT alone. Because atmospheric error is highly correlated from band to band, it is mainly the average amplitude of the

recovered emissivity spectrum and temperature that are affected by uncorrected attenuation. All three atmospheric parameters vary from band to band, however, and poor correction will impose this signature on the TES emissivity spectrum.

Upwelling sky radiance is correctable to about 1%. For a warm ground (300K) and cold sky (240K) the resulting uncertainties in ε and T are ~0.003 and 0.4 K, but for cold ground (240K) and warm skies (273K) they rise to ~0.004 and 0.6 K. These uncertainties are equivalent in size to those due to attenuation.

Uncorrected sky irradiance reflected from the ground, $(1-\varepsilon)S\downarrow$, can be a major source of inaccuracy and imprecision in the TES algorithm, especially for the recovered emissivities. It is most serious for cold rock surfaces under a warm sky, because both (1-ε) and $S\downarrow$ are large. Warm, vegetated surfaces viewed under cold skies are least affected by this source of error, because both (1-ε) and $S\downarrow$ are small (Fig. 17).

Iterative estimation of ε and subtraction of $(1-\varepsilon)S\downarrow$ from the measured radiance can correct apparent temperatures, provided $(1-\varepsilon)\ S\downarrow$ is not too large: or graybodies such as vegetation, corrected temperatures are accurate to within 0.3 K. Even for rock surfaces having low emissivities, correction is accurate to similar levels. Furthermore, error in estimating $S\downarrow$ does not contribute significantly to error in T. Therefore, reflected sky irradiance is not a factor limiting TES performance as far as recovering surface temperature is concerned.

Temperature recovery may be reliable even if $S\downarrow$ is poorly known because its determination depends mainly on the radiance from the band with the highest emissivity, and therefore the lowest amount of reflected $S\downarrow$ (Fig. 18). The recovered emissivity spectrum, on the other hand, is much more sensitive than T to $S\downarrow$. Figure 19 shows that, even after correction, $S\downarrow$

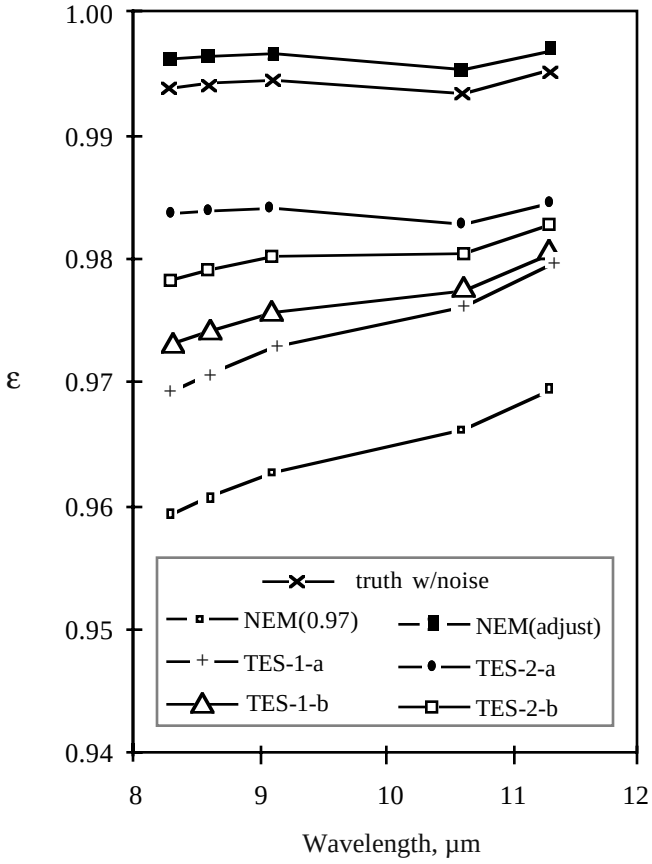

Figure 16. Mean apparent emissivity spectra (N=30) calculated for a graybody measured with ASTER NEΔT. "Truth" is calculated correctly assuming T=300 K. The lowest curve is the NEM spectrum assuming ε_{max}=0.97. The next two higher curves (TES-1 a, b) show the improvement obtained by the first pass through TES: for a, the apparent MMD was used, but for b the corrected value was (minimizing ν). The top curve (filled squares) is the recalculated NEM spectrum obtained by refining ε_{max}. In this instance, it provides the best approximation to the "truth," but this is not generally so. The remaining curves (TES-2 a, b) are TES spectra based on the recalculated NEM temperature.

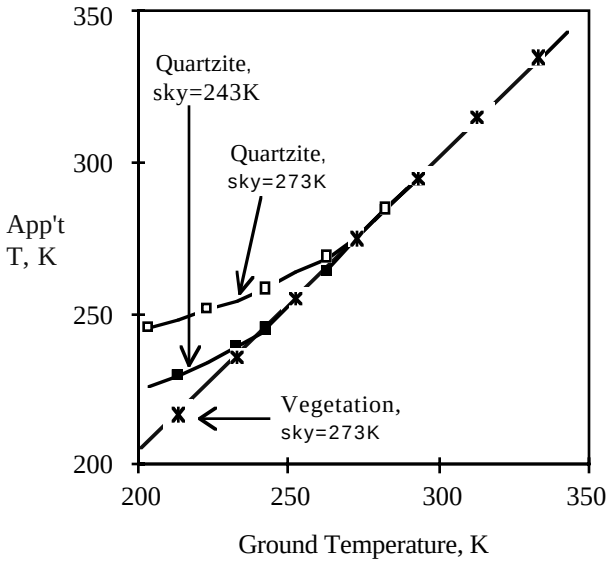

Figure 17. Apparent ground temperature T' for quartzite and vegetation increases with sky irradiance. For quartzite (ε=0.63, 0.69, 0.57, 0.95, 0.97) apparent temperatures are inaccurate for T<280K, even with a cold sky, whereas for vegetation (0.98, 0.99, 0.99, 0.99, 0.98) errors are much smaller.

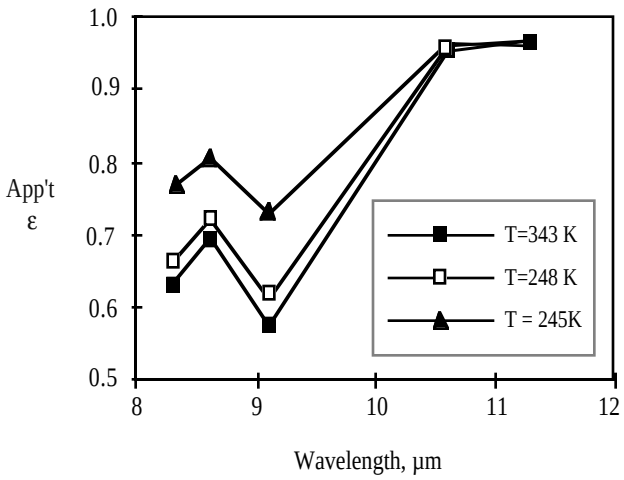

Figure 18. Impact of $S\downarrow$ on apparent emissivities is greater for lower emissivities, even after accurate correction. Shown above: TES emissivity spectra for quartzite at 245, 248 and 343 K (effective sky temperature = 243 K).

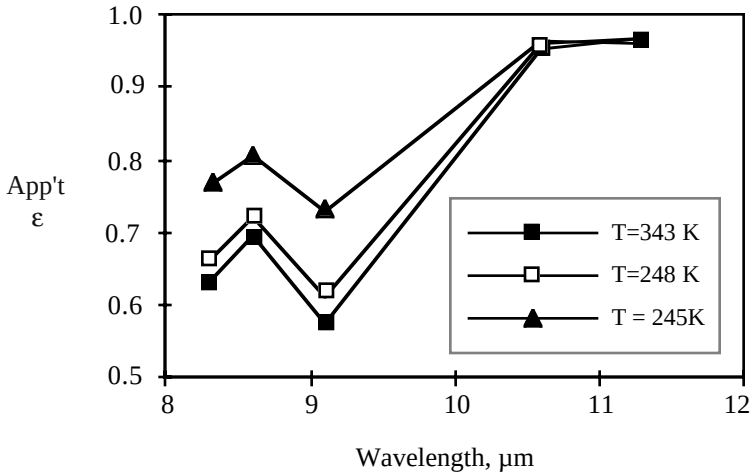

has a sizable residual impact on apparent emissivities recovered by TES. Even if $S\downarrow$ is accurately known, accurate emissivities cannot be recovered unless $(1-\varepsilon)S\downarrow \ll R$ (Fig. 19a). If this condition is met, then for many circumstances emissivities for even quartzite, with its low emissivities in ASTER bands 10-12, can be recovered with errors less than 0.01. Because $S\downarrow$ may not be known with less than 10% error, Figure 19a probably presents an overly optimistic view of TES

performance. Figure 19b shows the impact on apparent TES emissivities of uncorrected $S\downarrow$, at the 10% level. These results suggest that uncorrected $S\downarrow$ is the dominant source of emissivity error for geologic materials unless they are imaged under very favorable conditions, with high ground temperatures and clear, thin skies. On the other hand, uncorrected $S\downarrow$ is not an source of significant error (i.e., <0.01) for important scene components: vegetation, snow and water, as well as spectrally flat rocks and soils.

If $(1-\varepsilon)S\downarrow$ is a large fraction of the measured radiance, the TES sky-irradiance correction code requires more iterations to converge on an accurate answer. Typically, temperatures will converge quickly to an accurate value, but apparent emissivities may take longer to converge, or may even diverge with each successive iteration. For quartzite at 310 K viewed under a cold sky (230 K effective temperature), appropriate values for both ε and T were recovered on the first iteration; if the sky temperature is 273 K, convergence occurs for ε after six iterations. However, if sky and ground temperatures are the same, the emissivities never converge, although the correct temperature is found after only four iterations.

Correction for sky irradiance is highly depended on sample characteristics and scene conditions. Under the best conditions, uncertainties in estimating $S\downarrow$ have no significant impact; under other conditions even well-determined $S\downarrow$ cannot be successfully removed from the data, unless ε is known *a priori.*

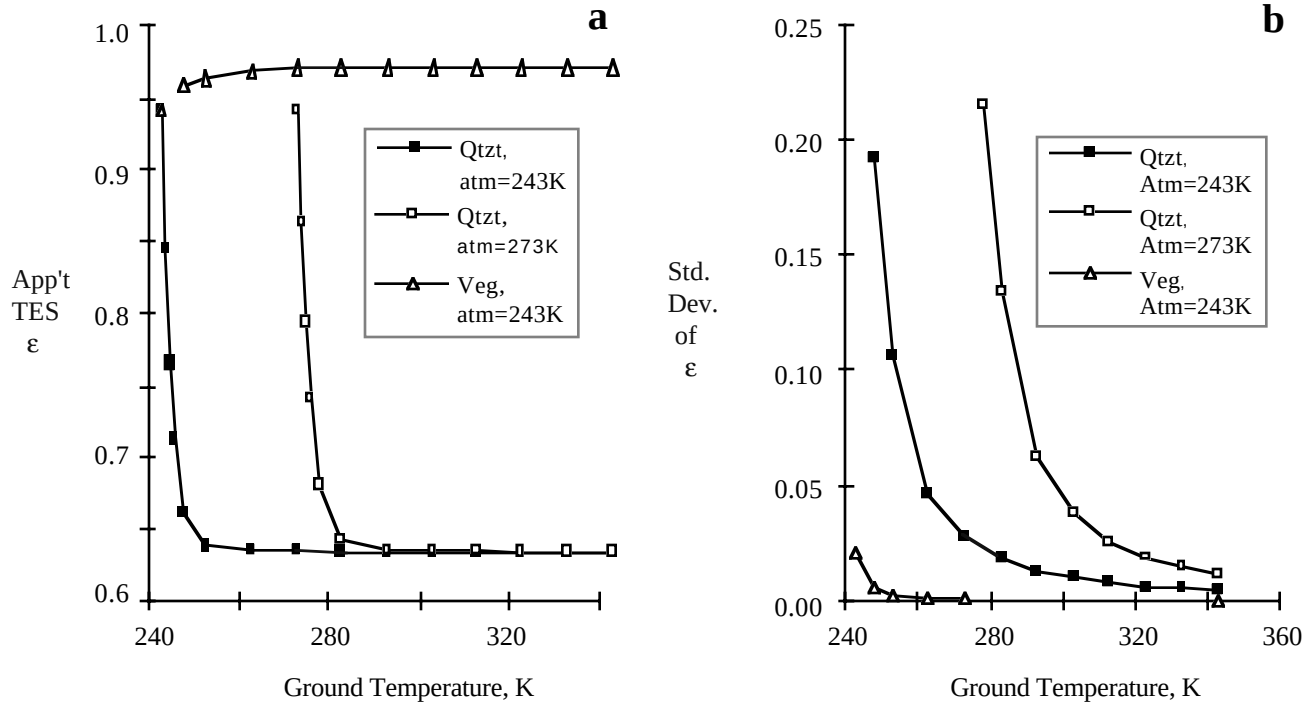

Figure 19. Apparent emissivities (ε_{10}) corrected for $S\downarrow$ are increasingly accurate (a) and precise (b) as the temperature contrast between atmosphere and ground increases. **a.** $S\downarrow$ is known accurately and precisely. Apparent emissivities converge to correct values if the ground temperature is 20 K or more greater than the effective sky temperature. **b.** $S\downarrow$ is known within ±10% (1σ). Uncertainty of the apparent emissivity is <0.01 for vegetation even at 260 K, but only under the most favorable circumstances (cold, sky, warm ground) for quartzite.

3.7.2 Tests on Simulated ASTER Images

The airborne TIMS, with NEΔT ≈ 0.2 K (Palluconi and Meeks, 1985), is appropriate for simulating ASTER's TIR images because ASTER bands 10-14 correspond closely to TIMS bands 1-3, 5 and 6. The MODIS Airborne Simulator, MAS simulates some, but not all, of ASTER's TIR bands. MASTER is a clone instrument to MAS, but simulates all of ASTER's bands (Table 4). Landsats 4, 5 and 7 all measure TIR radiances, but do not match ASTER's performance. The TIR imaging spectrometer SEBASS can be used to simulate ASTER data, but is not generally available. The FSI scanner is not deployed on aircraft and simulates only three of ASTER's bands. It is useful mainly for ground measurement.

Table 4. Validation TIR Imagers and ASTER

Instrument	Reference	No. bands	Band Centers, μm (8-12μm)	Band Widths, μm	Resolution	$NE\Delta T_{300K}$	FOV
ASTER	Kahle et al., 1991	5	8.3, 8.65, 9.05, 10.6, 11.3	0.4-0.7	90m	0.3K	5°
Landsat 7		1	11.5	2.1	120m	1K	15°
TIMS	Palluconi and Meeks, 1985	6	8.3, 8.7, 9.3, 9.6, 10.6, 11.3	0.3-1.1	5-20m	0.2K	95°
MAS	King *et al.*, 1996	5	8.6, 9.8, 10.6, 11.0, 12.0	0.4-0.6	50m	0.1K	86°
MASTER	Hook and Tan, 1998	12	8.6, 9.7, 10.4, 11.0, 12.6	0.4-0.6	25-50m	0.1K	86°
SEBASS	Hackwell *et al.*, 1996	90	every 50-70 nm	0.05	0.4-5m	0.05K	7°
FSI	FLIR Systems, Inc.	3	8.2, 8.7, 11.2	0.3-1.7	0.01-1m*	0.3K	34°

** at ranges of 1-100 m*

TIMS and MASTER images are calibrated using internal blackbody measurements, atmospheric data, and surface temperature measurements. Radiosonde atmospheric probes and Reagan Sun Photometer measurements of total water vapor, together with MODTRAN and FASCODE atmospheric models (e.g., Abreu *et al.*, 1991; Anderson *et al.*, 1993; Clough et al., 1981; Kniezys *et al.*, 1996), can be used to estimate the three atmospheric parameters (τ, $S\downarrow$ and $S\downarrow$) at the time of overflight and as a function of view angle (e.g., Realmuto, 1994). From these data the ASTER atmospheric corrections can be duplicated. Surface temperatures are measured with an Everest radiometer. Three simulated ASTER images (Fig. 20) have been prepared from calibrated TIMS overflights of Castaic Lake and Lake Tahoe, both in California, and of the south coast of Hawai'i (Realmuto *et al.*, 1992). These images are used to test T and ε recovery over water targets (low MMD). An additional image has been prepared over a geologic target, the playa in Railroad Valley, Nevada, and is used to test recovery over land areas having high MMD (Fig. 21).

The Castaic Lake image is of a reservoir, the earthen dam that impounds it, and sparsely vegetated hills (Realmuto, 1994). Lake surface temperatures of 287.9 ±0.3 K were measured at 49 locations. Boat trails visible in the image were 2 K colder. TIMS radiances, with correct emissivities, indicate a water temperature of 289.0±1.6 K, about 1.1 K too high. TES T was ~290.6 K. The average TES emissivities were correspondingly low (~0.05). Deviations from laboratory spectra were most pronounced in bands 10 and 14. Emissivities for a stand of trees showed the same pattern, subdued. Correcting for sky irradiance reduced TES T by ~0.2 K. We attribute the inaccurate atmospheric to incorrectly calibrated hygristors in the radiosondes, a problem that was corrected in 1997.

The Lake Tahoe image includes the lake and forested, snowy mountains (not shown in Fig. 20). The subscene in Figure 20 is of Dollar Point, a subdivision with roads and houses. Water, air, and melting snow temperatures were ~280.3 K, ~283.1 K, and ~273.1 K, respectively. Corresponding TES T values were 281.0±0.4, 283.9±0.6, and 273.7±0.4 K, respectively. Assuming forest and air temperatures were the same, the mean TES T's were systematically 0.4-0.8 K too high, but within the uncertainty predicted from the numerical simulation studies. If the band 10 and 14 radiances were adjusted by empirical gain factors designed to "flatten" the recovered Castaic water spectra, TES ε spectra for both Lake Tahoe water and snow were flat. Snow spectra averaged 0.973±0.006, ~0.011 lower than laboratory values. Recovered water spectra had an rms error of only 0.004 compared to laboratory data. Forest spectra were less well fit, with an rms error of 0.026.

The Hawai'i image shows an active lava flow entering the ocean near Kapa'ehu, accounting for the plume-like patterns in the water and for the wide range of temperatures there. A cloud of steam drifts west (left) from the entry point. Concentrations of SO_2 are also present nearby. SO_2 absorbs strongly in the 8-12 μm region of the spectrum and is not accounted for by the atmospheric corrections. Away from Kapa'ehu, ocean temperatures measured by Realmuto *et al.*, (1992) three days before overflight were ~296 K (~330 K near the entry point). Corresponding TES T = 305±0.6 K, ~9 K higher than the earlier radiometric temperatures. Recovered emissivities are too low by 0.05 (band 10) to 0.02 (band 12). Uncorrected absorption by SO_2 and other gases from the lava may account for the excessive apparent temperatures. Correcting for sky irradiance reduced TES T by ~0.5 K.

Railroad Valley images for three successive years (1995-1997) were analyzed. Figure 21 shows the playa, shallow ponds surrounded with reeds, and alluvial fans in 1996. Figures 21a, b and c show radiance, TES T, and TES ε images, respectively; Figure 21d is a decorrelation-stretched false-color version of the same scene, indicating clearly the spectral homogeneity of the playa validation site (A). Results from 1995-96 were consistent with those from California and Hawai'i. Running TES without band 10 cut pond temperature discrepancies in half. After correcting the radiosondehygristor calibration in 1997, TES emissivities for the pond and playa sites were brought into agreement with and laboratory and field measurements (Fig. 22). Precisions for ε for homogeneous areas on the images were ≤0.006. We attribute some of the rms "error" of 0.018 for the playa to difficulties in comparing spectra made at different scales (6.4 m *vs*. 10 cm). This may especially be true for band 5, which only overlaps with the field data at the 2-σ level. Band 5 spans the carbonate emssivity feature near 11.5 μm, and the field spectra, but not the TIMS data, may indicate the local presence of carbonates on the playa.

TES pond temperatures were 290.8±0.4 K, 1.7°K less than the buoy temperatures. Because of evaporation, water skin temperatures may be as much as 4°K lower than buoy temperatures. TES temperatures of 314.2 ±0.3 K for playa site E were indistinguishable from Everest radiant temperatures of 314.3±0.9 K (n=99, ε=0.93).

Correcting for sky irradiance in the TES algorithm reduced apparent water temperatures by ~0.2 °K for the California and Nevada sites, and ~0.5 °K for Hawai'i.

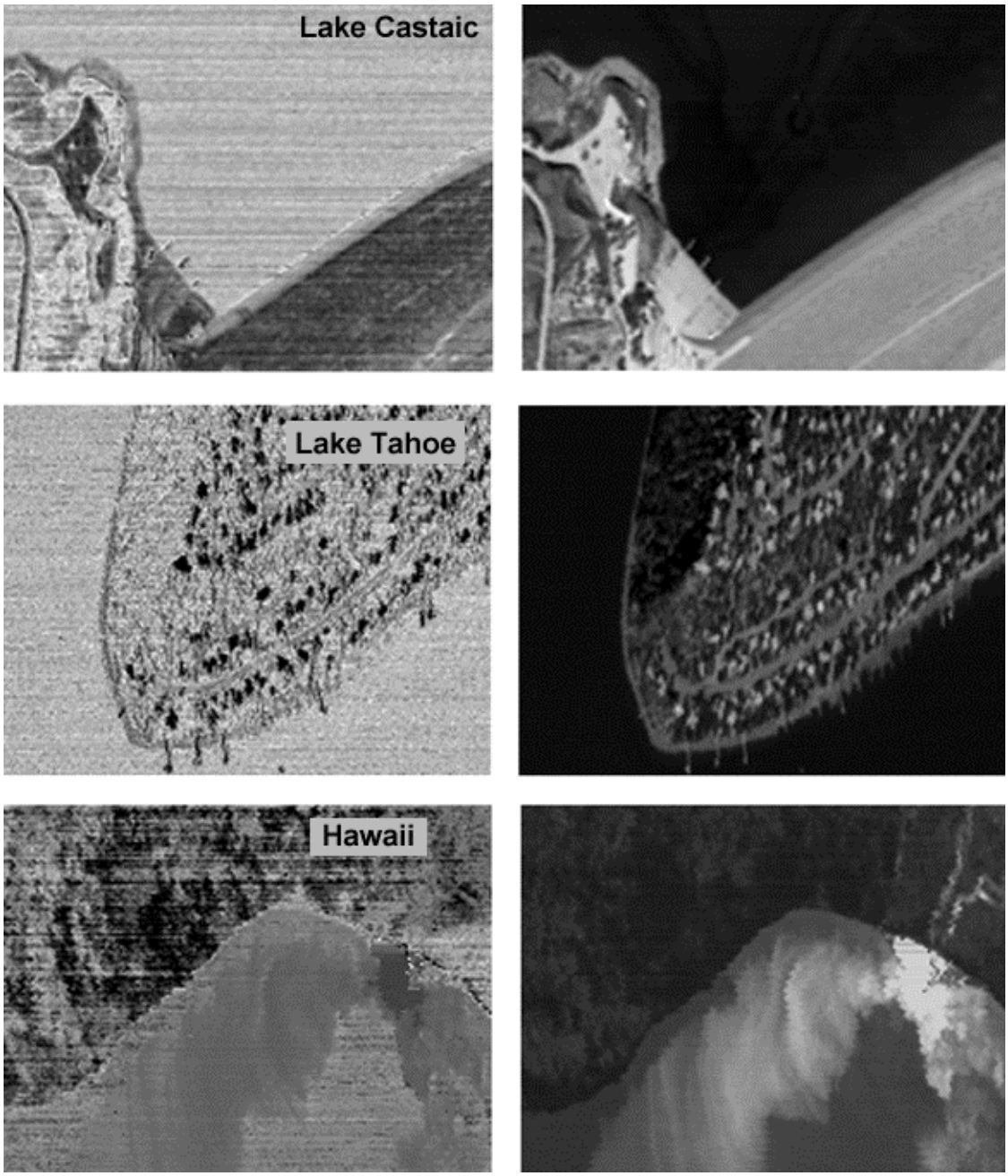

Figure 20. TES results from simulated ASTER images acquired by TIMS over Castaic Lake (~900 m amsl; 9 March 1994), California, Lake Tahoe, California (~2000 m amsl; 28 May, 1995), and the south coast of Hawai'i (1 October 1988). Left: ε_{10}. Stretched images appear "noisy" because the scene has low MMD. Right: temperature. Subscenes are 100 x 200 pixels or about 0.6 x 1.2 km; resolution is ~5.5 - 7.5 m/pixel.

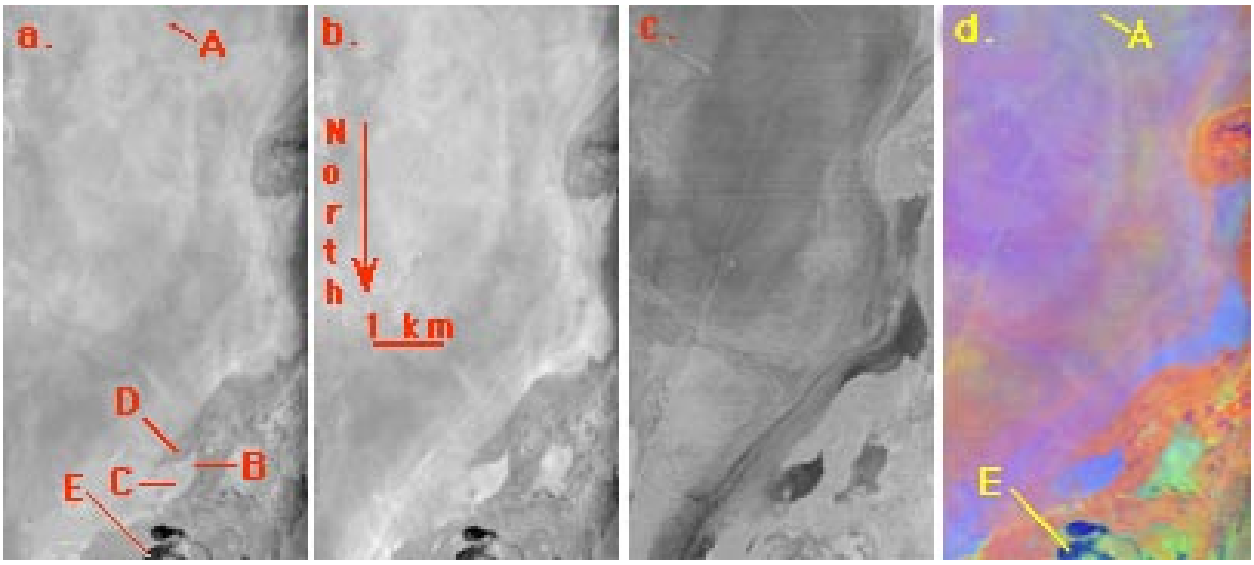

Figure 21. TES results from simulated ASTER data acquired by TIMS over Railroad Valley playa (~1750 m amsl), 1 June 1996. North is to the left; image is ~20 km high.; resolution is ~15 m/pixel. **a.** TIMS Radiance data, simulated ASTER band 13 (10.6 µm), showing test areas for which field temperatures and laboratory reflectance spectra were measured: A, playa center; B and C, shore; D, yardangs; E, ponds. **b.** Temperature image recovered by TES. **c.** Emissivity image, ASTER band 12, recovered by TES. Due to exposed geologic materials, MMD was as high as 0.15. **d**. False-color decorrelation-stretched image made from ASTER bands 10=B, 12=G, and 13=R. Decorrelation stretching subdues correlated radiance variations due to scene temperatures and exaggerates spectral differences.

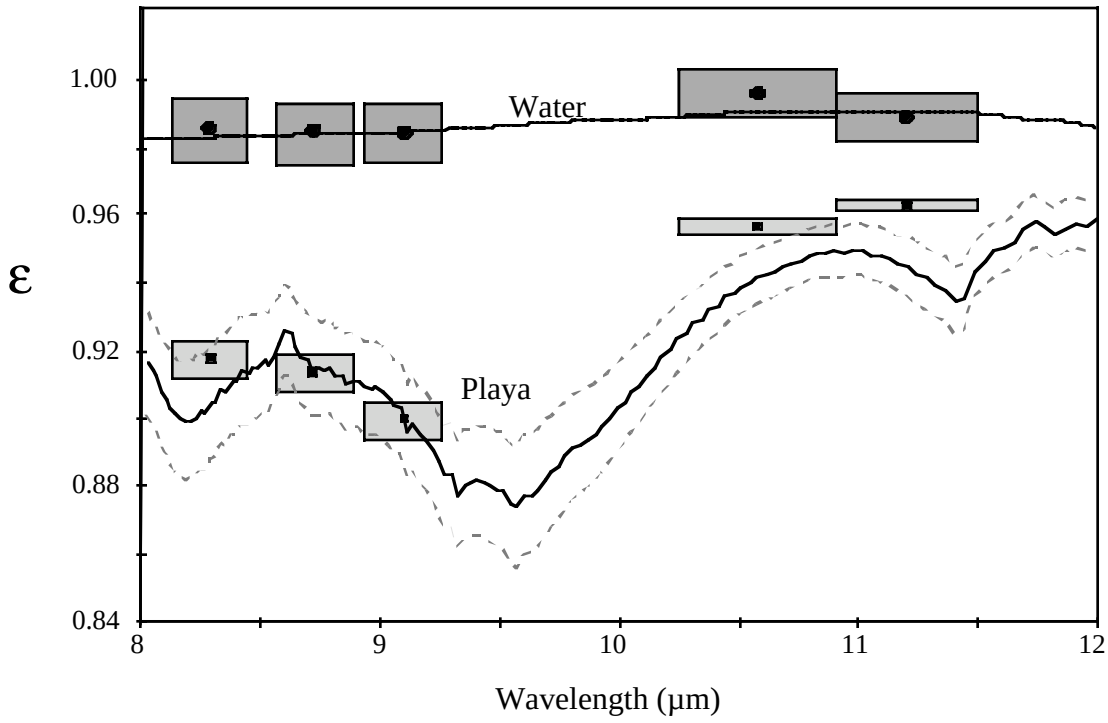

Figure 22. TES emissivities (bars) compared to field emissivity spectra, Railroad Valley playa. Upper line: water spectrum (J. W. Salisbury, pers. comm., 1995). Lower line: playa spectrum, Site B (ε_{max}=0.97). Dashed lines indicate 1-σ natural variability. Dark bars: TES ε values for ponds, Site E. Light bars: TES ε values for Site B. ASTER band centers are indicated by dots in the bars. Bar heights indicate 1-σ precisions; bar widths indicate band widths.

3.7.3 Discussion of TES Performance

Applying TES to numerically simulated TIR radiance data suggests that TES performs within its design specifications to recover temperatures and emissivities within 1.5 K and 0.015, with respective precisions of 0.4 K and 0.003. Analysis of simulated ASTER data acquired by TIMS, however, raises some questions. Although precisions are close to predicted limits, temperatures are less accurate than expected, and there are systematic and significant errors in recovered emissivity spectra. These problems were observed for all four TIMS images for which concurrent atmospheric measurements have been made. As seen for the spectrally flat water targets, the concentration of emissivity inaccuracies in ASTER bands 10 and 14, which are the most subject to atmospheric effects, suggests that the atmosphere correction may be imperfect. There may also be problems with TIMS calibration, field emissivity spectra, or laboratory reflectance measurements. We do not attribute the errors to TES itself, because they do not occur in numerical simulations.

TES is sensitive to errors in spectral contrast because emissivity amplitude and hence temperature depend on MMD. Therefore, incomplete removal of atmospheric effects in even a single channel will reduce accuracies of the recovered T and ε significantly. This problem may be irreducible, because scatter about the ε_{min}-MMD regression line appears to be a real property of natural surfaces. For high-MMD scenes this scatter is coincidentally equivalent to the ASTER NEΔT of 0.3 K, and to engineering predictions of ~1 K radiometric accuracy; however, measurement noise is random, whereas regression effects are organized spatially. The MMD effects are most serious for graybodies, such as vegetation and water. For these important scene types random measurement errors affecting MMD are amplified in the final T and ε products. Although the ε_{min}-MMD regression now appears to be robust, it does warrant further study before routine use of TES, and improvement of TES before launch of Terra will focus on refining the MMD relationship.

Improvements in ASTER sensitivity and noise levels would translate into improved TES precision over natural graybodies. However, even for NEΔT=0, TES could not match the accuracy of dedicated sea-surface temperature algorithms, because these presume that ε is known and TES does not. For geologic surfaces, the inherent variability on the ε_{min}-MMD plane, not the NEΔT, is the major source of uncertainty. No improvement in this area can be forecast now.

Atmospheric correction may be the effective limit on TES performance with ASTER data during the EOS mission. For most scenes, the critical parameters are atmospheric transmissivity and path radiance. Errors in correction for these parameters propagate directly into T and ε. For many scenes, sky irradiance reflected from the scene is of minor significance: for example, at Castaic Lake it accounted for only 0.2 K. For humid atmospheres or warm atmospheres over cold scenes, however, the correction for reflected sky irradiance may be larger, even the most important factor limiting TES performance.

Mixtures of scene materials fall near the regression line if the endmembers do also. Potential sources of error include admixture of blackbody cavity radiation from rough surfaces, since ideal blackbodies fall above the regression line. Theoretical studies with radiosity models suggest that these effects will be minor because multiple-scattering contributions rarely exceed ~20% of the total radiance from natural surfaces.

To be effective, TES probably requires at least four or five channels of TIR data. Numerical simulations show that uncertainties become larger as the number of bands is reduced. It is possible for TES to run, for example, on only four of the five bands acquired by ASTER with little degradation in performance, whereas for two bands the products are only half as precise. Running on four bands is advantageous if, for some reason, one band of data is noisy or is lost during transmission. TES is also readily applied to TIR data sets acquired by scanners other than ASTER. However, directional effects at high scan angles such as found in MODIS data (±45°) may create difficulties that have not been considered in writing TES.

TES requires further testing on calibrated, atmospherically corrected TIR data before routine use by the remote-sensing community. However, we conclude that TES is a useful and general algorithm for recovering land surface temperature and emissivities from multispectral TIR imaging systems. The fundamental limitations are the variability in the ε_{min}-MMD relationship for natural surfaces, and atmospheric characterization and correction. Future refinements of TES may be possible, but performance characteristics reported in this discussion are probably close to the ultimate limits achievable with its approach.

4. VALIDATION PLAN SUMMARY

The TEWG plans to validate the temperature and emissivity Standard Products by comparing values with simultaneous measurements made: 1) in the field by ground instruments; 2) airborne scanners such as TIMS (Palluconi and Meeks, 1985) and MASTER (Hook and Tan, 1999); 3) MODIS. The goal of quality control efforts will be to see that: 1) TES temperatures recovered for water and snow are accurate and precise within the performance guidelines established by the TEWG; and 2) TES emissivities over water and snow, and also over a limited range of geologic (rock) targets, are likewise within established limits of accuracy and precision. Validation efforts will occur in three phases: 1) pre-launch phase. The effort will be directed towards determining that TES is functioning properly and establishing the accuracy and precision of the T and ε Standard Products using simulated ASTER data; 2) post-launch Initial Checkout (ICO) phase and post-ICO phase. The effort is directed towards demonstrating that TES works on actual ASTER data within the specified performance

levels during the as soon as data become available, during the first six months of the Terra mission; and 3) long-term monitoring. Here the goal is to keep track of TES performance under a wide range of conditions at a single site. The complete Validation Plan is found in Appendix E.

There is no need to set up special TES sites for tests of water and snow, because these sites are needed primarily for atmospheric correction validation and will be established and managed by the Atmospheric Correction Working Group (ACWG). The TEWG will help take data at these sites, but under the guidance of the ACWG. Because the emissivities for water and snow are known in advance, the only information the TEWG needs from the water/snow sites is the surface temperature data set, plus the atmospherically corrected aircraft scanner data from the ACWG.

At the "geologic" sites the main problem is to measure representative scene emissivities and to assess spatial heterogeneity, in order to define appropriate 90-m scene elements that be imaged by ASTER. At each site, tens to hundreds of field emissivity spectra will be measured until the emissivity at the 90-m scale, estimated from the 10-cm-scale measurements, stabilizes. Once the emissivities are established, before launch, it is not necessary to measure them again. During ASTER or aircraft data takes it is sufficient to measure surface temperatures and atmospheric characteristics, as for the ACWG sites.

The strategy of the TES validation program will be to make extensive use of the sites of the Atmosphere Correction Working Group to maximize economy. At the "geology" sites atmosphere measurements will be done the same way, but fewer data will be collected at the more remote sites. Because only a handful of sites will be studied, the extendibility or generalization of the findings is open to doubt. Following discussions at the Validation Workshop at GSFC in May 1996, these will be addressed by airborne transects using TIMS or MASTER. These transects will cross strong climate/altitude/ecological zones. Although the entire transect cannot be documented heavily in the field, local atmospheric conditions measured at one or two sites can be extended using the MODTRAN model. Problem areas with TES can be identified by photo-interpretation of the Standard Products.

Validation sites.. The main US "water" site will be Lake Tahoe, California. A low-altitude site will be established at the Salton Sea. Castaic Lake, near JPL, may be a backup site. The choice of “water” sites depends on proximity to JPL and on the requirements of the Atmosphere Correction Working Group. The Japanese team will also establish a water site at Lake Kasumigaura, and another off the eastern coast of Honshu.

The main U.S. "geological" site will be the summit caldera of Mauna Loa, Hawai'i, at nearly 4000 m elevation. High-altitude sites minimize errors due to atmospheric correction. The Hawai'i site consists of more than 1 km^2 of flat, smooth and compositionally homogeneous basalt, erupted in 1984. The caldera rim is of older lava flows covered with a siliceous weathering rind that contrasts spectrally with the fresh basalt of the caldera floor. Railroad valley Playa, a calibration test site in central Nevada, will be a second “geological” validation site. Back-up, all-season sites near JPL will be established at lower altitude, at the Kelso Dunes and at Goldstone Playa in the Mojave Desert. The Japanese team will establish a similar site at Tottori Sand Dunes, in Japan. Dunes and smooth rocks have less shadowing (temperature differences) and multiple scattering compared to rougher surfaces. Playa sites may be prove to be unsatisfactory for TES because the emissivity can change, necessitating new field measurements for every validation experiment. Nevertheless, the initial results are encouraging and show the problem of heterogeneity characterization to be manageable.

Monitoring site.. At least one site “water” and one “geologic” site will be chosen to monitor TES' performance on ASTER data over the lifetime of Terra, under a wide range of atmospheric conditions. This enables the best possible estimates of Standard Product reliability and any changes in reliability. The site will be imaged as frequently as weather and scheduling allow. The Lake Tahoe or Lake Kasumigaura sites are the best “water” candidates; Mauna Loa, Goldstone Playa or Tottori Dunes are the best “geologic” candidates. Other sites, especially over forests, will be considered as time and resources allow. Precision of both the T and ε products, and the accuracy of ε but not T, can all be monitored without simultaneous field measurements. Emissivity of water is known *a priori*, and emissivity for rock sites such as Mauna Loa can be determined beforehand. Emissivities for playas may change if the playa surface is wetted and dried, but they vary within a limited range and can be re-measured as necessary.

Ground instruments... Skin temperatures are hard to measure directly but may be inferred from radiometric temperatures if emissivities are known. Surface temperatures may be extrapolated from temperature profiles if the site is in thermal equilibrium. Temperatures for lakes will be measured using 16 continuously recording buoys with thermistor sensors. Additional measurements will be made with Everest radiometers in temperature-stabilized boxes devised at JPL. Surface temperatures for melting snowfields are known (273.1 K). Temperature profiles for dunes will be measured using thermocouples placed at different depths. Near-surface temperatures for bedrock will be measured by thermocouples placed in shallow drill holes, sealed with a putty compound and allowed to equilibrate. These holes will be located carefully on maps and aerial photographs so they can be re-occupied as required.

Emissivities for dunes and bedrock will be measured using JPL's μFTIR field emissivity spectrometer, calibrated with dual blackbodies and a diffuse gold reflectance standard. The blackbody temperatures are measured using thermocouples.

Atmospheric transmissivity, path radiance, and sky irradiance, will be estimated during pre-launch aircraft overflights, using two Radiosonde balloon sensors and (possibly) a Reagen Sun Photometer, as for the Atmospheric Correction sites.

Emissivity variability on scales of 10^{-2}-10^{1} m will be measured using FSI (FLIR Systems Incorporated) video-rate hand-held TIR imaging system, specially modified at the University of Washington to acquire data sequentially through three different filters (8.2±0.3, 8.7±0.3 and 11.7±1.6 μm). These filters were chosen to approximate ASTER bands 10, 11 and 12.

Airborne scanners... Pre-launch aircraft overflights of the "geologic" Railroad Valley and Mauna Loa sites have been made using TIMS, operated under contract to NASA out of Las Vegas. MASTER data have been acquired over Death Valley and Railroad Valley and have been requested to be flown Mauna Loa before launch. The Japanese team will operate their own AAS (ASTER Airborne Simulator) scanner over Tottori Dunes, and have tested AAS over Railroad Valley and Cuprite (Nevada) in May, 1996.

MODIS comparisons... Over large enough areas to be resolved by MODIS (0.5-km TIR pixels) MODIS data are an excellent basis for comparison. MODIS has better capabilities to measure TIR radiance, better capabilities for measuring atmospheric parameters, and better capabilities for mapping cirrus clouds than ASTER. On the other hand, MODIS does not duplicate the ASTER TIR bands: MODIS-N band 29 will acquire data at 8.6 μm, equivalent to ASTER band 11, and MODIS band 31 at 11.0 μm is equivalent to ASTER band 14, but the other three ASTER bands are unmatched. Therefore, the TES algorithm will be adapted for computing MODIS temperatures and emissivities, and the appropriate results will be compared with the ASTER products.

MODIS will also produce split-window water temperatures. These results are anticipated to be more accurate and precise than the ASTER TES water temperatures, and therefor form a good standard for performance. Castaic Lake and especially Lake Tahoe are large enough for MODIS to sample unmixed pixels of water, and these existing study sites will be heavily utilized. Mauna Loa is also large and homogeneous enough to test bot MODIS and ASTER over rock targets. However, ASTER can be tested against MODIS anywhere MODIS can resolve homogeneous scene elements, and this opportunity provides an economical measure of performance after launch.

5. SCHEDULES

Schedule milestones fall into four categories, itemized below. Essentially, the TES code is already complete except for minor adjustments. The most significant activity remaining is in TES validation.

Validation activities will begin as soon as it is possible to acquire data following launch, currently scheduled for 28 July 1999. The ICO will consist mainly of engineering tests; however, data will begin to be acquired over key validation sites. For sites in the continental US or Japan, TIMS, AAS or MASTER data will be acquired simultaneously with ASTER overflights. However, MASTER is not scheduled to fly over Hawai'i until summer 2000. For TES, ASTER is scheduled to collect data over a few sites as frequently as possible during ICO and especially the post-ICO phase.

Unfortunately, the post-ICO phase now coincides with Northern Hemisphere winter, curtailing activities at some validation sites because of weather. Data processing for validation will continue at a lower level throughout the life of Terra.

It is planned to update TES "tuning" coefficients by the end of the post-ICO operation. Validation sites will be monitored on a less frequent basis throughout the life of the mission to collect statistics on performance under different weather conditions, and to update tuning coefficients if necessary..

6. COMPUTATIONAL CONSTRAINTS, LIMITATIONS, AND ASSUMPTIONS

At present there are no computational constraints on the TES algorithms, which should work with thermal infrared data acquired during the day or night. The cloud mask will function well only for daytime data. The value of the computationally costly refinements implemented in TES needs to be determined during pre-launch validation studies. The full computing cost is also a factor in their deployment, but has yet to be assessed.

7. ACKNOWLEDGMENTS

We thank our colleagues on ASTER's T/ε Working Group for helpful advice and suggestions, and especially John W. Salisbury for providing spectra. We also thank Elsa Abbott and Frank Palluconi for their tireless help. We are grateful to Zhengming Wan for thoughtful formal criticism. This research was a collaborative effort of the U.S. and Japanese EOS/ASTER instrument teams, sponsored by the NASA EOS Project and ERSDAC.

8. REFERENCES

Abrams, M. J., Abbott, E. A., and Kahle, A. B., Combined Use of Visible, Reflected Infrared and Thermal Infrared Images for Mapping Hawaiian Lava Flows. *J. Geophys. Res.* 96(B1), 475-484, 1991.

Abreu, L. W., Kneizys, F. X., Anderson, G. P., Chetwynd, J. H., Berk, A., Bernstein, L. S., and Robertson, D. C., MODTRAN. *Proc. 1991 Battlefield Atmospherics Conference,* El Paso TX, 1991.

Anderson, G. P., Chetwynd, J. H., Theriault, J.-M., Acharya, P., Berk, A., Robertson, D. C., Kneizys, F. X., Hoke, M. L., Abreu, L. W., and Shettle, E. P., MODTRAN2: Suitability for remote sensing. In the workshop on atmospheric correction of Landsat imagery, edited by P. N. Slater and L. D. Mendenhall, Geodynamics Corporation, Torrance CA, 1993.

Barducci, A., and Pippi, I., 1996. Temperature and emissivity retrieval from remotely sensed images using the "grey body emissivity" method, *Transactions on Geoscience and Remote Sensing*, IEEE Trans. Geoscience and Rem. Sensing 34(3), 681-695.

Barton, I. J., Transmission model and ground truth investigation of satellite derived sea surface temperatures. *J. Clim. Appl. Meterol.* 24, 508-516, 1985.

Becker, F., The impact of spectral emissivity on the measurement of land surface temperatures from a satellite. *Int. J. Remote Sens.* 8(10), 1509-1522, 1987.

Becker, F., and Li, Z. L., Temperature-Independent Spectral Indices in Thermal Infrared Bands. *Remote Sens. Environ.* 32, 17-33, 1990.

Brown, O. B., MODIS Infrared sea surface temperature algorithm. Algorithm Theoretical Basis Document, NASA Contract Number NAS5-31361, 10 November 1994.

Clough, S. A., F. X. Kneizys, L. S. Rothman, and W. O. Gallery, Atmospheric spectral transmittance and radiance: FASCOD1B. *SPIE,* **277,** 152–166. 1981.

Cothern, J. S., Gillespie, A. R., and Smith, M. O., Algorithm theoretical basis document for ASTER scene classification, Version 2.0. *in prep*, 1999.

Elvidge, C., Thermal Infrared Reflectance of Dry Plant Materials: 2.5-20.0 µm. *Remote Sens. Environ.* 26, 265-285, 1986.

Fujisada, H., and Ono, A., Anticipated performance of ASTER instrument in EM design phase. *SPIE Proc.*, pp. 187-197, 1993.

Dozier, J., and Warren, S. G., Effect of viewing angle on the thermal infrared brightness temperature of snow. *Water Resour. Res.* 18, 1424-1434, 1982.

Geller, G., Standard Data Products Specifications. JPL Document D-11719, Jet Propulsion Laboratory, Pasadena CA, August 1996.

Gillespie, A. R., Lithologic Mapping of Silicate Rocks Using TIMS. *The TIMS Data Users' Workshop*, June 18 - 19, 1985, JPL Publication 86-38, pp. 29-44, 1985.

Gillespie, A. R., Spectral mixture analysis of multispectral thermal infrared images. *Remote Sens. Environ.* 42, 137-145, 1992.

Gillespie, A. R., Kahle, A. B., and Walker, R. E., Color Enhancement of Highly Correlated Images. I. Decorrelation and *HSI* Contrast Stretches. *Remote Sens. Environ.* 20, 209-235, 1986.

Gillespie, A. R., Rokugawa, S., Hook, S. J., Matsunaga, T., and Kahle, A. B., Temperature/emissivity separation algorithm theoretical basis document, Version 2.0. Jet Propulsion Laboratory, Pasadena, 1 November 1995.

Gillespie, A. R., Rokugawa, S., Hook, S. J., Matsunaga, T., and Kahle, A. B., Temperature/emissivity separation algorithm theoretical basis document, Version 2.3. Jet Propulsion Laboratory, Pasadena, 16 August 1996.

Gillespie, A. R., Matsunaga, T., Rokugawa, S., and Hook, S. J., Temperature and Emissivity Separation from Advanced Spaceborne Thermal Emission and Reflection Radiometer (ASTER) Images. *IEEE Transactions on Geoscience and Remote Sensing*, 36, 1113-1126, 1998.

Gu, D., and Gillespie, A. R., Topographic normalization of TM images of forests based on sun-canopy-sensor geometry. *Remote Sens. Environ.*, 64, 166-175, 1998.

Hackwell, J.A., Warren, D.W., Bongiovi, R.P., Hansel, S.J., Hayhurst, T.L., Mabry, D.J., Sivjee, M.G., Skinner, J.W., 1996. LWIR/MWIR imaging hyperspectral sensor for airborne and ground-based remote sensing. SPIE Proc. 2819.

Hook, S. J., Gabell, A. R., Green, A. A., and Kealy, P. S., A Comparison of Techniques for Extracting Emissivity Information from Thermal Infrared Data for Geologic Studies. *Remote Sens. Environ.* 42, 123-135, 1992.

Hook, S. J., Kahle, A. B., Gillespie, A. R., and Jentoft-Nilsen, M., Algorithm theoretical basis document for temperature/emissivity separation, Version 1.0. 28 February, 1994.

Hook, S. J., and A. B. Kahle, The JPL Field Emissivity Spectrometer. *Proc. 5th Airborne Visible/Infrared Imaging Spectrometer (AVIRIS) Workshop, Vol. 2.*, JPL Publ. 90-54, Jet Propulsion Laboratory, Pasadena, CA., 17-18, 1995.

Hook, S. J., and Tan, H., http://masterweb.jpl.nasa.gov/, 1999.

Jaggi, S., Quattrochi, D., Baskin, R., An algorithm for the estimation of bounds on the emissivity and temperatures from thermal multispectral airborne remotely sensed data (Abstr.). *In* V. J. Realmuto, *Ed., Summary of the Third Annual JPL Airborne Geoscience Workshop, June 1-5*, pp 22-24, Jet Propulsion Laboratory Publication 92-14, 1992.

Kahle, A. B., Surface emittance, temperature, and thermal inertia derived from Thermal Infrared Multispectral Scanner (TIMS) data for Death Valley, California. *Geophysics* 52(7), 858-874, 1987.

Kahle, A. B., Gillespie, A. R., Abbott, E. A., Abrams, M. J., Walker, R. E., Hoover, G., and Lockwood, J. P., Relative Dating of Hawaiian Lava Flows Using Multispectral Thermal Infrared Images: A New Tool for Geologic Mapping of Young Volcanic Terranes. *J. Geophys. Res.* 93(B12), 15,239-15,251, 1988.

Kahle, A. B., Madura, D. P., and Soha, J. M., Middle Infrared Multispectral Aircraft Scanner Data analysis for Geological Applications. *Appl. Optics* 19, 2279-2290, 1980.

Kahle, A. B., Palluconi, F. D., Hook, S. J., Realmuto, V. J., and Bothwell, G., The Advanced Spaceborne Thermal Emission and Reflectance Radiometer (ASTER). *Int. J. Imaging Systems Tech.* 3, 144-156, 1991.

Kealy, P. S., and Gabell, A. R., Estimation of Emissivity and Temperature using Alpha Coefficients. *Proc. 2nd TIMS Workshop*, JPL Publication 90-55, 1990.

Kealy, P. S., and Hook, S. J., Separating Temperature and Emissivity in Thermal Infrared Multispectral Scanner Data: Implication for Recovering Land Surface Temperatures. *Geosci. Remote Sens.* 31(6), 1155-1164, 1993.

King, M. D., Kaufman, Y. J., Menzel, W. P., and Tanré, D., Remote sensing of cloud, aerosol, and water vapor properties from the Moderate Resolution Imaging Spectrometer (MODIS). *IEEE Trans. Geosci. and Rem. Sensing*, 30, 2-26, 1992.

King, M. D., W. P. Menzel, P. S. Grant, J. S. Myers, G. T. Arnold, S. E. Platnick, L. E. Gumley, S. C. Tsay, C. C. Moeller, M. Fitzgerald, K. S. Brown and F. G. Osterwisch, Airborne scanning spectrometer for remote sensing of cloud, aerosol, water vapor and surface properties. *J. Atmos. Oceanic Technol.* 13, 777-794, 1996.

Kniezys, F. X., Shettle, E. P., Abreu, L. W., Chetwynd, J. H., Anderson, G. P., Gallery, W. O., Selby, J. E. A., and Clough, S. A., User guide to LOWTRAN 7. Air Force Geophysics Laboratory Report No. AFGL-TR-88-0177, Hanscom AFB, Mass 0731, 1988.

Kniezys, F. X., Abreu, L. W., Anderson, G. P., Chetwynd, J. H., Shettle, E. P., Berk, A., Bernstein, L. S., Robertson, D. C., Acharya, P., Rothman, L. S., Selby, J. E. A., Gallery, W. O., and Clough, S. A., The MODTRAN 2/3 report and LOWTRAN 7 model. Edited by L. W. Abreu and G. P. Anderson, Phillips Lab., Geophys. Directorate, PL/GPOS, Hanscom AFB, MA 01731, Contract F19628-91-C-0132, 1 November 1996.

Li, W.-H., Weeks, R. J., and Gillespie, A. R., Multiple scattering in the remote sensing of natural surfaces. *International Journal of Remote Sensing*, 19(9), 1725-1740, 1998.

Lyon, R. J. P., Analysis of Rocks by Spectral Infrared Emission (8 to 25 microns). *Econ. Geol.* 60, 715-736, 1965.

Masuda, K., Takashima, T. and Takayama, Y., Emissivity of Pure and Sea Waters for the Model Sea Surface in the Infrared Window Region. *Remote Sens. Environ.* 24, 313-329, 1988.

Matsunaga, T., A Temperature-Emissivity Separation Method Using an Empirical Relationship between the Mean, the Maximum, and the Minimum of the Thermal Infrared Emissivity Spectrum. *Jour. Remote Sens. Soc. Japan* 14(2), 230-241, 1994 (in Japanese with English abstract).

McMillan, L. M., and Crosby, D. S., Theory and validation of the multiple window sea surface temperature technique. *J. Geophys. Res.* 89(C3), 655-3661, 1984.

Moore, B. III, Abel, P., Goward, S., Kasibhatia, P., Krider, P., Margolis, J., Tucker, J., and Wentz, F., Algorithm theoretical basis documents review. Panel two: ASTER, LIS, MOPITT, SEAWINDS. May, 1994.

Mustard, J.F., and Hays, J.E., Effects of hyperfine particles on reflectance spectra from 0.3 to 25 μm. *Icarus* 125, 145-163, 1998.

Palluconi, F. D., Hoover, G., Alley, R., and Jentoft-Nilsen, M., Atmospheric correction method for ASTER thermal radiometry over land, Jet Propulsion Laboratory, Pasadena, 1994.

Palluconi, F. D., and Meeks, G. R., Thermal Infrared Multispectral Scanner (TIMS): An Investigator's guide to TIMS data. JPL Publication 85-32, 1985.

Prabhakara, C., and Dalu, G., Remote Sensing of surface emissivity at 9 μm over the globe. *J. Geophys. Res.* 81(21), 3719-3724, 1976.

Prabhakara, C., Dalu, G., and Kunde, V. G., Estimation of Sea Surface Temperature from Remote Sensing in the 11- to 13-μm Window Region. *J. Geophys. Res.* 79(33), 5039-5044, 1974.

Price, J. C., Land surface temperature measurements from the split window channels of the NOAA 7 Advanced Very High Resolution Radiometer. *J. Geophys. Res.* 89, 7231-7237, 1984.

Realmuto, V. J., Separating the Effects of Temperature and Emissivity: Emissivity Spectrum Normalization. *Proc. 2nd TIMS Workshop*, JPL Publication 90-55, 1990.

Realmuto, V. J., Report of TIMS Airborne Calibration Experiment: Castaic Lake, California, 9 March 1994. Jet Propulsion Laboratory, 18 pp., 10 May 1994

Realmuto, V. J., Hon, K., Kahle, A. B., Abbott, E. A., and Pieri, D. C., Multispectral thermal infrared mapping of the 1 October 1988 Kupaiana flow field, Kilauea volcano, Hawaii. *Bull. Volcanology* 55, 33-44, 1992.

Sabins, F. F. Jr., *Remote Sensing Principles and Interpretation.* W. H. Freeman and Company, San Francisco, 426 pp., 1978.

Salisbury, J. W., Preliminary measurements of leaf spectral measurements in the 8-14 μm region. *Int. J. Remote Sens.* 7(12), 1879-1886, 1986.

Salisbury, J. W., and D'Aria, D., Emissivity of Terrestrial Materials in the 8-14 μm Atmospheric Window. *Remote Sens. Environ.* 42, 83-106, 1992.

Salisbury, J. W., Walter, L. S., and D'Aria, D., Thermal Infrared (2.5 to 13.5 μm) Spectra of Igneous Rocks. U. S. Geol. Surv. Open File Rept. 88-686, 1988.

Schmugge, T., Hook, S. J., and Kahle, A. B., TIMS observations of surface emissivity in Hapex-Sahel. *IEEE Trans. Quant. Rem. Sens. for Sci. Appl., Vol. III,* Firenze, Italy, pp. 2224-2226, 1995.

Siegal, R., and Howell, J. R., *Thermal Radiation Heat Transfer*. Hemisphere Publishing Corporation, New York, second edition, 1982.

Smith, M. O., Roberts, D.A., Hill, J., Mehl, W., Hosgood, B., Verdebout, J., Schmuck, G., Koechler, C., anmd Adams, J.B., A new approach to determining spectral abundances of mixtures in multispectral images. *Proc. IGARSS*, JPL, Calif., 1994.

Soha, J. M., and Schwartz, A. A., Multispectral Histogram Normalization Contrast Enhancement. *Proc. 5th Canadian Symp. Remote Sens.*, Victoria, British Columbia, Canada, pp. 86-93, 1978.

Vidal, A., Atmospheric and emissivity correction of land surface temperatures measured from satellite using ground measurements or satellite data. *Int. J. Remote Sens.* 12(12), 2449-2460, 1991.

Wald, A. E., Modeling thermal infrared (2-14 μm) reflectance spectra of frost and snow. *J. Geophys. Res.* 99, 24,241-24,250, 1994.

Wald, A. E., and Salisbury, J. W., Thermal infrared directional emissivity of powdered quartz. *J. Geophys. Res.* 100, 24,665-24,675, 1995.

Wan, Z., MODIS land-surface temperature algorithm theoretical basis document (LST ATBD). Version 1, Contract Nmbr. NAS5-31370, 37 pp., Feb. 1994.

Wan, Z., and Dozier, J., Land-Surface Temperature Measurement from Space: Physical Principles and Inverse Modeling. *Geosci. Remote Sens.* 27(3), 268-278, 1989.

Watson, K., Spectral ratio method for measuring emissivity. *Remote Sens. Environ.* 42, 113-116, 1992a.

Watson, K., Two-temperature method for measuring emissivity. *Remote Sens. Environ.* 42, 117-121, 1992b.

Watson, K., Kruse, F. A., and Hummer-Miller, S., Thermal infrared exploration in the Carlin trend, northern Nevada. *Geophysics* 55(1), 70-79, 1990.

Wen-Yao, L., Field, R. T., Gantt, R. G., and Klemas, V., Measurement of the Surface Emissivity of Turbid Water. *Remote Sens. Environ.* 21, 97-109, 1987.

Yamaguchi, Y., Tsu, H., and Fujisada, H., A scientific basis of ASTER instrument design. *SPIE Proc.*, pp. 150-160, 1993.

APPENDIX A: FORMAL REVIEWS OF THE ATBD AND RESPONSES

Version 1.0

In 1994, the Temperature/Emissivity Working Group (TEWG) designated two different algorithms to produce the ASTER temperature and emissivity standard products. These were the Normalized Emissivity Method and (NEM) and Alpha-Derived Emissivity (ADE) approach, reviewed in Appendix B. Two candidates were selected to provide time for complete evaluation. The TEWG's main concern with the NEM algorithm was that the key assumption, that there was a single maximum emissivity for most rocks, soils, water and vegetation, was not true at the level of accuracy the TEWG aimed for. The ADE algorithm solved that problem, but used Wien's approximation, which caused recovered emissivity spectra to tilt proportional to temperature. The TEWG recommended strengthening the empirical basis for the ADE method through a program of field spectral measurements.

The Version 1.0 ATBD (Hook *et al.*, 1994) was reviewed by a panel convened by NASA (Moore *et al.*, 1994). Most reviewers found the NEM and ADE algorithms attractive because of their relative simplicity and speed of operation. Reviewers commented that the basic TIR remote-sensing problem, indeterminacy, probably cannot be overcome completely by any algorithm. As one reviewer put it, "sometimes nature is not kind." The ADE method dealt with this problem by resorting to empiricism. Some reviewers felt that this was elegant, making use of our backlog of experience with terrestrial scenes; others were concerned that it was unsatisfying because, tautologically, the algorithm might fail when it encountered a scene not considered in defining the regression.

The TEWG has preserved the empirical approach to addressing the under-determined equations in the new TES algorithm. The new finding that field emissivity spectra yield the same regression as laboratory reflectance spectra of different samples bolsters this strategy; however, the applicability of the regression to all scenes remains a matter of concern and further research. Central to this effort is the collection and compilation of more field emissivity spectra. This important topic is addressed in the Validation Plan.

Some reviewers commented that the NEM and ADE algorithms had yet to be tested beyond numerical models, so there might be unexpected difficulties in extending them to airborne or space images. Undoubtedly difficulties will arise, but it is not true that these algorithms are untested on actual data -- considerable informal experience had been collected, and some studies published, when ATBD Version 1.0 was prepared. On the other hand, the new TES algorithm now supported has been tested only on four real images, as documented in the current ATBD (Version 2.3). A second major goal of the TEWG is to collect more calibrated airborne TIR images (TIMS and MAS) with ancillary atmospheric and ground data for further testing.

The suggestion was made that the ASTER and MODIS teams converge on a common algorithm, or set of algorithms. This idea is highly attractive in principle. Communication between the TEWG and the MODIS team has been facilitated by inclusion of MODIS team member Zhengming Wan in the TEWG. However, the goals and capabilities of ASTER and MODIS differ in some important ways. MODIS, with higher sensitivity, is designed to acquire moderate-resolution TIR data, including ocean images. ASTER acquires high-resolution data over the land surface. MODIS does not have sufficient bands within the 8-14 μm atmospheric window to execute the TES algorithm effectively. ASTER does not acquire the data on the edges of the atmospheric window that allow MODIS to characterize atmospheric absorption internally; therefore, ASTER would recover inaccurate split-window ocean-temperatures, for example. The MODIS algorithms are designed mainly to recover accurate and precise temperatures, especially over oceans and forests. ASTER goals require recovery of "seamless" temperature and emissivity data over the land surface, forest and desert alike. Consequently, MODIS and ASTER will have different algorithms.

The TEWG endorses efforts to bring ASTER and MODIS closer together. It is a good idea to develop specialized temperature-recovery algorithms for ASTER, independent of TES, to facilitate comparison of ASTER and MODIS data after launch. However, these cannot take the place of the standard products.

Reviewers' other comments can be grouped in six categories, treated separately below.

Presentation... The desire was expressed that the ATBD be comprehensive, yet readable -- especially in its treatment of error analysis. The sense of the comments was that there was too much statistical characterization of the algorithm performance, and perhaps not enough attention to identifying the factors responsible for the biggest error. In Version 2.3 we have tried to abbreviate the statistical treatment, and we have identified the factors that cause us the biggest headaches. However, the goal of readability and thorough treatment are probably mutually exclusive. The TES algorithm, simple at its core, is complex in its implementation. Each section contributes to the inaccuracy and imprecision of the whole, and requires analysis and discussion.

Atmospheric correction.. All reviewers agreed that atmospheric correction needed more attention. The major issue was the need for a plan to compensate for reflected downward sky irradiance. The problem is that the answer -- in this case the emissivities -- must be known before correction can be made, thus indicating some iterative approach. The TEWG has implemented such a modification in the new TES algorithm.

The suggestion was also made that the TEWG use products from other EOS instruments such as MISR or MODIS to characterize the atmosphere for correction. In fact, this is the TEWG's plan, except that the generation of the atmospheric parameters is to be done as standard ASTER products that provide "radiance leaving the ground" (i.e., corrected for atmospheric absorption and path radiance) and downwelling sky irradiance, corrected for elevation using DTMs. The major improvement over ATBD Version 1.0 is the incorporation of the elevation data into the estimate of sky irradiance.

Product artifacts... One reviewer pointed out that, because it makes use of Wien's approximation, the ADE algorithm produces tilted emissivity spectra. We have dropped support for this algorithm for this reason, since the effect is significant at projected measurement precisions for ASTER. Following Matsunaga (1994), we have adapted the empirical relationship at the core of the approach to the new TES algorithm, which produces unbiased spectra.

The suggestion was also made that we address artifacts introduced by instrument "noise." Since we had already considered the impact of random measurement errors at the projected NEΔT level (0.3 K in 1994, revised to 0.2 K in 1996), it is possible that the reviewer intended for us to investigate other scanner problems: transmission errors, microphonic interference, and so forth. We have not done this, although a QA plan does exist for flagging the standard product if such errors can be identified. Most such errors are fatal and/or obvious, and we do not yet have engineering projections of the severity of anticipated problems. We may address this problem as we learn more about system performance; for now, we have incorporated no noise-recognition algorithms in the TES algorithm.

Reviewers also expressed concern that we did not address directional effects, including shadowing and penetration into sparse vegetation canopies. Uncorrected, some directional artifacts can introduce errors of several K into the apparent temperatures. Also, we had no treatment of topographic effects and multiple scattering.

Although the issue of viewing geometry and topographic effects is complex and thorny, it is important to recognize that ASTER's small range of view angles ($\pm$2.5° for each TIR image), minimizes differential effects within a scene, and the maximum view angle (11°, if the scanner is slewed its maximum of 8.5°) is comparable to maximum view angles for TM images. Overall, directional effects will be much less significant than for MODIS, with its 55° maximum view angle. Nevertheless, we have addressed directional artifacts in ATBD Version 2.3, although no correction is made in the algorithm itself.

Classifier... Version 2.0 of the ASTER TES algorithm used VNIR/SWIR scene classification to flag cloudy areas and cloud perimeters for which ground temperatures and emissivities are likely to be in error. Version 2.3 instead uses a pre-executed classifier to identify clouds and cloud perimeters. Therefore, comments concerning version 2.0 pertain to the classifier ATBD (Cothern *et al.*, 1999), but no longer to the TES ATBD.

The original ATBD called for a more aggressive role of scene classification, as a research topic for possible use in improving algorithm performance. Two specific contributions were identified and discussed in TEWG meetings: 1) for the NEM approach, VNIR/SWIR classification could be used to identify scene types having distinctive maximum emissivities (ε_{max}). For example, forests and water bodies are readily identified in VNIR images, and have distinctly higher emissivities than rock surfaces (~0.99 *vs.* ~0.95); 2) In 1994, the TEWG suspected that the regression between the mean and variance parameters used by the ADE algorithm might be somewhat different for soils than for rocks; coefficients selected according to scene classification might improve overall accuracy.

Reviewers expressed contradictory opinions on the role of classification in refining the ASTER temperature and emissivity products. One thought that use of classification along the lines described above would be an important refinement; another felt that classification could be used in lieu of the TIR data to estimate emissivities! Others expressed concern that, because VNIR classification was unavailable for night-time acquisitions, it should not be used for day-time data, either.

Most reviewers agreed that the interaction between the ASTER T/E code and the classified product, AST10, needed more exploration. This concern has been effectively removed because EOS no longer supports AST10 as a standard product. The current ASTER strategy utilizes a modification of the AST10 algorithm only to identify and flag clouds (Cothern *et al.*, 1999), and this algorithm is executed before entering the TES code. Valid reviewer concerns about variable treatment for TIR data taken alone or in conjunction with VNIR/SWIR data (or data from other instruments), together with concerns for the AST10 algorithm accuracy (~90%, estimated visually), have confirmed our intention to use image classification only for QA, and not to improve the temperature and emissivity data products.

Validation Plan... Reviewers expressed the desire for more detailed validation plans, commenting that nevertheless validation could reasonably be expected by launch. Some were concerned that there should be an extensive post-launch validation plan. A validation plan, including a post-launch plan, and justification are presented in ATBD Version 2.3.

Schedule... Reviewers were dissatisfied with the absence of a schedule for code delivery, product generation, and validation efforts. A schedule is presented and justified in ATBD Version 2.3.

Version 2.3

In late 1996, Michael King at NASA convened a second review panel, again headed by Berrien Moore. Version 2.3 of the TES ATBD (Gillespie *et al.,* 1996) and the Validation Plan were criticized separately. Both received a grade of "A-," with an "A" meaning "outstanding."

TES algorithm... The TES standard products were regarded as important to meeting the objectives of the NASA Mission to Planet Earth (MTPE) program and the global change research agenda. The algorithm itself was regarded as having a sound theoretical and technical basis. Production of an operational product at launch appeared to be feasible.

On the other hand, reviewers concluded that the TES approach depended heavily on the quality of the atmospheric correction (in a separate ASTER product), in turn dependent on the quality of input atmospheric profiles. This criticism is correct, but the proper point of correction is in the ASTER Land-Leaving Radiance Standard Product, which is the input to TES. The ASTER instrument was designed to avoid the very spectral regions that give information on atmospheric conditions, further comments by reviewers that water band absorption in ASTER band 10 and continuum absorption in band 14 are "quite strong" notwithstanding. In Version 2.4, we have elaborated discussions of atmospheric absorption in the TIR ASTER bands 10-14.

One recommendation was made for more sensitivity and error analysis besides the estimations made in the ATBD for the favorite condition (NEΔT) and some worst-case situations (in Figures 18 and 19). Curiously, this information had earlier been removed in response to criticisms of Version 1 that there was an over-emphasis on statistical characterization of performance. We have not conducted further analyses on simulated data. TES has by now been adopted and implemented in different remote-sensing laboratories around the world, and experience with actual data will accumulate soon (e.g., Schmugge et al., 1995).

The suggestion was also made that we should consider subpixel mixing with components with different emissivities and temperatures in wide ranges of atmospheric and surface conditions. In Version 2.3 sub-pixel mixing was discussed for isothermal conditions (Appendix D). The reviewers have a good point in that atmospheric path radiance need not fall on the MMD regression line; therefore, in improperly compensated data, mixed pixels and unmixed pixels alike may yield erroneous results. This observation has been added to Appendix D. Furthermore, an article on TIR mixing is in preparation for the open literature.

Reviewers recommended performing TES at a reduced spatial resolution of 4 by 4 pixels (360x360 m) so that accuracy may be improved by reduced NEΔT. This suggestion was apparently also motivated by the desire for a more direct comparison to lower-resolution MODIS and AVHRR data. Averaging 16 pixels may reduce imprecision by a factor of four (to $\leq$0.08K), but this would not lead to increased accuracy, which is controlled to a substantial degree by the scatter along the MMD regression line, which is independent of ASTER measurement error. However, performance in important scene types which are nearly graybodies would be improved, because the MMD would not be dominated by image "noise." In balance, ASTER was placed on Terra partly to serve as a high-resolution "zoom lens" for MODIS, and it does not seem reasonable to discard this advantage for little gain. Therefore, no action has been taken on this suggestion. It should be noted that improvement in "near graybody" scenes will not be improved by averaging *after* running TES, and that it would be possible to run TES on smoothed data to produce a special product, currently unsupported.

Finally, the recommendation was made to have closer synergism with AST09 and to use reference pixels with known emissivities (such as water body and dense canopy) and the difference in temperatures retrieved for different bands for evaluation of the inaccuracy of the atmospheric correction due to uncertainties in the input atmospheric profiles. This is part of the Validation Plan already.

A "critical area" needing further research and development prior to generation of data products was identified: it was how to provide useful QA flags and error estimates in the QA data planes. Specifically, the reviewers voiced concern about how to evaluate the quality of the atmospheric profiles and the atmospheric correction, and how these affected TES products. This is a clear problem, and one that the ASTER Temperature/Emissivity Working Group has discussed, but it is more properly in the domain of the Land-Leaving Radiance Standard Product, for which atmospheric correction is actually attempted. The Validation Plan in Version 2.3 (and Version 2.4) does already contain provisions for measuring atmospheric conditions at the time of overflight at validation sites, and these data will provide a basis for evaluation of TES product inaccuracies. However, the primary source of these Product errors will be inaccuracy of the Land-Leaving radiance Product, and therefore that is the logical point of correction. The primary concern of TES is how radiance errors propagate into temperature and emissivity errors, and that is already largely understood.

Validation plan... The primary strength of the Validation Plan in ATBD Version 2.3 was identified as the strong component of field analysis ("ground truthing"), which combined modeling and measurement, and allowed straightforward comparisons to MODIS results. No significant weaknesses were identified, other than the inherent difficulty in field studies. The approach was regarded as adequate for establishing the scientific validity of the algorithm Products and for ensuring the credibility of the EOS measurements. Specifically noted was the fact that joint field campaigns with MODIS and other

groups have already been implemented and will be continued. A joint article on temperature/emissivity product validation has been proposed following the Initial CheckOut (ICO) phase of Terra.

Reviewers cited the need for aircraft overflights both before and after launch. The pre-launch requirement is clear and is part of the Validation Plan in Version 2.3. Post-launch overflights are useful to establish the linkage between pre-launch and post-launch assessments of TES' performance with the same data sets, but once this has been established practical economic considerations argue against heavy continued involvement of aircraft in Product validation. Indeed, test sites have been chosen for their compositional homogeneity and stability, so that ground measurements (including atmospheric characterizations) are adequate for post-ICO validation.

Reviewers noted that spatial and temporal variations in surface temperature over an otherwise homogeneous site are the major limitations for the accuracy of field measurement data. This is certainly true, and the Version 2.3 validation plan addresses this important issue in the following ways: 1) heavy reliance on sites over water, where compositional homogeneity is certain and temperature is the only variable. Here, temperature profiles and radiant skin temperature measurements are made continuously at several sites within the test area. Because the ASTER pixels are smaller than MODIS (or AVHRR) pixels, spatial variability is less and the measurement problem more tractable. The temporal variability is a significant concern, because the exact instant of ASTER measurement of the test area cannot be known. Therefore, this problem can only be treated statistically, by analysis of the correlated and uncorrelated components of variations of the skin temperatures measured at the redundant field stations.

APPENDIX B: ALGORITHMS REVIEWED BY THE TEMPERATURE / EMISSIVITY WORKING GROUP

The Temperature/Emissivity Working Group (TEWG) considered a wide range of algorithms designed to recover surface temperature (T), emissivity (ε), or both, with the goal of selecting a single algorithm that would recover both over all terrestrial surfaces. None of the algorithms inspected by the TEWG could recover accurate T and ε unless the data were atmospherically corrected independently. The algorithms evaluated in this appendix are:

1) Alpha-derived emissivity (ADE) method
2) Classification method
3) Day-night measurement
4) Emissivity bounds method
5) Graybody emissivity method
6) Mean-MMD method (MMD)
7) Model emissivity method
8) Normalized emissivity method (NEM)
9) Ratio algorithm
10) Split-window algorithm

1) Alpha-derived emissivity (ADE) method... The ADE algorithm, along with the NEM algorithm, was supported by ASTER to generate standard temperature and emissivity products (Hook *et al.*, 1994). This is no longer the case; instead, the most attractive features of the ADE approach have been incorporated in the new TES algorithm described in ATBD Version 2.0 or higher.

The ADE method (Kealy and Gabell, 1990; Hook *et al.*, 1992; Kealy and Hook, 1993) is based on the "alpha-residual" technique that preserves the shape of the ε spectrum, but not its amplitude, nor T. The "alpha residual" spectrum, described below, ranges about a mean of zero. The key innovation of the ADE approach is to utilize an empirical relationship between the average ε and a measure of the spectral contrast or complexity in order to restore the amplitude to the alpha-residual spectrum, thereby enabling recovery of T also.

The regression is based on the common-sense observation that, for a blackbody, the mean emissivity is unity and the spectral variance is zero. For the silicate minerals that comprise much of the geologic substrate of terrestrial scenes deviation from black-body emissivity occurs because of spectral features (reststrahlen bands) that are localized by wavelength, at least in terms of the broad TIR window spanned by ASTER (8-12 μm). For such spectra, the variance is greater than zero and, of course, the mean is less than unity. The deeper the reststrahlen bands, or the more complex the spectrum, the greater the variance and the smaller the mean. In use, the mean is predicted from the variance, which is calculated from the measured radiances.

The regression is established from laboratory reflectance spectra of different rocks, soils, and vegetation (Salisbury *et al.*, 1988; Salisbury and D'Aria, 1992). The emissivity is estimated by Kirchhoff's Law (ε=1-r). In order to be useful for a specific sensor system, the laboratory spectra must be integrated to produce pseudo-spectra from which simulated radiances R_i can be calculated:

$$\varepsilon_i = \frac{\int \psi_i(\lambda)\varepsilon(\lambda)d\lambda}{\int \psi_i(\lambda)d\lambda}; \quad R_i = \frac{\int \psi_i(\lambda)\varepsilon(\lambda)B(\lambda,T)d\lambda}{\int \psi_i(\lambda)d\lambda}; \quad T = 300\ K, \tag{B-1}$$

where ψ_i is the sensor response function for image channel i. For ASTER, the data are recast into pseudo-spectra for ASTER channels 10-14 (Table 1). The mean parameter is calculated from the set of ε_i; the variance parameter is calculated from R_i. T assumed for the Planck function B, 300 K, is the average temperature of the Earth's surface (Sabins, 1978). Below, the calculation of the alpha residuals and the mean and variance parameters are described.

The alpha residuals are calculated utilizing Wien's approximation of Planck's Law, which neglects the "-1" term in the denominator. This makes it possible to linearize the approximation with logarithms, thereby separating λ and T:

$$\frac{c_2}{T} = \lambda_i \ln(\varepsilon_i) - \lambda_i \ln(R_i) + \lambda_i \ln(c_1) - 5\lambda_i \ln(\lambda_i) - \lambda_i \ln(\pi). \tag{B-2}$$

Wien's approximation introduces errors in R_i (and also in ε_i) of up to 1% at 300K and 10-μm wavelength (Siegal and Howell, 1982). Thus, the alpha residuals are not an unbiased estimation of emissivity, but contain temperature-dependent curvature that can be resolved by ASTER.

The next step is to calculate the means for the parameters of the linearized equation, summing over n sensor channels:

$$\frac{c_2}{T} = \frac{1}{n}\sum_{j=1}^{n} \lambda_j \ln(\varepsilon_j) - \frac{5}{n}\sum_{j=1}^{n} \lambda_j \ln(\lambda_j) - \frac{1}{n}\sum_{j=1}^{n} \lambda_j \ln(R_j) + \left(\ln(c_1) - \ln(\pi)\right)\frac{1}{n}\sum_{j=1}^{n} \lambda_j. \tag{B-3}$$

For ASTER, summation is over TIR channels 10-14. The residual is calculated by subtracting the mean from the individual channel values. Collecting terms, a set of n equations is generated relating ε_i to R_i, independent of T:

$$\lambda_i \ln(\varepsilon_i) - \mu_\alpha = \lambda_i \ln(R_i) - \frac{1}{n}\sum_{j=1}^{n} \lambda_j \ln(R_j) + \kappa_i \qquad \text{(B-4a)}$$

$$\kappa_i = 5\lambda_i \ln(\lambda_i) - \sum_{j=1}^{n} \lambda_j \ln(\lambda_j) - \left(\ln(c_1) - \ln(\pi)\right)\left(\lambda_j - \bar{\lambda}\right) \qquad \text{(B-4b)}$$

$$\mu_\alpha = \frac{1}{n}\sum_{j=1}^{n} \lambda_j \ln(\varepsilon_j); \quad \bar{\lambda} = \frac{1}{n}\sum_{j=1}^{n} \lambda_j . \qquad \text{(B-4c)}$$

Note that κ_i contains only terms which do not include the measured radiances, R_i, and hence may be calculated from the constants. Although dependency on T has been eliminated, it has been replaced by the term μ_α, related to the mean emissivity in the list of unknown parameters, such that the total number of unknowns is unchanged and the equations are still under-determined. It is μ_α that must be estimated if the actual emissivities are to be found.

The components of the alpha residual spectrum are proportional only to the measured radiances. They are defined as $\alpha_i \equiv \lambda_i \ln(\varepsilon_i) - \mu_\alpha$ and are equivalent to the right-hand side of Equation B-4a. To recover ε_i, μ_α may be estimated using the regression with the variance parameter ν_α found for the laboratory spectra:

$$\nu_\alpha = \frac{1}{n-1}\sum_{j=1}^{n} \alpha_j^2 . \qquad \text{(B-5)}$$

The best-fitting curves relating μ_α and ν_α are of the form $\mu_\alpha = c\nu_\alpha^{1/x}$, where c and x are empirically determined coefficients (c=-0.085, ν_α=0.40 and r^2=0.935 for the 1994 86-sample TEWG spectral library). Once the emissivities are estimated, the temperature may be calculated using Planck's Law. For 95% of the spectral library, T is recovered within 1.6 K of the correct value at 300K. For simulated measurements of vegetation at 300 K, the precision of 0.2 K reflected only the ASTER NEΔT. The average recovered vegetation temperature was 1.4 K too high, because the spectrum plotted off of the regression line. Using a different collection of 81 library spectra, Hook *et al.* (1994) showed that 67% were accurate to within 1 K, compared to 58% for the normalized emissivity method. Performance differences reflect the choice of spectra in the library and are not fundamental.

The use of Wien's approximation results in a significant tilt to the recovered emissivity spectra. Furthermore, this tilt varies with temperature, from 0.022 at 340K to 0.005 at 240K, measured across ASTER bands 10-14. This progressive and artifactual tilt with increasing temperature is illustrated in Figure B-1. The impact on recovered temperatures is minimized because they are first calculated for each band, and then averaged. However, the biased character of the recovered spectra is fundamental to the approach.

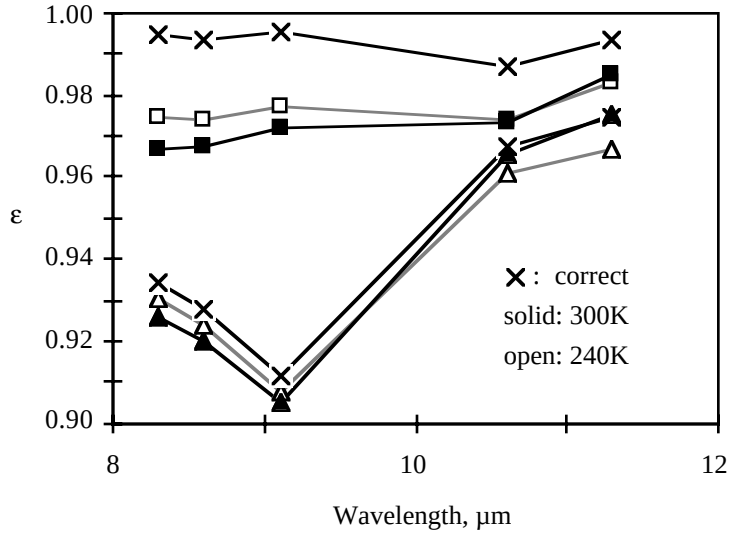

Figure B-1. Emissivity spectra recovered by the ADE technique at 240 and 300 K.

The TEWG originally adopted the alpha approach as one of two algorithms to be implemented provisionally. A detailed accounting of its performance is found in Hook *et al.* (1994) and has therefore been summarized only briefly here. The ADE was found to be more accurate than the model emissivity and NEM techniques, largely because it could handle both vegetation and rock surfaces. The TEWG incorporated the key feature of the ADE approach, the empirical regression between emissivity and spectral contrast, into the supported TES algorithm. The TEWG dropped support the ADE algorithm itself because:

1) the use of Wien's approximation introduces a bias in the residual spectra that is passed on to the estimated emissivity spectra;
2) it was relatively easy to correct this deficiency in the new hybrid TES algorithm;
3) the mathematical core of the ADE technique is more complex than other approaches.

2) Classification... The MODIS instrument team has proposed to use image classification and a spectral library to identify emissivity for the land surface (Wan, 1994). Once the emissivities are accurately known, it is a simple matter to calculate the temperatures -- essentially, this is the same problem addressed by the split-window method. Image classification is probably sufficient to discriminate areas of water, snow or closed-canopy vegetation for which, indeed, emissivities can be assigned reliably. The classification-based approach is capable of producing precise temperatures over areas that can be classified accurately, and that have well known emissivity spectra. Classification-based algorithms are less reliable for geologic substrates, which vary spatially, and which may have radically different emissivity spectra. In large part the failure of VNIR classification to predict substrate composition is because the emissivities are chiefly responsive to the Si-O bond, whereas the VNIR reflectances respond chiefly to OH^- and Fe oxides, which are not well correlated to silicate mineralogy.

Classified images are characterized by step discontinuities in "theme" or "class." These discontinuities are appropriate where, in fact, the land surface type or cover changes over a pixel or two -- ~100 m at the scale of ASTER TIR data. Examples of successful classification (from this viewpoint) include ocean/land boundaries. In other instances, cover changes are gradual, yet the classification change is triggered where some threshold criterion is exceeded, resulting in an inappropriately sharp boundary, possibly at an arbitrary location. Examples include gradual changes in vegetation cover.

The TEWG decided against implementing an algorithm based on VNIR classification because:

1) A fundamental goal was to recover emissivity spectra of geologic surfaces, and these could not be predicted accurately by classification.
2) For geologic substrates, recovered temperatures could be inaccurate by an unknown amount.
3) Temperature maps would have inappropriate step discontinuities, or would appear seamed or contoured, an unrealistic feature that the TEWG rejected for the ASTER standard products.

3) Day-night measurement... If well-registered multispectral day-night radiance measurements are available, it is possible to determine T and ε, since the number of measurements (2n) exceeds the number of unknowns (n+1) for n>1 (Watson, 1992a). The TEWG ruled out this esthetic approach for five reasons:

1) Standard T and ε images could not be produced unless ASTER acquired cloud-free images of a scene twice, severely reducing the number of scenes for which T and ε images could be produced.
2) ASTER cannot acquire images of the same scene only 12 hours apart, resulting in the possibility of change in the scene between the daytime and nighttime images and severe inaccuracies in T and ε;
3) Day-night image registration to ±1 pixel or better for 95% of the scene can not be guaranteed without special processing and therefore accurate registration is infeasible for a standard ASTER product;
4) The approach is exceptionally sensitive to measurement error (NEΔT). For example, for two image bands at 8 and 12 μm, day-night temperatures of 290 and 310 K, and for ASTER precisions, the temperatures could only be recovered with an uncertainty of 20 K or more.
5) Day/night emissivity differences can be expected for many areas because of dew.

4) Emissivity bounds method... Jaggi *et al.* (1992) and S. Jaggi, D. Quattrochi and R. Baskin (pers. comm., 1992) observed that the independence of T with wavelength permitted unambiguous bounds on T and ε values to be established. For every pixel and every band (considered in isolation) there exists a locus of (T,ε_i) vectors that are possible solutions (Fig. B-2). There is a family of loci, one for each band, for each pixel. Because T must be the same for all image bands, some (T,ε_i) pairs can be ruled out as candidate solutions. In effect, possible solutions all fall within a narrow range of T. Emissivity limits for each band are specified by the intersection of the locus of that band and the zone of possible T.

The ε limits are much closer if the range of possible ε (or T) can be restricted *a priori*. For the earth, it is commonly possible to assume that $0.8<\varepsilon<1.0$, for example, and the final ε limits are more useful than if the entire possible range $0<\varepsilon<1$ is permitted. If even a rudimentary classification is attempted, areas of vegetation, ocean, and so forth can be identified for which the range of possible ε is even more restricted -- $0.95<\varepsilon<1.0$, for example -- and the final limits are even more useful.

The elegant feature of the emissivity-bounds method is that, in principle, no assumptions need be made. In practice, however, the performance of the algorithm depends on how well emissivity limits are known *a priori*. The TEWG rejected the emissivity-bounds method because:

1) The restriction of the emissivity ranges to useful levels really requires closer *a priori* estimation than may be available in general.
2) Establishing useful *a priori* emissivity limits probably requires some sort of image classification, with its attendant introduction of artifacts in the standard products.
3) The technique does not identify most probable emissivities or temperatures, only possible ranges.

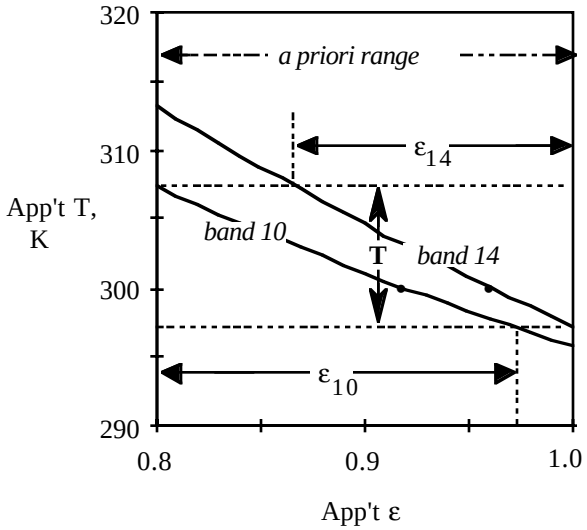

Figure B-2. Solution loci of apparent T and ε for ASTER bands 10 and 14 for a radiance vector calculated from the TEWG spectral library (300 K). If ε can be assigned *a priori* limits (here, 0.8<ε<1.0), the temperature range (arrow T) can be limited and more restrictive limits (ε_{10} and ε_{14}) can be assigned to ε. Heavy dots (•) on the (T,ε) loci indicate correct emissivities.

5) Graybody emissivity method... Instead of examining the same scene element at two different times and temperatures, as in the day-night method, it is sometimes possible to examine the scene element at different wavelengths λ_i and λ_j, chosen such that $\varepsilon_i=\varepsilon_j$. Provided this criterion is met, the situation is at least locally deterministic. It is necessary to find T and only a single ε for the two bands:

$$\left(\frac{\exp\left(c_2/\left(\lambda_j T\right)\right)-1}{\exp\left(c_2/\left(\lambda_i T\right)\right)-1}\right)=\frac{R_i}{Rj}\left(\frac{\lambda_i}{\lambda_j}\right)^5; \qquad \varepsilon=\frac{R_i}{B_i(T)}. \tag{B-6}$$

T is readily found by successive approximation. Thereafter, ε may be found for every channel. If more than two channels satisfy the requirements of the method, the best solution can be found by least-squares minimization of error.

The strength of the technique lies in its ability to recover emissivities for graybodies, regardless of the value of ε. This is not true for algorithms that assume emissivity values (e.g., ε_i, ε_{min} or ε_{max}). The main weakness is that the basic requirement, $\varepsilon_i=\varepsilon_j$, is not met for much of the land surface of the earth, at least for instruments such as ASTER with only a few TIR channels. Barducci and Pippi (1996) have proposed this technique for use on future scanners than have more TIR channels than are available on ASTER.

The graybody method is sensitive to measurement error, which is compounded by band ratioing. The technique is inherently unstable and sensitive to errors in the fundamental assumption. For simulated ASTER measurements of graybody radiances, made with Monte Carlo estimates of random errors at NEΔT=0.2 K (300 K), T precision is about 1.2 K.

The effect on recovered T of violating the fundamental assumption, $\varepsilon_i=\varepsilon_j$, can be estimated by analyzing radiance data calculated from the TEWG spectral library. For near-graybody spectra the accuracy for T is comparable to NEM (Fig. B-3); for most rock spectra the graybody assumption is violated and some T errors are in excess of 5 K (for quartzite, errors were as large as 17 K).

It would be possible to implement the graybody algorithm for ASTER data using another technique to identify appropriate pixels for which $\varepsilon_i=\varepsilon_j$. For these pixels, T accuracy is comparable to NEM. However, a different algorithm would have to be used for geologic materials. The TEWG rejected the graybody emissivity method because:

1) Even for near-graybodies, T recovery was not as precise as for NEM;
2) For non-graybodies the fundamental assumption that $\varepsilon_i=\varepsilon_j$ was often not met for ASTER.

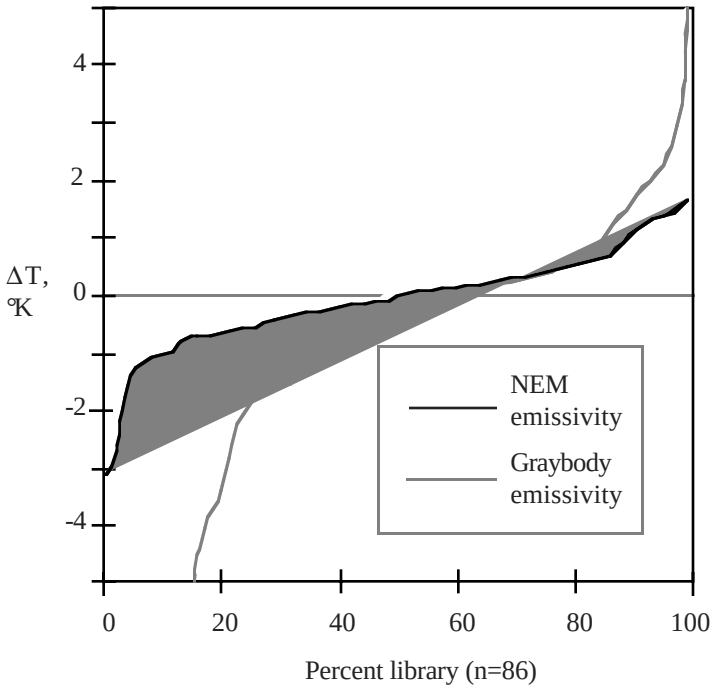

Figure B-3. Temperature error (ΔT) for the graybody emissivity and NEM algorithms, for samples from the TEWG spectral library. NEM performance is superior for most samples.

6) Mean - MMD Method (MMD)... The MMD algorithm (Matsunaga, 1994) is adapted from the ADE algorithm, but is simpler. Whereas ADE utilizes the empirical relationship between the mean emissivity ($\bar{\varepsilon}$) and the variance of alpha-residual emissivities, MMD utilizes the relationship between $\bar{\varepsilon}$ and the total range of the emissivities themselves, the maximum-minimum difference or MMD. Figure B-4 shows $\bar{\varepsilon}$ and MMD for various terrestrial materials (Salisbury *et al.*, 1988; Salisbury and D'Aria, 1992.). It is assumed that $\bar{\varepsilon}$ is a linear function of MMD. As seen in Figure B-4, this is probably valid, considering the scatter of the data about any regressed line; however, there is a suggestion in the data that the actual curve may flatten for MMD>0.2.

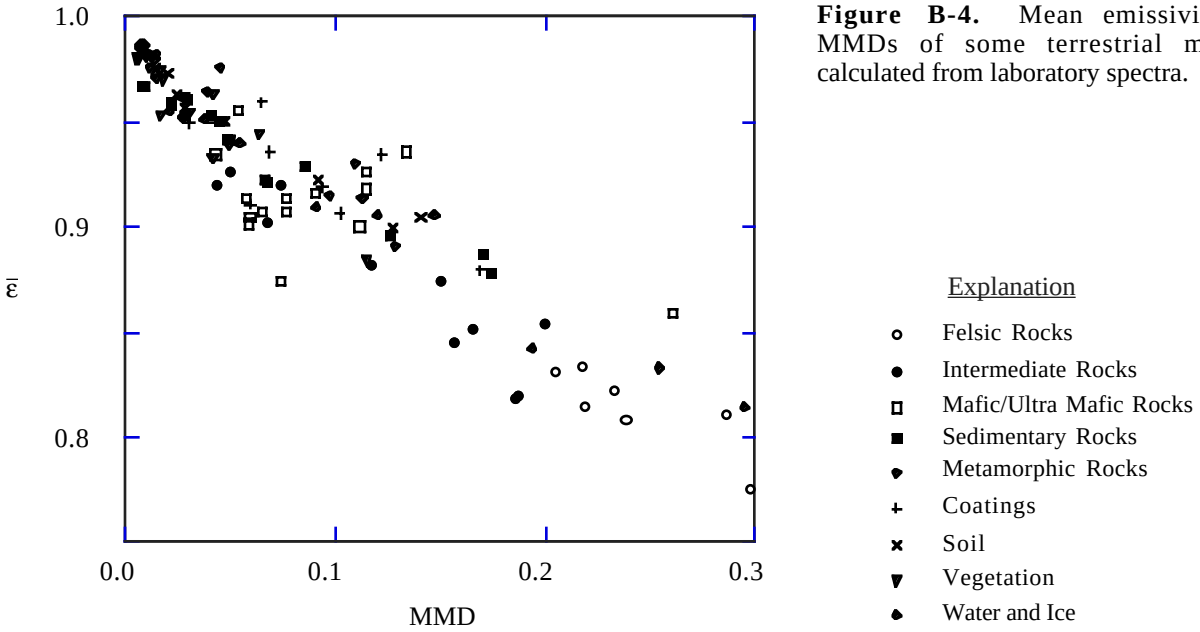

Figure B-4. Mean emissivities and MMDs of some terrestrial materials, calculated from laboratory spectra.

The Mean - MMD algorithm requires that the ε spectrum be estimated in order to calculate the MMD, from which $\bar{\varepsilon}$ is calculated. The apparent spectrum is then rescaled according to this average, and the process is iterated. After the final iteration, T is calculated. The algorithm is implemented in five steps:

1) The "first-guess" emissivities are calculated from surface radiance data using the NEM approach.
2) MMD is calculated from the "first-guess" emissivities or, on subsequent iterations, adjusted emissivities:
$$MMD_j = \varepsilon_{max,\,j} - \varepsilon_{min,\,j} \quad \text{(B-7)}$$
where $\varepsilon_{max,\,j}$ and $\varepsilon_{min,\,j}$ are respectively the maximum and the minimum ε values, and j indicates the current iteration.
3) The new mean emissivity, $\bar{\varepsilon}_{j+1}$, is calculated using the empirical equation:
$$\bar{\varepsilon}_{j+1} = a + b * MMD_j \quad \text{(B-8)}$$
where a and b are constants determined by regression analyses of laboratory spectra of various terrestrial materials. The constant a may be interpreted as the emissivity of commonly occurring graybodies such as water, snow and vegetation.
4) The emissivities are then adjusted so that their average is equal to $\bar{\varepsilon}_{j+1}$.
$$\varepsilon_{i,\,j+1} = \varepsilon_{i,\,j} * (\bar{\varepsilon}_{j+1} / \bar{\varepsilon}_j) \quad \text{(B-9)}$$
where i is the ASTER band number.
5) T is calculated from $\varepsilon_{i,\,j+1}$ and ground-leaving radiances for each ASTER TIR band.

Steps 2-5 are repeated until $Ts_{j+1} - Ts_j < NE\Delta T$.

The accuracies of the ADE and MMD algorithms are similar because they are based on the same empirical knowledge. T is relatively insensitive to multiple scattering of thermal radiation within a scene element and to downwelling sky irradiance. Calculated emissivities, however, are more sensitive to these factors. Scatter of $\bar{\varepsilon}$ about the regressed line ranges from about ±0.01 for graybodies to ±0.025 for some rocks. Isothermal mixtures of two materials which plot on the regression line also plot on the same line.

The accuracy of the MMD algorithm depends on the accuracy of the empirical relationship between the $\bar{\varepsilon}$ and MMD and on NEΔT. The MMD and NEM algorithms were compared using the two artificial test targets used in the Version 1.0 ATBD (Hook *et al.*, 1994). These results are summarized in Table B-1. Coefficients of two algorithms were optimized for each target:

"Fresh"	ε_{max}=0.950	a=0.983	b=-0.838
"Weathered"	ε_{max}=0.940	a=0.995	b=-1.031

Here, "fresh" and "weathered" refer to the two targets, one of which was calculated from laboratory spectra of broken, unweathered rocks, and the other of which was calculated from spectra of natural weathered surfaces and soils. Parameter ε_{max} is required for the NEM algorithm; a and b are the regression coefficients as described above. Although different coefficients for the two targets were used in this exercise, it should be noted that only a single set would be used in a real application. The set for the "weathered" target may be more appropriate to natural surfaces.

The rms errors for temperatures found using the MMD algorithm are smaller than those from the NEM algorithm unless NEΔT > 0.3 K, which is the baseline performance requirement of ASTER TIR. If NEΔT = 0.6 K, however, the difference between two algorithms is less than the measurement precision. In general, the MMD algorithm is more accurate but also more sensitive to measurement error than the NEM algorithm.

The TES algorithm is similar to the MMD algorithm in important respects. It differs in using a better estimate of the emissivity and in basing the "absolute" measure of emissivity on ε_{min} rather than $\bar{\varepsilon}$, a difference that results in less scatter of the data about the regressed line and, hence, improved performance. TES also uses a regression based on the simulated ASTER radiances rather than laboratory spectra. Lastly, TES incorporates other iterative refinements, including correction for down-welling sky irradiance, not addressed by the MMD algorithm.

Target	**NEΔT (K)**	**NEM rms error (K)**	**MMD rms error (K)**
Fresh	0.0	2.14	1.55
	0.3	2.44	2.02
	0.6	2.95	3.06
Weathered	0.0	2.48	1.19
	0.3	2.83	1.89
	0.6	3.53	3.38

Table B-1. Root-mean-square errors of the NEM and MMD algorithms for fresh and weathered artificial test targets.

7) Model emissivity method... The model emissivity method, or reference-channel method, assumes that the value of the emissivity for one of the image channels is constant and known *a priori*, reducing the number of unknowns to the number of measurements. We have called this algorithm the "model" emissivity method to indicate the strong role that the conceptual model -- that the emissivity spectrum peaks at a fixed wavelength and has fixed maximum value -- plays in estimating the "model" parameters, T' and ε'. However, other algorithms involve similar simplifying assumptions, and these also produced "model" parameters in our terminology.

Lyon (1965) suggested that, for most silicate rocks, the maximum emissivity (ε_{max}) was commonly ~0.95 and occurred at the long-wavelength end of the 8-14 µm TIR window. For ASTER, the "fixed" channel would be band 14 (10.95-11.65 µm). The model temperature T' is estimated using

$$T' = \frac{c_2}{\lambda_{14}}\left(\ln\left(\frac{c_1\varepsilon_{14}}{\pi R_{14}\lambda_{14}^5}\right)\right)^{-1}; \quad \varepsilon_{14} = 0.95. \qquad \text{(B-10)}$$

Blackbody radiances B_b can be calculated from Planck's Law and T' for the remainder of the bands, and the model emissivities can be calculated from R_b/B_b.

Although ε_{14} can be adjusted, no single value appears to be appropriate for all the surfaces encountered by ASTER. For example, for vegetation $\varepsilon_{14} \approx 0.983$; if the value is erroneously assumed to be 0.95, the emissivities will be underestimated, the spectrum will be warped, and T will be overestimated by 2.3 K. Vegetation, snow and water are all subject to this kind of error. Also, reststrahlen bands for some types of rocks - for example, peridotite - occur near 10 µm. For these rock types the errors may be even greater.

Only for 62 of 86 emissivity spectra (72%) does ε_{max} occur in band 14, and for 13 cases (15%) $|\varepsilon_{max} - \varepsilon_{14}|>0.01$. We estimate that the model emissivity method will recover T and ε inaccurate by >1 K and >0.01 perhaps a third of the time.

The TEWG considered using VNIR classification to select the best value for ε_{14} on a pixel-by-pixel basis. This approach has the disadvantage of complexity. Transitions from one class to another would be marked by discontinuities in the images of the calculated parameters. Furthermore, it is uncertain that the classification could be expected to distinguish rocks well enough to estimate ε_{14}.

The model emissivity approach is robust and has the virtue of simplicity. It produces moderately reliable results for a wide range of surface materials. Nevertheless, the TEWG rejected it because:

1) it is not capable of producing accurate results for both vegetation and rocks;
2) it will recover inaccurate T and ε for a significant fraction of geologic substrates;
3) the classification modification introduces undesirable image discontinuities or artifacts and may not be accurate for all surface materials.

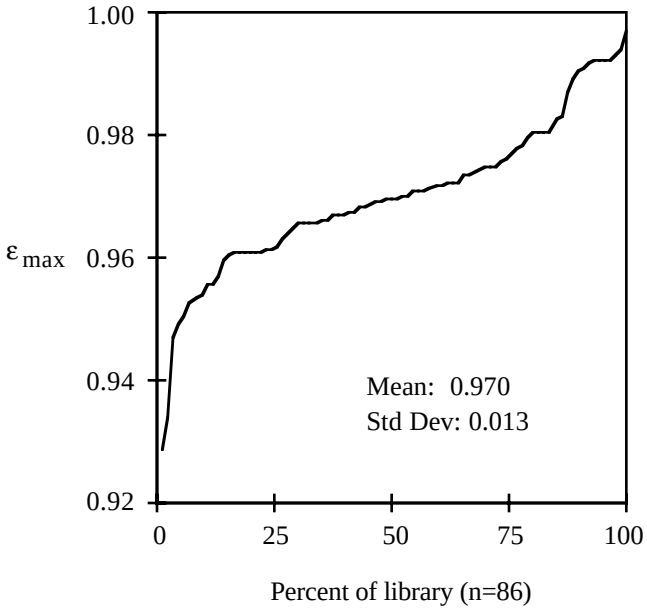

Figure B-5. NEM algorithm: distribution of ε_{max} for the spectral library. The highest accuracy overall will be obtained if the assumed value of ε_{max} is set to 0.97; the most accurate results for vegetation will be found if it is set higher (e.g., ε_{max}=0.99).

8) Normalized emissivity method (NEM)... A more sophisticated and flexible version of the model emissivity algorithm, the NEM algorithm permits the wavelength at which ε_{max} occurs to vary from pixel to pixel (Gillespie, 1985). The assumed value of ε_{max} is fixed, however, regardless of which image channel it is assigned to. Because the algorithm permits the wavelength of ε_{max} to vary, it is less error-prone than the simpler model emissivity method. Nevertheless, it fails to accommodate the difference in ε_{max} between vegetation and geologic materials. Adjustment of ε_{max} on the basis of image classification would produce the same artifacts identified in the discussion of the model emissivity method.

The NEM algorithm first must find the image channel in which ε_{max} occurs. Thereafter it proceeds as for the model emissivity method. Candidate temperatures T_i' are calculated for each channel from Planck's Law, ε_{max} and the wavelength at which ε_{max} occurs. The highest of these candidates is designated as the kinetic temperature for the pixel. Now the blackbody radiances can be calculated for each channel and used to find values for ε_i. A recent application of this technique to mapping basalt flows in Hawaii is given by Realmuto (1990).

For samples from the TEWG spectral library, ε_{max} =0.970±0.013 (Fig. B-5). This ε_{max} is higher than Lyon's (1965), probably because the library includes vegetation, water, soils and snow -- all of which have higher emissivities than most rocks. Figure B-5 points out the difficulty in assuming any single value for ε_{max}. In any particular sample, errors might be as high as 0.04, resulting in errors of T, ε, and in the shape of the emissivity spectrum.

For 81 spectra evaluated by Hook *et al.* (1994), 58% of the temperatures found by the NEM algorithm were accurate to within 1 K, compared to only 21% of temperatures recovered using the model emissivity method. For the 86 samples of the TEWG spectral library, evaluated at 300 K and NEΔT=0 K, the NEM algorithm returns temperatures with an average error or 0.0±0.9 K -- however, that was for the same data set used to select ε_{max}. The uncertainty, larger than the ASTER NEΔT, reflects the range in actual values of ε_{max}, independent of measurement error. This precision is acceptable for a standard temperature product for the land surface. However, for a graybody with ε=0.995 (spectrally similar to vegetation) evaluated at 300 K and NEΔT=0.2 K, temperature errors were 1.9±0.2 K. These results are less accurate than desired by the TEWG for vegetation. There appears to be no way of improving temperature accuracy for vegetation without sacrificing accuracy for geologic substrates.

Errors in recovered ε also occur when ε_{max} is inaccurate. Emissivities for vegetation are underestimated by ~0.031±0.006 (Fig. B-6), and the recovered spectrum has an apparent slope of ~0.01 over ASTER bands 10-14. This systematic spectral bias is a factor of 3 greater than the ASTER measurement error level (~0.003). For the spectral library, recovered emissivities were, on average, within 0.006 of their correct values. However, for some rock samples, recovered emissivities were as much as 0.05 too high.

The performance of the NEM algorithm is sensitive mainly to the assumed value for ε_{max}. The accuracy and precision of recovered values vary only insignificantly with temperature, for example. NEM shares the virtues of simplicity and overall reliability with the model emissivity algorithm. The TEWG originally selected the NEM algorithm as one of two supported algorithms (Hook *et al.*, 1994). It was subsequently "deselected" because:

1) The assumption of a single ε_{max} is demonstrably wrong, and results in temperature errors of as much as 2 K;
2) Emissivities may be in error by 0.03 or more. Accurate values are not recovered for both rock and vegetation;
3) Apparent emissivity spectra are tilted unless ε_{max} is coincidentally correct;

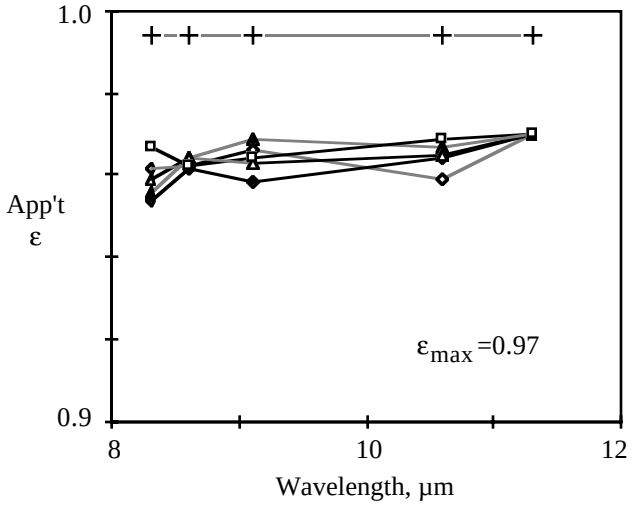

Figure B-6. NEM recovers tilted ε spectra for vegetation with an overall inaccuracy of ~0.03. The actual graybody spectrum is shown at top ("+"). Five recovered spectra are shown below (solid and open geometric symbols).

9) Ratio algorithm... Watson *et al.* (1990) and Watson (1992b) observed that ratios of bands i and j provided a normalized emissivity spectrum that had the property of preserving spectral shape well, provided that the temperature could be estimated even roughly. On the other hand, the technique had no way of recovering the actual ε, nor T.

$$\frac{\varepsilon_j}{\varepsilon_i} = \frac{R_j}{R_i} \frac{\left(\exp\left(c_2 / \left(\lambda_i T\right)\right) - 1\right)}{\left(\exp\left(c_2 / \left(\lambda_j T\right)\right) - 1\right)} \qquad \text{(B-11)}$$

To calculate the ε ratios it is necessary first to approximate the temperature from the measured radiances, requiring that ε be estimated. Emissivity can be estimated easily within ±0.075, since the range for many surfaces is only 0.85-1.00. This leads to an uncertainty in temperature of ±5 K. Correction of the radiance ratios for T at this level of precision results in ε ratios with an average error of only ~0.007 -- that is, only a little more than the error due to measurement precision (0.006). Using the NEM algorithm, T can be estimated within 2 K. In this case, the recovered ratioed spectrum will be within measurement error of the actual values.

It should also be possible to ratio each band to a common denominator band, instead of ratioing adjacent channels as discussed by Watson (1992b). In this way it would be possible to construct a ratioed emissivity spectrum ρ that represents the shape of the actual emissivity spectrum. It would also be possible to scale the ratioed spectrum by the ratio of the denominator band to the average of all the ratios, without altering the basic properties of the ratioed spectrum or its noise characteristics significantly. Thus,

$$\beta_i = \frac{\varepsilon'_i}{\varepsilon'_j} \frac{\varepsilon'_j}{\mu'}; \qquad \mu' = \sum_{i=10}^{14} \varepsilon'_i, \qquad \text{(B-12)}$$

where i represents the ASTER band number, ε' is the apparent ε calculated by the NEM algorithm, and μ' is the average apparent emissivity. This is the "RATIO" algorithm used by TES.

Adjacent band ratios are stable with respect to the estimated temperature and have precisions of ~0.006, for blackbodies measured with ASTER's predicted noise levels. Because the uncertainty for μ' (~±0.002) is less than for ε'_i (~±0.004), the uncertainty for β_i (~±0.004) is less than for the adjacent band ratios. However, if the estimated temperature is inaccurate, the ratio spectrum is systematically warped. If the NEM algorithm is used to estimate T, warping can happen if the assumed value of ε_{max} is wrong (Fig. B-7). Although for extreme errors in ε_{max} the average slope is comparable to that due to noise between adjacent bands (~0.005), the effect is systematic from band to band and therefore detectable for the spectrum as a whole. Nevertheless, ratioed emissivities are much less sensitive than NEM emissivities to errors in ε_{max} (Fig. B-8).

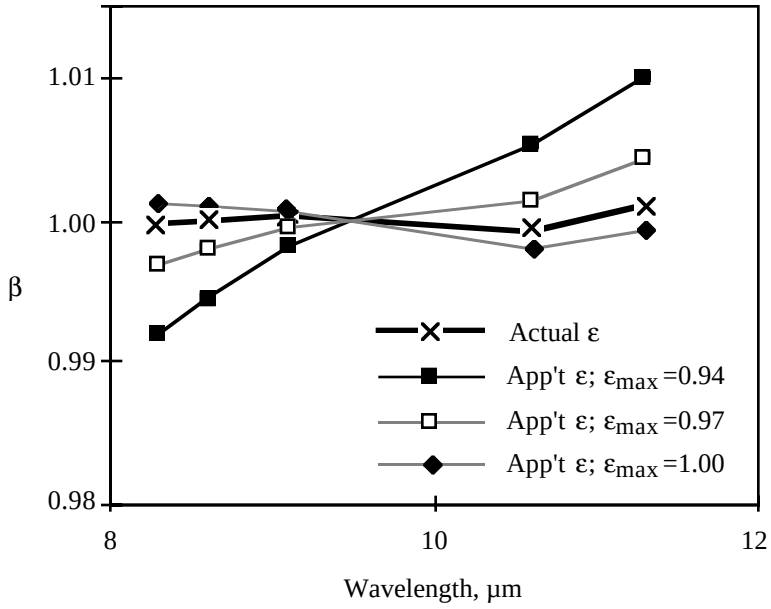

Figure B-7. Variation in normalized emissivities ratioed to their means, for different values of ε_{max}. The "actual" spectrum was calculated from simulated blackbody radiance (ε=1.00) "measured" in a Monte Carlo experiment with NEΔT=0.3 K at 300K. The apparent ("App't") ε data were calculated from the same simulated radiances using the ratio algorithm, assuming the indicated values of ε_{max}. Ratioed spectra are less sensitive to the assumed value of ε_{max}.than are normalized emissivity spectra (Fig. B-8).

Although the TEWG did not consider the ratio algorithm as a candidate for the supported temperature / emissivity algorithm, it did incorporate ratioed emissivities into TES. This was done because the shape of the emissivity spectrum was captured without a systematic bias, and because it was insensitive to the initial assumptions. The ratioing approach itself was rejected for the supported algorithm because:

1) The technique does not recover temperatures;
2) It does not recover actual emissivity values, either.

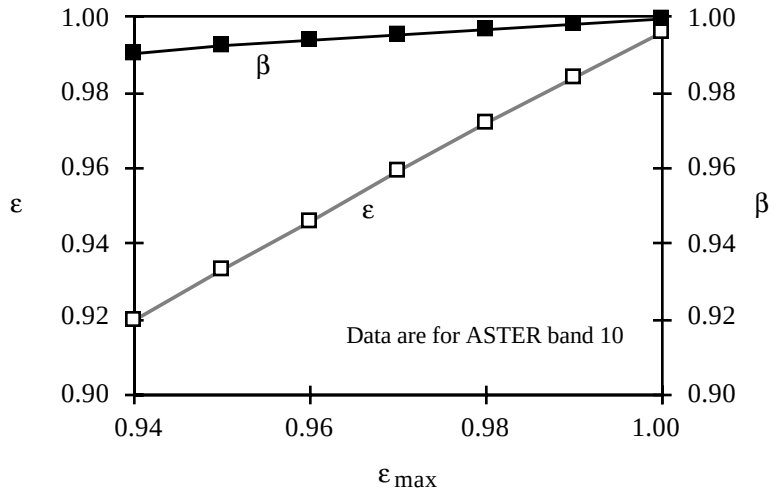

Figure B-8. Normalized emissivities (ε: open squares) are more sensitive to ε_{max} than are emissivity ratios (β: filled squares). Calculated for graybody radiance (ε=0.995).

10) Split-window algorithm... Split-window techniques are designed to recover temperatures for surfaces of known emissivity. The redundancy in the measurement is used to correct for atmospheric effects. The algorithms have been applied to the important task of measuring sea-surface temperatures. The TIR bands in the split-window approach are centered in spectral regions of different atmospheric transparency, controlled by water vapor. Since the kinetic temperature is independent of wavelength, discrepancies in the brightness temperatures in the two bands ($\Delta T=T_1-T_2$) are attributable to the atmospheric effects. Correction of the temperature error and ΔT, a relationship that is established by sea-surface temperatures measured *in situ* and radiance measurements, for a range of atmospheric conditions.

ASTER is designed mainly for inspection of the land surface but, of course, some images of oceans near land and some images of lakes will be acquired for which split-window algorithms might be useful. ASTER acquires five bands of TIR data instead of the minimum of two needed for split-window approaches. On the other hand, the bands are all chosen to minimize atmospheric effects; thus the necessary capability to assess atmospheric conditions is compromised. One consequence is that the approach is likely to be sensitive to measurement error. Numerical simulations suggest that ASTER could recover SST only within ~1 K with a two-channel algorithm. This performance is not markedly better than the more general algorithms can deliver and is an order of magnitude worse than high-precision imaging systems such as AVHRR or MODIS can deliver. The MODIS instrument team is planning on using a split-window algorithm to estimate sea-surface temperatures (Brown, 1994), and for the purposes of comparison between scanners on Terra a similar algorithm for ASTER is attractive. However, projected use of ASTER is over the land surface, and a sea-surface algorithm *per se* would have limited use. The TEWG recommended that the split-window might be useful for a special ASTER product, but not as the basis for the general TES algorithm. The reasons were:

1) The approach cannot recover emissivity and is hence inappropriate for use over land;
2) Temperature recovery requires knowledge of the emissivity, which is generally not possible over land;
3) The bands are not at the necessary wavelengths; at least one should be in an atmospheric water band.
4) The improvement in performance over water compared to more general land-surface algorithms is marginal.

APPENDIX C: TIR REMOTE SENSING OF HETEROGENEOUS TARGETS

In most remote-sensing studies involving TIR measurements only homogeneous isothermal surfaces have been considered. This situation must be considered a special case of the general problem, because real terrestrial surfaces are commonly heterogeneous and anisothermal at the spatial scale of measurement (e.g., 90 m for ASTER). The radiance leaving the ground may be mixed from components having different emissivity spectra and temperatures. Even for homogeneous isothermal surfaces, some of the emitted radiance may be reflected one or more times from the surface before its interception by the scanner, unless the surface is also smooth. With each reflection, the spectrum of the radiance is changed because $r_\lambda = 1 - \varepsilon_\lambda$. Thus the measured radiance is mixed from components having different emissivity spectra, each corresponding to the number of bounces or times the packet of radiation was reflected.

Supposing that there does exist some scale at which the surface is actually homogeneous and isothermal, and ignoring atmospheric and adjacency effects, the expression for the emittance from the pixel-sized surface element is given by:

$$R_\lambda = \sum_{i=1}^{p} f_i \varepsilon_{i,\lambda} \sum_{j=1}^{m_i} g_j B_\lambda\left(T_j\right); \qquad \sum_{i=1}^{p} f_i = 1; \qquad \sum_{j=1}^{m_i} g_j = 1. \tag{C-1}$$

p = number of homogeneous scene elements
m_i = number of isothermal elements within each scene element, i
f_i = fraction of pixel having spectrum ε_i
g_j = fraction of component i having temperature T_j

In this general case there may be a large number of unknowns, although the number of measurements n is unchanged. Since even the isothermal, homogeneous case is under-determined, it is not feasible to solve the general problem. Algorithms to find T and ε_λ have disregarded this issue, calculating an effective temperature T_{eff} and emissivity spectrum ε_{eff}. T_{eff} represents a weighted average temperature that need not correspond to any kinetic temperature actually found in the scene element, but which does serve as a representative value. Likewise, the apparent emissivity spectrum ε_{eff} need not correspond to ε for any real material, but nevertheless is a useful approximation. It should be noted, however, that the inability to recover actual emissivities for complex scenes will limit the diagnostic ability of any TIR scanner.

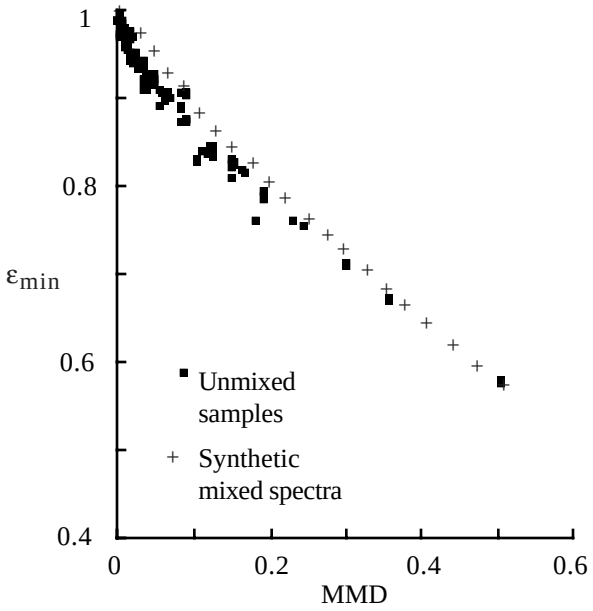

Figure C-1. Regression line for mixed spectra. Example was chosen to illustrate extreme behavior: mixture is between a rock spectrum falling on the regression line (lower right) and a blackbody (upper left), which plots above the regression line.

Even homogeneous but anisothermal scene elements consisting of ideal blackbodies will yield inaccurate apparent emissivities. Because the wavelength of the maximum radiance varies with T, the sum of Planck functions at different temperatures is not itself a Planck function. This problem is commonly encountered, for instance when the pixel spans both sunlit and shaded slopes. The inaccuracy in ε does not exceed the precision of 0.003 (due to NEΔT=0.2 K at 300 K) unless the temperature difference exceeds 20° K. Thus, shadowed slopes should not in general introduce appreciable errors. If the temperature difference is 40 K, however, as it might be on the edge of a snow bank, the inaccuracy in ε is ~0.02 -- nearly 15% of its expected range in the scene. It should be noted that the error is manifest as a tilted emissivity spectrum, not simply a global change in amplitude.

"Mixed" pixels are likely to be heterogeneous as well as anisothermal. The mismatch between the ε_{eff} and component ε spectra may be much greater, and more structured, than the simple tilt caused by anisothermal scenes. On the other hand, mixing commonly occurs between vegetation and some geologic substrate, or between cavity radiation and emittance from the smooth substrate, and both of these produce ε_{eff} spectra that resemble the substrate spectrum, but with lower contrast.

Mixing can also occur as a function of grain-size distribution within the pixel. Pulverizing rock or mineral samples can lead to dramatic changes in , even inversions of, emissivity spectral structure. However, the most common effect of fine, unpacked particles is probably to reduce spectral contrast (Mustard *et al.*, 1998).

There appears to little than can be done to improve TIR remote sensing of complex surfaces, because of the severely under-determined nature of the problem. Effects of mixing are much more likely in large pixels than small ones, because there is greater opportunity for different materials in the scene element. It is not clear at what scale the pixels loose their mixed character, but it is probably smaller than the 90-m resolution of ASTER. Comparison of ASTER and the lower-resolution MODIS TIR data should help clarify this issue.

From the perspective of the TES algorithm, mixing can cause poor performance if mixed pixels plot off the ε_{min}-MMD regression line. Although this will not happen if both endmembers themselves plot on the line, it will if one or both do not. This is shown in Fig. C-1 for a rough rock surface, for which cavity (blackbody) radiation and radiance from the smooth rock surface are mixed. The rock plots on the regression, but cavity radiation plots above it, and mixtures do also. Although admixture of cavity radiation is a common phenomenon, other equally common phenomena do not lead to deviant behavior: for example, mixing of vegetated and unvegetated surfaces need not, because vegetation plots near the regression line.

APPENDIX D: MULTIPLE SCATTERING AND ADJACENCY EFFECTS

Interaction between adjacent scene elements, or between clouds and the ground, can profoundly affect apparent T and ε. T is generally raised, especially at night, because radiative loss is retarded. A familiar example is the relative warmth of cloudy nights. Emissivities are also affected, largely because incident TIR radiance is reflected proportional to the complement of the emissivity (Kirchhoff's Law). Thus, multiple scattering tends to reduce spectral contrast or "flatten" recovered ε spectra.

The TEWG has considered several types of multiple scattering. Adjacency effects from clouds have been a special concern, because clouds are a common scene constituent. Simple radiative exchange models have been used to predict the zone around clouds for which apparent temperatures will be in error by a level defined as unacceptable, for example 1 K.

Multiple scattering on the land surface itself can be considered in four categories: scattering among resolved and unresolved scene elements, and exchange between spectrally similar and dissimilar materials. Additionally, volume scattering (e.g., in sparse vegetation canopies) must be considered.

Resolved topography... Topography at scales larger than some threshold (e.g., 100 m) can be described by DTMs, and for some or all ASTER scenes some form of DTM may be available. For scenes described by DTMs it is possible to calculate the effects of radiosity in the VNIR and in the TIR. Wen-Hao Li at the University of Washington has created a practical radiosity algorithm that calculates the contribution of multiple-scattered light to the total radiance from a scene, and has used it to estimate 1) the magnitude of the effect as a function of general scene roughness, and 2) the impact on apparent emissivities. An example is shown in Figure D-1. The multiple-scattered component is as large as 5% of the total emittance, for typical rough terrain. The effect is maximized at the bottom of steep valleys. The effect on apparent emissivity depends on the number of times the light is scattered before measurement, and on the actual emissivity. This is the familiar mixture problem: the multiple-scattering radiance appears to have been mixed with cavity (blackbody) radiation. Li's radiosity model quantifies this effect for any specified scene.

In principle, it is possible to estimate the effects of radiosity from resolved and modeled terrain, and to compensate for them. The TEWG considers this infeasible for ASTER standard products because: the radiosity algorithm has not been widely used and must be regarded as experimental; it is expensive to execute compared to the TES algorithm; its use presumes that ε is already known, thereby complicating standard use further.

Figure D-1. Total radiance (radiosity) emitted from an isothermal homogeneous scene (ε=0.9), consisting of directly emitted and multiple-scattered components. Left: Digital elevation model "illuminated" by sun at lower right, assuming a Lambertian surface of uniform reflectivity. Right: Multiple-scattered TIR component, contoured with black = 0-1%, gray = 1-3%, and white = 3-5% of the direct emitted component. Perspective view calculated from a 7.5' DTM having horizontal resolution of 30 m. Subscene is 3 km across.

Unresolved topography... Multiple-scattering effects also occur at sub-pixel scales for which radiosity models cannot be used, because DTMs are not available. We have experimented with Li's radiosity model on meter-scale "micro-DTMs" (cm resolution) and conclude that roughness effects are even more significant (~20%) than terrain effects (~5%). In the limit, emittance from gaps between cobbles from gravel bars, for example, approaches true blackbody radiation. In principle, it may be possible to characterize surface roughness by one or two parameters calculated remotely, and to use these parameters to predict TIR radiosity effects. This is the subject of active research, for example, in NASA's SIR-C program. However, the problem has not been solved, and in any case the treatment is experimental and not appropriate for standard products. The TEWG recommends that the temperature and emissivity standard products be regarded as "effective," that is, they will include the effects of multiple-scattered light from within the pixel.

Self-scattered emittance... Multiple scattering among homogeneous scene elements acts to mix cavity (blackbody) radiation with the direct emittance from a "colored" surface. Provided the ε spectrum plots close to the TES regression line (relating

ε_{min} to MMD), such admixture has the simple effect of moving the plotted position up and down the regression line, and the accuracy and precision of the recovered effective T and ε are unaffected. If one or the other of the endmembers plots away from the line, then mixtures will be have intermediate error characteristics.

Multiple scattering among heterogeneous scene elements... Despite the different physics involved, additive mixing of direct emittance from sub-pixel scene elements behaves similarly to admixing of cavity radiation due to rough surfaces, insofar as the TES algorithm is concerned. That is, provided both endmembers plot near the TES regression line, the accuracy and precision of the effective temperatures and emissivities are unaffected. However, as discussed in Appendix C, recovered T and ε are apparent or effective values only, and need not correspond to any particular T or ε present in the scene.

Numerical simulations show that multiple scattering between scene elements having different emissivities is similar to the self-scattered emittance problem. Provided the direct emitted radiance plots on the TES regression line, the multiple-scattered radiance will also. The TES algorithm will return precise effective T and ε, although their significance in terms of scene properties is uncertain.

It is worthwhile emphasizing that these problems affect all algorithms alike, and are not peculiar to the TES algorithm.

Volume scattering... Sparse vegetation canopies emit thermal radiance from different physical components -- leaves, branches, substrate, and so forth -- and from different positions. Much of the radiation leaving the canopy has been scattered many times, and bulk emittance is near-blackbody spectrally. The ratio of multiple-scattered to direct emittance varies with the depth into the canopy that the scanner can "see." This is a function of the canopy architecture, but also of the view angle of the scanner: an oblique glance at a canopy may show more first-surface radiance than a nadir view. Furthermore, bi-directional effects may appear as a function of view angle, because leaf orientation is not random.

The effect of volume scattering is likely to be more significant for T rather than ε. Because vegetation temperatures are a balance among radiative heating, evapo-transpirative cooling, and sensible heat transport by wind, T is likely to vary within the vegetation canopy. Emissivity, on the other hand, is nearly gray for leaves at the canopy top, and becomes more so for elements within the canopy because of multiple scattering. Even soil and rock exposed in canopy gaps have a subdued spectral signature. Therefore, apparent emissivities for canopies viewed at different angles are likely to be similar.

The TEWG has not considered correcting the standard T and ε products for volume-scattering effects. Assessing the magnitude of effects at the 90-m ASTER scale is a worthy goal for the pre-launch period.

APPENDIX E: TES VALIDATION PLAN

TABLE OF CONTENTS

1. INTRODUCTION

This validation plan applies to the surface temperature and emissivity products calculated from the thermal infrared image bands (10-14) of the Advanced Spaceborne Thermal Emission and Reflectance Radiometer (ASTER) on the Terra platform. The Temperature/Emissivity Separation (TES) algorithm that generates these products is described in detail in the Algorithm and Theoretical Basis Document, ATDB AST-08 and AST-05. A summary of the validation plans is also contained in that document. A single plan is presented for both standard products because they are closely interrelated and must be calculated with a single algorithm.

The TES algorithm is an elaboration of the earlier Alpha residual and MMD algorithms, documented in the ATDB. The key problem in calculating surface temperatures and emissivities is that there are more unknowns than measurements. Even in the simplest situation, there is an unknown emissivity for each image channel, plus a single kinetic temperature. In addition, atmospheric absorptions and emissions contribute additional unknowns. For ocean imaging the emissivity spectrum is well known, and it is sufficient merely to calculate the temperature, provided the atmospheric characteristics have been determined. The TES algorithm is applied to the ASTER standard product AST-09, "Level 2 Radiance--TIR, Land_Leaving." This product has been compensated for atmospheric effects. The challenge for ASTER, designed to look at

the land surface for which the emissivities are not known, is to estimate somehow one unknown from independent information. To do this, the Alpha and MMD algorithms use an empirical relationship between contrast and amplitude in the emissivity spectrum: the standard deviation or the min-max difference decreases quasi-linearly as the minimum emissivity increases. TES approximates the measure of spectral contrast by band-ratioing, which removes the effects of temperature, but also emissivity amplitude. Predicting the minimum emissivity from the spectral contrast restores the amplitude information and balances the unknowns and measurements.

1.1 Measurement and science objectives

The objective of the TES algorithm is to calculate the surface temperature and emissivity spectrum. The surface temperature influences heat transport across the surface/air interface and is important in radiation-budget research, and the emissivity spectrum is useful in studies of vegetation (because it helps distinguish substrate from canopy) and change (for example, soil erosion). Changes in surface temperature track phenological changes in vegetation communities and indicate unusual stress in crops, grasslands and forests.

1.2 Missions

ASTER is scheduled to fly on the Terra platform with a launch in July, 1999. ASTER will not fly on any of the subsequent AM or PM platforms. The design life of the instruments in orbit is five years but the design is such that, with attention to life-limiting elements, ASTER should be able to produce data for the entire six-year life of the Terra platform.

1.3 Science data products

The level-2 science data products to be validated are the surface kinetic temperature (AST-08) and the surface emissivities (AST-05). AST-08 contains of a single image plane consisting of short-integer (16-bit) pixels that specify the temperature in 0.1 K quanta. The ASTER NEΔT $\approx$ 0.3 K at 300K. AST-05 contains five image planes consisting of 16-bit pixels specify the emissivity ε in 0.001 quanta. The possible emissivity range of 0-1 is thus encoded as 0 - 1000. ASTER is capable of measuring ε within about $\pm$0.004 (at λ=10 μm and 300K). Current engineering projections of NEΔT=0.2 K correspond to $\pm$0.003 emissivity. Each standard product may have associated with it a 16-bit image plane containing pixel-by-pixel precision and other Quality Control data.

2. VALIDATION CRITERIA

The validation criterion is the quantitative agreement of the Standard Products calculated by TES with values for the same parameters measured independently for test areas in the field and by other scanners such as MODIS.

2.1 Overall approach

Performance characteristics for TES vary with spectral contrast. Although the Earth's surface is complex, for the purposes of TES validation it is necessary to consider only two types of scenes: near-graybodies for which the emissivities are known and homogeneous, and temperatures are known or homogeneous and can be readily measured during overflight; and "colored" surfaces for which emissivity spectra depart from graybody values but which are homogeneous. The first instance corresponds to the important class of scenes covering bodies of water, ice sheets and snow fields, and closed-canopy vegetation. For these scenes, the primary goal is to recover surface temperature since the emissivities are closely known in advance. The second instance corresponds to the class of scenes for which soil and rock are exposed. Surface temperatures cannot be recovered unless emissivities are recovered also, since they are unknowable in advance. This type of scene is common in the arid third of the land surface.

The temperature and emissivity Standard Products will be validated by comparing TES values with simultaneous measurements made: 1) in the field by ground instruments; 2) airborne scanners such as TIMS and MASTER; 3) MODIS. The goal of quality control efforts will be to see that: 1) TES temperatures recovered for water and snow are accurate and precise within the performance guidelines established by the ASTER Temperature/Emissivity Working Group (TEWG); and 2) TES emissivities over water and snow, and also over a limited range of geologic (rock) targets, are likewise within established limits of accuracy and precision.

There is no need to set up special TES sites for tests of water and snow, because these sites are needed primarily for atmospheric correction validation and will be established and managed by the Atmospheric Correction Working Group (ACWG) and, in some cases, by other groups also. The TEWG will help take data at these sites, but under the guidance of the ACWG. Because the emissivities for water and snow are known in advance, the only information the TEWG needs from

the water/snow sites is the surface temperature data set, plus the atmospherically corrected aircraft scanner data from the ACWG.

At the "geologic" sites the main problem is measure representative scene emissivities and to assess spatial heterogeneity, in order to define appropriate 90-m scene elements that be imaged by ASTER. Several hundred spectra will be measured until the emissivity at the 90-m scale, estimated from the 10-cm-scale field measurements, is stable. Once these are established, before launch, it is not necessary to measure them again. During ASTER or aircraft data takes it is sufficient to measure surface temperatures and atmospheric characteristics, as for the ACWG sites.

The TES algorithm will be validated before launch using ASTER data simulated from airborne scanner images. Field emissivities measured then will be used immediately after launch to re-validate the products using actual ASTER data. Periodically thereafter the validation experiments will be repeated to guard against instrument drift. During the Terra mission, validation will include cross-checking with MODIS data, aircraft underflights, and other image data as appropriate. We anticipate that one post-launch experiment will be monitoring TES ASTER products at a single site, perhaps Lake Tahoe, as frequently as possible, without field control. This experiment will be used to track precison of TES T and precision and accuracy of TES ε data (accuracy estimation is possible for ε because it is known for water in advance).

2.2 Sampling requirements and trade-offs

There are two key issues: first, the ideal test site scene must be compositionally homogeneous and isothermal during overflight; and second, the site must be large enough to encompass several ASTER pixels to permit reliable estimates of accuracy and precision. ASTER TIR pixels are 90 m on a side, whereas current field spectral measurements are 10-cm on a side. Both temperatures and emissivities are controlled at all scales down to the mm level, by mineralogical variability and vegetation cover and by surface roughness and texture. Proper random sampling is a practical impossibility. It is therefore important to choose sites carefully such that temperatures change little around the time of overflight, and to minimize the need for a dense sampling grid.

We plan to use sites for which compositional homogeneity can be established without intensive field spectral measurements. For the graybody sites, we will use lakes and snowfields; for the "colored" sites we will use smooth unvegetated bedrock surfaces or sand dunes.

The advantage of melting snowfields is that the temperature is everywhere 0°C, and deviations from known emissivity spectra are small and can be easily measured in the field. On the other hand, accessible snowfields are not available at all seasons.

Lake sites, like snowfields, have known emissivities, but temperatures must be measured by a network of buoys. Lakes are not isothermal at the level of ASTER sensitivity. Accessible lake sites are available at all seasons.

Appropriate "rock" sites are not common. Sand dunes are time-variable and may be moist, changing surface emissivities unpredictably. On the other hand, vegetation is minimal, and the scale of compositional heterogeneity is related to the dune structure (~10 m) so it is relatively easy to assess with field spectra having only 10-cm footprints. Sand dunes are accessible to JPL year-round.

Unvegetated bedrock sites tend to be at high elevation and are inaccessible during the winter. Most low-elevation sites the we know of are pediments (e.g., Cima Dome) and are vegetated. The best sites near JPL are mineralogically homogeneous granitic plutons, smoothed and swept clear of weathering products during the last ice age. Therefore, emissivity spectra can be determined in a reasonable field campaign. Several sites large enough for a grid of 90-m ASTER pixels are known.

2.3 Measures of success

The experimental goal is to recover temperatures and emissivities accurately and precisely for the validation sites using both field measurements, ASTER data, and other airborne or spaceborne TIR image data. In order to validate the TES products, the mean recovered ASTER products and the mean field determinations or independent measurements must agree within the specifications given in the ATBD: essentially 1-2 K and 0.01-0.02 emissivity units. Such agreement is a test of product accuracy. Additionally, variability of the standard products at the 90-m ASTER scale, assessed over the grid of "pixels" at the validation sites, must conform to variability predicted by the ATBD from the ASTER NEΔT. Such agreement is a measure of product precision and has similar size to the accuracy requirements.

3. PRE-LAUNCH ALGORITHM TEST/DEVELOPMENT ACTIVITIES

Pre-launch activities are focused on establishing validation sites, assessing site emissivity characteristics, collecting and interpreting simulated ASTER TIR data, and iteratively refining or tuning the TES algorithm to minimize cost and optimize performance. Activities will include field study, aircraft overflights, ASTER image simulation and calculation of the standard TES products. Work will be conducted collaboratively, especially with the Atmospheric Correction Working Group because the sites and data requirements are strongly overlapping.

3.1 Field experiments and activities

Validation sites (§7) will be established in the United States and Japan at:

- Lake Tahoe, CA
- Kasumigaura Lake (Japan)
- Salton Sea, CA
- Mt. Humphreys, CA
- Tottori Dunes (Japan)
- Mauna Loa, HA
- Railroad Valley, NV
- Kelso Dunes, CA

TES validation will be conducted in parallel with other validation tests for reasons of economy. In particular it is planned to work with the Atmospheric Correction sites and data. The two main sites of interest are Lake Tahoe and the Salton Sea. Both are near JPL and accessible year-round. Lake Tahoe is a high-altitude site that includes snowfields part of the year. The Salton Sea is below sea level and atmospheric corrections are bigger than for Lake Tahoe. TES validation at these sites requires only making use of the data collected by the Atmospheric Correction Working Group, although TES personnel will work alongside the ACWG collecting field data, especially spectral data of water and snow. Experimental procedure at these sites is documented in the Validation Plan for ASTER Standard Product AST-09. Japanese testing at the Kasumigaura Lake site will parallel US activities.

ACWG activities include radiometric measurements from boats, deployment of continuously recording buoys to measure temperatures directly, and radiosonde atmospheric profile measurements, reduced with the aid of the radiation model MODTRAN. The ACWG intends to monitor a 3x3 pixel area (270x270 m) to assess geologic variability. Because the water sites have low intrinsic variability, a 3x3 pixel area will probably suffice to estimate accuracy and precision.

The "rock" sites will also be established before launch. The chief activity at Mt. Humphreys and Mauna Loa will be to verify lithologic homogeneity over a 600x600 m site, sufficient for compiling performance statistics on a 30-pixel image area, and to document field emissivity spectra there. The mineralogic homogeneity, assessed in the field by conventional geologic methods, will be used to establish the minimum sampling density required for the field emissivity spectra. A similar experiment will be conducted at the sand dune sites, both in California and Japan. TIR imaging systems, available at JPL and commercially, will be used in the field (US) to help document site homogeneity at the m to 10-m scale.

Airborne TIR scanner (TIMS) overflights will be conducted of the "rock" sites before launch. These require that temperatures be measured over the sites. This will be done using a hand-held Everest radiometer at pre-selected locations for which field emissivity spectra have been measured. The Everest data will be calibrated against blackbody measurements using a manufactured horn encased in insulation and calibrated using a thermocouple. This device is available at JPL. Because it will take some time to measure temperatures for the whole site, drift will be accounted for by reference to a common base station. Spatial patterns of relative temperatures will be determined by low-altitude airborne imaging. These data will be used in conjunction with the field measurements. Atmospheric data will be acquired as described in the Validation Plan for ASTER Standard Product AST-09.

Pre-launch experimentation will identify any major algorithm flaws so that a corrected version can be prepared in time for delivery of the post-launch version to the DAAC.

3.2 Operational surface networks

No "Operational" surface networks have been identified which would directly support this validation effort with the exception of a network operated by CSIRO in Australia which could be used in addition to or in place of the "rock" sites.

3.3 Existing satellite data

Field experiments are generally planned around times when satellite data (e.g., Landsat, AVHRR) will be available. Existing data do not satisfy the multispectral requirements of TES testing and validation.

4. POST-LAUNCH ACTIVITIES

Post-launch activities will be similar to pre-launch validation exercises. Notably, emissivity spectra will have already been collected, and site heterogeneity already established, simplifying the task. Terra and low-altitude aircraft passes over validation sites will be synchronized and will be coordinated with field experiments to characterize temperatures and atmospheric conditions. We will also monitor TES results as frequently as possible over one or more previously characterized sites without further field measurements.

4.1 Planned field activities and schedules

The plan described here relies on measurements of surface temperatures and atmospheric conditions over at least a subset of the same validation sites explored during the pre-launch activities. With the addition of the ASTER data takes, actual pre- and post-launch activities will be similar. However, it will not be necessary to re-establish site emissivity characteristics during overflight.

It is proposed to drop the "rock" sites after initial post-launch activities have validated the TES algorithm on actual ASTER data; however, it is anticipated that the "water" sites at least will be reoccupied and monitored periodically during the life of the Terra platform.

Validation activities will commence immediately after launch. Every effort will be made to conduct at least two experiments over each validation site during the first 6-8 months of the Terra mission. Thereafter, at least one "water" site will be revisted frequently, perhaps quarterly, for the life of ASTER but without further field measurements.

4.2 New EOS-targeted coordinated field campaigns

The two US water sites are large enough to be used in MODIS as well as ASTER validation activities. Additionally, a land calibration site at Railroad Valley, Nevada, is large enough for MODIS. Railroad Valley is not a prime TES "rock" site because it is a playa, compositionally varying due to rain and wind. Nevertheless, the prime TES rock sites are too small for MODIS' use, and TES personnel will participate a May/June EOS joint validation/calibration field campaign in anticipation that such activity will help solidify support for similar joint activities in the post-launch time period.

4.3 Needs for other satellite data

Landsat-7 60-m TIR data will be useful in a general way in validation activities, especially if Landsat and ASTER data takes can be coordinated. MODIS data will be of use in that they may assist in the atmospheric correction of ASTER data. AVHRR and MODIS data will be useful in helping assess generalized haze and cirrus conditions at the validation sites.

4.4 Measurement needs

The following measurements are needed:

> *To characterize atmospheric conditions...* profiles of atmospheric moisture and temperature, estimates of atmospheric aerosol content and column ozone amount, physical and spectral radiometric measurements of surface temperatures at the time of EOS AM-1 overflight, and surface emissivity measurements near the time of overflight, with good location data for the surface measurements. In addition, low-altitude airborne TIR scanner data and spaceborne TIR will be helpful. MODIS and AVHRR images will help assess weather conditions (especially thin cirrus). All the above will be needed for the water sites and will be acquired for the atmospheric correction validation effort.
>
> *To characterize site conditions...* pre-launch emissivity maps (rock sites) and generalized spectra (water sites) will be combined with limited post-launch field measurements made with JPL's Micro-FTIR field emissivity spectrometer. Hand-held radiometric measurements will be made on a predetermined grid of sample locations at the rock sites to characterize temperatures. These will be merged with relative temperature measurements made by TIMS or an equivalent scanner from low-altitude aircraft (1400 m above terrain, or 4.5 m data).

4.5 Needs for instrument development

Field TIR imaging systems are required, especially during the pre-launch site-characterization phase, to assess emissivity and temperature heterogeneity scales from 1 cm to 10 m. These data bridge the gap between field spectra (10 cm) and low-altitude scanner data (10 m). JPL currently has constructed a suitable solid-state QWIP imaging system (256x256 pixels, 0.025 K sensitivity at 9.0 μm) that is usable in field settings, and we have experimented with it in the field. This instrument needs little adaptation to function well in the validation experiments, if regular access to it can be secured.

Pre-launch activities will benefit from having a sensitive aircraft scanner that duplicates ASTER's five TIR bands. TIMS is acceptable in general, although the match of spectral bands is not ideal. MASTER is designed for a good match, but has only recently become available.

4.6 Geometric registration site

Geometric registration is a basic Level-1 activity not related to the validation plan discussed here. Validation sites will be located on high-resolution aerial photographs first and then located on aircraft or ASTER images by cross-correlation using existing software at UW.

4.7 Intercomparisons (multi-instrument)

Intercomparison with surface temperature estimates from MODIS will be an important validation activity. Although the greatest insight will probably be cast on the efficacy of ASTER atmospheric reduction, this is one of the greatest sources of uncertainty in the TES standard Products.

5. IMPLEMENTATION OF VALIDATION RESULTS IN DATA PROCESSING

5.1 Approach

The validation results will be used to refine the TES algorithm to optimize the accuracy, precision, and cost of the standard products. The accuracy and precision will also be used as part of the QA documentation associated with the header of each ASTER surface-temperature and emissivity image. Finally, the results will be used to assess on a pixel-by-pixel basis the algorithm performance, and resulting precision estimates will be incorporated into a QA data plane associated with each standard product. It is anticipated that precision will vary chiefly with temperature and with the spectral contrast or MMD, and an important role of validation is to characterize the dependency quantitatively.

Validation is of sufficient importance that a peer-reviewed publication of pre-launch results is planned. Results will also be made available in text form at the DAAC responsible for processing ASTER data to Level 2 (currently, this would be at the EROS Data Center).

5.2 Role of EOSDIS

The primary role of EOSDIS in this validation plan is to supply the data products which are being validated for the time and location of the experiment. In doing this, EOSDIS will also acquire and process the necessary input data sets to process the ASTER data.

5.3 Plans for archiving of validation data

Validation data and a description of the processes, procedures and algorithms used will be archived in a report at the ASTER Team Leader's processing facility and also at the University of Washington SCF.

6. SUMMARY

The validation plan described above uses pre-launch experiments to characterize sites for post-launch validation, to fine-tune and document the TES algorithm, and to prepare initial QA assessments and assessment methodologies for the standard products. Field measurements of temperature, emissivities, and atmospheric conditions will be combined with aircraft and existing satellite TIR scanner data in this effort. Validation sites will be of two types: water and rock sites. Water sites will be used to determine temperature and emissivity recovery for graybodies. Rock sites will be used to test TES for regions of high emissivity contrast. Redundant sites will be maintained in the western US and Japan. One site (Railroad Valley) may be used specifically to allow for intercomparisons to MODIS.

Post-launch activity will be coordinated with Terra overflights and acquisition of ASTER and MODIS data. Collection of emissivity data in the field will be minimal, but temperature and atmospheric data will have to be acquired. Overlap in this activity with the Atmospheric Correction Working Group is anticipated.

Initial post-Launch validation will be concluded at each site within 6-8 months of launch, but continued experiments will be repeated annually for the life of the mission to check for changes in performance. The plan calls for such long-term experiments only at the water sites to maximize economy.

7. VALIDATION SITES TO BE USED FOR TES

In this section summaries of pertinent information about validation sites for TES are given. There are three types of sites: low-contrast sites over lakes or seas (§7.1), high-contrast sites over geologic surfaces (§7.2), and a site at which both types of

surfaces are to be studied (§7.3). The low-contrast sites are all proposed and supported by other working groups that will collect water surface temperatures and atmospheric data at the time of data overflights. The emissivity for water is already known; therefore, the TES validation effort at these sites consists of executing TES on the atmospherically corrected data and comparing the results to the measured or known values of T and ε for the water. At the high-contrast sites, TES is the only validation effort. At these sites TES will collect emissivities in advance of image acquisition, and surface temperatures and atmospheric data during data takes. The "combined" site is one at which ponds and a playa surface are both targets of interest to other groups. Here, the TES field effort will consist of measuring playa emissivities and temperatures.

7.1 Low-contrast "water" sites

Site name:	**Lake Tahoe.**
Site location:	39.2°N; 119.8°W
Lead investigators:	K. Thome, U. Arizona; F. Palluconi, JPL
Algorithm:	Level-1 processing calibration coefficients, Level-2 radiance, surface reflectance, atmospheric correction, TES.
Description:	High-altitude, large surface area, deep-water lake on the California-Nevada border.
Other support:	ASTER calibration test site which will also be used for MODIS calibration.
Test objectives:	To provide a thermally uniform target for in-flight radiometric calibration and cross-calibration of ASTER and MODIS. Evaluate TES performance for surfaces having low emissivity contrast.
Access:	Site is easily accessible all year by roads. Occasional snow closures in winter. Since the site is a water target, aircraft and boats are necessary for access. Shore locations are available.
Site size:	3x3 km.
Image area:	15x30 km.
Occupation:	For ASTER purposes, the site is only occupied for calibration/validation exercises. It should be possible to make arrangements for setting up equipment for more frequent measurements.
Elevation:	1900 m.
Surface cover:	100% water.
Climate:	Alpine, cold winters, frequent snow storms; cool dry summers with August thunderstorms.
Nearest weather station:	Truckee/Tahoe airport records winds, temperature and pressure - 10 km. Nearest radiosonde station: Reno, NV - 50 km
Available data:	Landsat 5 - EDC; AVHRR - EDC.
Field equipment:	µFTIR TIR spectrometer, Everest radiometers, Reagan sun photometers, radiosondes
Equipment available at site:	None.
Suitability for cal/val activities:	The site is a cal/val site
Pre-flight activities:	Aircraft overflights in conjunction with surface temperature measurements and atmospheric sounding. Data should be collected under clear-sky conditions.
Post-launch activities:	Same as pre-launch.
Data processing requirements:	For the calibration work, Level 1 ASTER data are required. For the atmospheric correction validation, the Level 2 surface radiance and surface reflectance products are required.
Key Words:	Lake Tahoe, calibration, ASTER, MODIS, atmospheric correction, TES.
Field measurements:	U of A will make airborne-based measurements of upwelling radiance from the lake, atmospheric transmittance using ground-based solar radiometers at the lake shore and at Truckee/Tahoe airport and sky radiance measurements from Truckee/Tahoe airport. JPL will collect water temperatures.

Site name:	**Kasumigaura Lake.**
Site location:	36°N; 140°E
Lead investigators:	T. Matsunaga, S. Rokugawa
Algorithm:	a) Atmospheric correction and water surface temperature estimation algorithms based on the regression of in-situ temperature data and ASTER TIR data. b) TBD (based on the regression of in-situ turbidity data and ASTER VNIR data after atmospheric correction). c) TES.
Description:	Kasumigaura Lake is a low-altitude eutrophic lake near Tsukuba, Japan**.**

Other support:	GSJ/ T. Matsunaga, RIKEN/ M. Kishino
Test objectives:	To establish ASTER a) water surface temperature algorithm b) turbidity algorithm and validate both special products (4A19 and 4A16, special). Validate TES temperatures for low-contrast (water) site.
Access:	Site is easily accessible all year .
Site size:	
Image area:	
Occupation:	Site is unoccupied.
Elevation:	
Surface cover:	NA
Climate:	
Nearest weather station:	Tsukuba.
Available data:	National Institute of Environmental Studies has obtained various water-quality and satellite data since 1980s.
Field equipment:	Thermometer: precision ±0.1K, accuracy ±0.5K(TBR). Various water-quality measurements.
Equipment available at site:	None.
Suitability for cal/val activities:	
Pre-flight activities:	Measure water surface temperatures and atmospheric parameters during aircraft overflights with multiband TIR sensors.
Post-launch activities:	With simultaneous sea-truth survey. Several times in first two years(TBR).
Data processing requirements:	Data quality, cloud fraction, and other QA information must be reported to sea-truth survey team with in 24 hours(TBR) after data acquisition.
Key Words:	Water surface temperature, turbidity, eutrophication, TES, ASTER
Field measurements:	Various water-quality measurements.

Site name:	**Salton Sea.**
Site location:	33.32°N; 115.72°W
Lead investigators:	F. Palluconi, JPL
Algorithm:	Land-Leaving TIR radiance, TES
Description:	The Salton Sea is a large (approx. 15X60 km) salt-water inland lake in the US.
Other support:	University of Arizona, K. Thome.
Test objectives:	This is a low-elevation site providing at times a warm, humid atmospheric column. The TES objective is to evaluate TES performance where atmospheric corrections are large.
Access:	Site is easily accessible by road and boat.
Site size:	4x4 km.
Image area:	60x60 km.
Occupation:	Site is unoccupied.
Elevation:	-50 m.
Surface cover:	Water.
Climate:	Warm and humid in late summer, never freezes.
Nearest weather station:	El Centro, CA?
Available data:	Unknown.
Field equipment:	Equipment brought to site: radiometers, radiosondes, buoys, sun photometers, GPS receivers.
Equipment available at site:	None.
Suitability for cal/val activities:	Yes. Could also be used by Landsat or MODIS.
Pre-flight activities:	characterize atmospheric conditions and water temperatures during aircraft overflights.
Post-launch activities:	characterize atmospheric conditions and water temperatures during aircraft overflights.
Data processing requirements:	Standard atmospheric correction plus estimating area average water temperature.
Key Words:	Atmospheric correction, water, thermal infrared, ASTER, TIMS, TES, temperature, emissivity.
Field measurements:	Bulk water temperature, surface skin temperature, atmospheric temperature and water vapor profiles, position measurements.

7.2 High-contrast "geology" sites

Site name:	**Mt. Humphreys.**
Site location:	37.25°N; 118.75°W
Lead investigators:	University of Washington (Gillespie); JPL (Kahle)
Algorithm:	Temperature/Emissivity Separation
Description:	Mt. Humphreys is a peak in the Sierra Nevada near Bishop, CA. The site is in the high basin to the west of the peak and just north of Paiute Pass. Paiute Pass is one of the lowest passes across the Sierra crest. The site is a homogeneous quartzose granitic pluton. Weathering products are minimum because the site was glaciated until 14,000 years ago. The site is smooth to minimize multiple scattering and covered only sparsely by vegetation.
Other support:	This site is not used by any other ASTER or EOS activities.
Test objectives:	The objective at this site is to evaluate TES performance for surfaces having high emissivity contrast. (Lake sites will be used to validate algorithm performance for near-graybodies). ASTER temperature and emissivity standard products will be compared to values measured in the field to determine accuracies and precisions.
Access:	Site is easily accessible by a 10-km trail in summer.
Site size:	Site size is 0.5x0.5 km or greater (25 ASTER TIR 90-m pixels).
Image area:	Area to be imaged is 10 km x 10 km, in part to allow comparison to and simulation of MODIS data.
Occupation:	Site is unoccupied.
Elevation:	3350 m.
Surface cover:	<5% white pine.
Climate:	Alpine, 150 cm/year winter precipitation, snow-bound November-May.
Nearest weather station:	Bishop Airport, 15 km.
Available data:	TIMS, NS-001 and Landsat TM images and air photos.
Field equipment:	µFTIR TIR spectrometer, Everest radiometers, Reagan sun photometers if possible, radiosondes, Amber Radiance-1 TIR imaging systems with 9-µm QWIP detectors.
Equipment available at site:	None.
Suitability for cal/val activities:	The site is not suitable for cal/val activities because of access and seasonality.
Pre-flight activities:	characterize emissivities and surface temperature variability at decadal scales from 1 cm to 1 km; aircraft overflights in conjunction with surface temperature measurements and atmospheric sounding.
Post-launch activities:	Surface measurement of emissivities (limited) and temperatures, atmospheric characteristics, coordinated with aircraft underflights and ASTER data acquisition.
Data processing requirements:	Aircraft images are processed to simulate ASTER and MODIS TIR data. (MODIS: possibly at ASTER 90-m spatial resolution). All ASTER images are processed through TES. Atmospheric data are reduced to atmospheric transmissivity, path radiance and sky irradiance and input to TES. Surface emissivity and temperature fields are reduced to ASTER-scale averages for comparison to image data over a 5x5 or 6x6 pixel area. MODIS data may be processed through a TES-like algorithm adapted for its different bands. Aircraft data will be registered to actual ASTER images for comparison of standard products.
Key Words:	TES, temperature, emissivity, ASTER
Field measurements:	Field measurements to be made by Gillespie: surface emissivities and temperatures at scales from 1 cm to 1 km, atmospheric characteristics sufficient to estimate transmissivity, path radiance and sky irradiance at the time of overflight, surface roughness and vegetation cover, mineralogy.

Site name:	**Mauna Loa.**
Site location:	19.5°N; 155.6°W
Lead investigators:	University of Washington (Gillespie); JPL (Kahle)
Algorithm:	Temperature/Emissivity Separation
Description:	Mauna Loa is a volcano on the island of Hawai'i. The site is in the summit caldera, in a National Park. The target is a flat, smooth, homogeneous surface of pahoehoe. There is no vegetation. Weathering products are minimum because the lava was erupted in 1984.

Other support:	This site is not used by any other ASTER or EOS activities. Spectrally contrasting lavas with silica weathering rinds are found nearby on the caldera rim.
Test objectives:	The objective at this site is to evaluate TES performance for surfaces having high emissivity contrast. ASTER temperature and emissivity standard products will be compared to values measured in the field to determine accuracies and precisions.
Access:	Site is easily accessible by a 10-km trail.
Site size:	Site size is 1x1 km or greater (120 ASTER TIR 90-m pixels).
Image area:	Area to be imaged is 10 km x 10 km, in part to allow comparison to and simulation of MODIS data.
Occupation:	Site is unoccupied.
Elevation:	4170 m.
Surface cover:	Unvegetated basalt.
Climate:	Tropical alpine, occasionally snow-bound.
Nearest weather station:	At 3400 m on the north flank of the volcano, 10 km; Hilo and Kona airports (30 km).
Available data:	TIMS, NS-001 and Landsat TM images and air photos.
Field equipment:	µFTIR TIR spectrometer, Everest radiometers, Reagan sun photometers if possible, radiosondes, Amber Radiance-1 TIR imaging systems with 9-µm QWIP detectors.
Equipment available at site:	None.
Suitability for cal/val activities:	The site is not suitable for cal/val activities because of access.
Pre-flight activities:	Characterize emissivities and surface temperature variability at decadal scales from 1 cm to 1 km; aircraft overflights in conjunction with surface temperature measurements and atmospheric sounding.
Post-launch activities:	Surface measurement of emissivities (limited) and temperatures, atmospheric characteristics, coordinated with aircraft underflights and ASTER data acquisition.
Data processing requirements:	Aircraft images are processed to simulate ASTER and MODIS TIR data. (MODIS: possibly at ASTER 90-m spatial resolution). All ASTER images are processed through TES. Atmospheric data are reduced to atmospheric transmissivity, path radiance and sky irradiance and input to TES. Surface emissivity and temperature fields are reduced to ASTER-scale averages for comparison to image data over a 5x5 or 6x6 pixel area.
Key Words:	TES, temperature, emissivity, ASTER
Field measurements:	Field measurements to be made by Gillespie: surface emissivities and temperatures at scales from 1 cm to 1 km, atmospheric characteristics sufficient to estimate transmissivity, path radiance and sky irradiance at the time of overflight, surface roughness and vegetation cover, mineralogy.

Site name:	**Kelso Dunes.**
Site location:	34.88°N; 115.71°W
Lead investigators:	University of Washington (Gillespie); JPL (Kahle)
Algorithm:	Temperature/Emissivity Separation
Description:	Kelso Dunes is just north of Granite Pass in the Mojave Desert of California. It is accessible from JPL with a 3-hr drive. The site is a field of active sand dunes composed largely of quartz sand. It is covered only sparsely by vegetation. Some spectral variability arises because of magnetite segregations of dune slopes and aeolian silt in interdune flats.
Other support:	This site is not used by any other ASTER or EOS activities.
Test objectives:	The objective at this site is to evaluate TES performance for surfaces having high emissivity contrast. (Lake sites will be used to validate algorithm performance for near-graybodies). ASTER temperature and emissivity standard products will be compared to values measured in the field to determine accuracies and precisions.
Access:	Site is easily accessible by road.
Site size:	Site size is 0.5x0.5 km or greater (25 ASTER TIR 90-m pixels).
Image area:	Area to be imaged is 10 km x 10 km, in part to allow comparison to and simulation of MODIS data.
Occupation:	Site is unoccupied.
Elevation:	600 m.
Surface cover:	<5% desert scrub.
Climate:	Desert, 20 cm/year winter storms and summer thunderstorms, infrequent snowfall.

Nearest weather station:	Barstow, 50 km.
Available data:	TIMS, NS-001 and Landsat TM images and air photos.
Field equipment:	µFTIR TIR spectrometer, Everest radiometers, Reagan sun photometers if possible, radiosondes, Amber Radiance-1 TIR imaging systems with 9-µm QWIP detectors.
Equipment available at site:	None.
Suitability for cal/val activities:	The site is not suitable for cal/val activities because of topographic relief of the sand dunes.
Pre-flight activities:	Characterize emissivities and surface temperature variability at decadal scales from 1 cm to 1 km; aircraft overflights in conjunction with surface temperature measurements and atmospheric sounding.
Post-launch activities:	Surface measurement of emissivities (limited) and temperatures, atmospheric characteristics, coordinated with aircraft underflights and ASTER data acquisition.
Data processing requirements:	Aircraft images are processed to simulate ASTER and MODIS TIR data. (MODIS: possibly at ASTER 90-m spatial resolution). All ASTER images are processed through TES. Atmospheric data are reduced to atmospheric transmissivity, path radiance and sky irradiance and input to TES. Surface emissivity and temperature fields are reduced to ASTER-scale averages for comparison to image data over a 5x5 or 6x6 pixel area. MODIS data may be processed through a TES-like algorithm adapted for its different bands. Aircraft data will be registered to actual ASTER images for comparison of standard products.
Key Words:	TES, temperature, emissivity, ASTER
Field measurements:	Field measurements to be made by Gillespie: surface emissivities and temperatures at scales from 1 cm to 1 km, atmospheric characteristics sufficient to estimate transmissivity, path radiance and sky irradiance at the time of overflight, surface roughness and vegetation cover, mineralogy.

Site name:	**Tottori Sakyu (Tottori Dunes).**
Site location:	35.53°N; 134.22°E
Lead investigators:	T. Matsunaga, T. Takashima
Algorithm:	Temperature/Emissivity Separation, Atmospheric correction
Description:	Tottori Sakyu is a linksland in Tottori Prefecture, west Japan, and faces the Japan Sea. The dunes are composed mainly of quartz sand from weathered granites. There are two small lakes nearby.
Other support:	This site is used for validating two ASTER Standard Products (TES and Land-leaving radiance) and a special product (water temperature). It is not used by other EOS activities.
Test objectives:	Evaluate TES performance for surfaces having high emissivity contrast (dunes) and low contrast (ponds). ASTER temperature and emissivity standard products will be compared to values measured in the field to determine accuracies and precisions. The site will also be used to validate atmospheric corrections.
Access:	Site is easily accessible by road and bus service from an airport and JR (Japan Railway) station, 6 km away.
Site size:	Site size is 3.5x1.0 km (dunes) and 4x2 km and 0.75x0.75 km (lakes).
Image area:	Area to be imaged is 10 km x 10 km.
Occupation:	Site is unoccupied (National Park).
Elevation:	<90 m.
Surface cover:	sparse vegetation.
Climate:	Average temperature and humidity: Jan - 5.2°C, 77%; Apr - 11.9°C, 66%; Jul - 23.9°C, 82%; Oct - 156.2°C, 75%. Cloudy in winter.
Nearest weather station:	Radiosonde: Yonaga City (75 km west). Hourly meteorological data at surface: Tottori City (4 km south).
Available data:	ERSDAC owns several Landsat TM scenes and probably has JERS-1 OPS images. GSJ has sand samples and laboratory emissivity spectra for different moisture contents.
Field equipment:	ERSDAC TIR spectrometer, Thermometry (±1 K accuracy, ±0.1 K precision) by GSJ and other institutions.
Equipment available at site:	None.
Suitability for cal/val activities:	The site may be suitable for cal/val activities.

Pre-flight activities:	Sand emissivities have already been measured. Surface temperatures , meteorological data and atmospheric sounding need to be taken simultaneously with nadir-looking aircraft images.
Post-launch activities:	Same.
Data processing requirements:	Atmospheric correction with local radiosonde data.
Key Words:	TES, surface temperature, emissivity, sand, wet atmosphere, ASTER
Field measurements:	In-situ surface temperature measurement(sand and water surface). In-situ surface emissivity measurement in the TIR region(sand surface). Lab sample emissivity/reflectance measurement in the TIR region.

7.3 Combined sites

Site name:	**Railroad Valley.**
Site location:	38.5°N; 115.7°W
Lead investigators:	P. Slater, K. Thome, U. A.; F. Palluconi, JPL.
Algorithm:	Level-1 radiometric calibration, Level-2 surface radiance and surface reflectance, Atmosphere correction, TES
Description:	Clay, dry-lake, playa surface in central Nevada. Includes Lunar Lake, another playa nearby.
Other support:	ASTER validation site.
Test objectives:	Objective is to provide a bright, uniform target for radiometric calibration and validating the retrieval of surface reflectance. Ponds will be used for TIR atmosphere correction. Evaluate TES performance: ASTER temperature and emissivity standard products will be compared to values measured in the field to determine accuracies and precisions.
Access:	Easy to moderate. Paved roads lead to the area with access to target site via unpaved roads which can be soft when wet. For some areas of the playa, 4-wheel drive is recommended.
Site size:	1x1 km.
Image area:	10x15 (Railroad Playa); 3x3 km (Lunar Lake).
Occupation:	Site is unoccupied.
Elevation:	1400 m (Railroad Playa); 1800m (Lunar Lake).
Surface cover:	Clay soils, no vegetation on target site, very little vegetation over extended site.
Climate:	Winter temperatures often reach below -5 degrees C, summer temperatures regularly exceed 30 degrees C. The wet seasons are the summer and winter with rain in the summer. Spring and fall are often cloudy.
Nearest weather station:	Weather station: Ely - 100 km; Radiosonde station: Mercury, Nevada - 200 km
Available data:	Landsat 5 - EDC; SPOT 3 - SPOT Corp.; AVIRIS - JPL.
Field equipment:	µFTIR TIR spectrometer, Everest radiometers, Reagan sun photometers if possible, radiosondes,.
Equipment available at site:	None.
Suitability for cal/val activities:	The site is a cal/val site.
Pre-flight activities:	characterize emissivities and surface temperature variability at decadal scales from 1 cm to 1 km; aircraft overflights in conjunction with surface temperature measurements and atmospheric sounding. Clear-sky conditions required.
Post-launch activities:	Surface measurement of emissivities (limited) and temperatures, atmospheric characteristics, coordinated with aircraft underflights and ASTER data acquisition.
Data processing requirements:	Level-2 surface radiance and surface reflectance ASTER data are required. Aircraft images are processed to simulate ASTER TIR data, then atmospherically corrected and processed through TES.
Key Words:	Calibration, ASTER, cross-calibration, TES, temperature, emissivity.
Field measurements:	The U of A will make ground- and airborne-based measurements of surface reflectance and radiance. Airborne measurements will be from >10,000' ASL. Will measure atmospheric transmittance using ground-based solar radiometers as well as sky radiance. Field emissivity measurements will be made by JPL and UW. Surface temperatures and atmospheric characteristics will be made during overflights.

* * * * * * * * *